MICROFLUIDIC PLATFORMS FOR CELL CULTURE AND MICROENVIRONMENT CONTROL

By

Yandong Gao

Dissertation

Submitted to the Faculty of the

Graduate School of Vanderbilt University

in partial fulfillment of the requirements

for the degree of

DOCTOR OF PHILOSOPHY

in

Mechanical Engineering

December, 2011

Nashville, Tennessee

Approved:

Associate Professor Deyu Li

Assistant Professor Joh F. Edd

Assistant Professor Haoxiang Luo

Professor Taylor G. Wang

Assistant Professor Donna J. Webb

To my beloved parents and wife

ABSTRACT

Microfluidic systems have the ability to tailor cell microenvironment in a controllable and reproducible fashion that cannot be easily achieved by conventional methods. This research aimed to develop microfluidic platforms for manipulation of cellular microenvironment and communication, which enabled new assays for biological studies to advance our understanding of various biological systems. These simple and compact platforms were compatible with conventional cell culture practice, which would lead to potential widespread acceptance by the biological community.

To control the interactions between two cell populations, a mechanical valve was integrated into the microfluidic platform containing two cell culture chambers. In the natural state, the two microfluidic chambers were connected, and the two cell populations cultured side by side communicated with each other. Once the valve was activated, the two cell populations were isolated and distinct cell types could be treated individually without affecting the other. To differentiate cell-cell interactions through either direct cell contacts or soluble factors alone, an agarose-coupled valve barrier was constructed. This barrier blocked cell migration but permitted exchange of signaling molecules. We further modified the permeable barrier by embedding ligand traps, which had the ability to bind selectively to certain soluble molecules with high affinity. As a result, the barrier became semi-permeable and could block the transport of a specific type of molecule, which provided a new way to probe the cellular signaling pathway.

To study chemotaxis, a pressure balance fluidic circuit was designed and fabricated which had the ability to generate automatically two streams with equivalent pressure and flow rate from two individual passive pumps. By feeding a pyramidal microfluidic circuit with these two streams, an approximately linear concentration gradient was created and maintained. The pressure balance fluidic circuit was also integrated into the traditional Dunn chamber to generate a concentration gradient on a two-dimensional surface or in a three-dimensional matrix.

We believe that these platforms would have extensive applications for neurobiology and cancer biology, as demonstrated by the studies of dynamic imaging of synapse formation, neuron-glia co-culture, tumor cell – endothelial cell cross-migration, and fibrosarcoma cell migration.

ACKNOWLEDGEMENTS

I would like to express my deep gratitude and hearty thanks to my supervisor Prof. Deyu Li for his invaluable guidance and constant encouragement and patience. He has spent his valuable time with me and made me feel the real zest of research work. I am highly indebted to him for his untiring devotion and willingness.

I also would like to express my sincere thanks to Prof. Donna Webb for providing me with the opportunity of performing the fascinating biological research. I was naïve on biology when I first arrived at Vanderbilt. Her constructive comments and guidance have helped me to understand biology and become a disciplinary researcher.

I would like to thank my former advisor Prof. Dongqing Li for the invaluable guidance and support. I also would like to thank Dr. Devi Majumdar for her insight and patience, without whom I would not be able to accomplish nearly as much.

I am grateful to my committee members Profs. Taylor G. Wang, Haoxiang Luo and Jon F. Edd for their time and critical assessment. Also I would like to thank Profs. Charles Lin, Andries Zijlstra and Jin Chen for giving me the freedom to explore my ideas.

I have benefited greatly from my association with all past and present members of the Li lab, Webb lab, Lin lab, Chen lab, Moses lab and Zijlstra lab, in particular Yuejun Kang, Zhemin Wu, Jiashu Sun, Guoqing Hu, Yao-Nan Wang, Chanhee Chon, Rebecca Michaud, Wan-Hsin Lin, Lan Hu, Dana Brantley-Sieders, Bojana Jovanovic, Candice Shaifer, and Aubie Shaw.

Finally, I thank all those who extended their helping hands towards me in various ways during my study at Vanderbilt.

TABLE OF CONTENTS

ABSTRACT i
ACKNOWLEDGEMENTS iii
LIST OF FIGURES viii

Chapter
1. INTRODUCTION 1
1.1 Background 1
1.2 Cell Microenvironment and Cell-Cell Interactions 3
1.3 Microfluidic Platforms for Cell Culture 5
1.4 Dissertation Overview 9

2. VALVE-ENABLED MICROFLUIDIC PLATFORMS FOR NEURONAL STUDIES 12
2.1 Motivation 12
2.1.1 Synapse formation 12
2.1.2 Glia and their roles in the nervous system 15
2.2 Microfluidic Platform Design and Fabrication 16
2.3 Device Characterization 21
2.3.1 Valve performance 21
2.3.2 Flow field 28
2.3.3 Passive pump 29
2.4 Neuronal Study Results 33
2.4.1 Synapse formation 33
2.4.2 Side-by-side neuron-glia co-culture 37
2.4.3 Quad-chamber side-by-side neuron-glia co-culture 41
2.4.4 Vertically-layered neuron-glia co-culture 44
2.5 Summary 50

3. MICROFLUIDIC PLATFORMS FOR TUMOR BIOLOGY STUDIES 51
3.1 Introduction 51
3.2 Microfluidic Platforms with Etched Glass Slides as Substrates 52

3.3 Tumor angiogenesis under normoxic and hypoxic conditions 56
3.4 Cross-migration of 4T1 tumor cells and ECs 60
3.5 Summary 64

4. MICROFLUIDIC CULTURE PLATFORMS WITH PERMEABLE AND SEMI-PERMEABLE BARRIERS 65
4.1 Introduction 65
4.2 Microfluidic Platforms with An Agarose Coupled Valve Barrier 66
4.2.1 Design principle 66
4.2.2 Surface treatment and barrier formation 68
4.2.3 3D cell co-culture and discussions 70
4.3 Microfluidic Platforms with a Semi-permeable Barrier 72
4.3.1 Design principle 72
4.3.2 Demonstration of ligand traps by two fluorescent proteins 74
4.3.3 An analytical model of the barrier's performance 78
4.4 Summary 84

5. MICROFLUIDIC CULTURE PLATFORMS WITH CONCENTRATION GRADIENTS 86
5.1 Introduction 86
5.2 Design Principle of the Pressure Balance Circuit 89
5.3 Pyramidal Microfluidic Device using A Pressure Balance Circuit to Generate Concentration Gradient in 2D 93
5.3.1 Device fabrication 93
5.3.2 Numerical modeling of the performance 94
5.3.3 Experimental validation of the generated concentration gradient 98
5.4 A Variation of the Dunn Chamber for 2D and 3D Cell Migration Studies 104
5.4.1 Concentration gradient in 2D 104
5.4.2 Concentration gradient in 3D 106
5.4.3 Cell Migration in 3D Collagen Matrices 108
5.5 Summary 115

6. SUMMARY AND OUTLOOK 117

6.1 Summary 117
6.2 Outlook, Challenge and Future work 119

APPENDIX 122
A. Two-layer Photolithography Protocol 122
B. Five Hundred Micrometre High Photolithography Protocol 124
C. Transfection of Neurons 125
D. MATLAB code for concentration in the semi-permeable barrier 127

REFERENCES 128

LIST OF FIGURES

Figure 2.1: The design and operation mechanism of the co-culture platform for cell-cell interaction studies 17

Figure 2.2: Schematics of the fabrication process 20

Figure 2.3: Computational model of the mechanical valve 22

Figure 2.4: Computational results of the deformed configurations at different actuation pressures for the PDMS's agent-to-base ratio of 1:12 ($G=5.5\times10^5$ Pa) 24

Figure 2.5: Computational results of the deformed configurations at different actuation pressures for the PDMS's agent-to-base ratio of 1:15 ($G=3.6\times10^5$ Pa) 25

Figure 2.6: Computational results of the deformed configurations of sloped side walls 26

Figure 2.7: Fluorescent images after one chamber was filled with FITC 26

Figure 2.8: Simulation results of the velocity profiles in the cell culture chambers without **(a)** and with **(b)** asymmetric semi-lunar shaped supporters 29

Figure 2.9: Schematics of the menisci to estimate the flow rate 31

Figure 2.10: Schematics of cell loading and separate transfection 34

Figure 2.11: Images of neuronal processes in microfluidic chambers 36

Figure 2.12: Co-culture of neurons and glia in the microfluidic platform 39

Figure 2.13: Transfection efficiencies for neurons cultured in traditional culture dishes and in microfluidic platforms containing neuron-neuron and neuron-glia cultures 40

Figure 2.14: Schematic of the quad-chamber side-by-side neurons-glia co-culture 42

Figure 2.15: Fluorescent images of cells in the quad-chamber co-culture system 43

Figure 2.16: Schematic of the vertically-layered neurons-glia co-culture 45

Figure 2.17: Intense crosstalks between the two cell populations 46

Figure 2.18: Phase contrast images of vertically-layered neurons-glia co-culture 47

Figure 2.19: Quantification of number of spine formations and synaptic contacts in neurons cultured in three different microfluidic platforms 48

Figure 3.1: Schematics of microfluidic platforms for cancer biology studies 54

Figure 3.2: AFM images of a plain and PLL coated glass coverslip 55

Figure 3.3: Schematics of the microfluidic platforms for tumor angiogenesis studies 57

Figure 3.4: The interactions of tumor cells and ECs 59

Figure 3.5: Hypothesis of endothelial EphA2 regulates Slit2 to modulate tumor angiogenesis 61

Figure 3.6: Phase contrast images of 4T1 and ECs cross-migration 62

Figure 3.7: Cross migration of 4T1 and ECs 63

Figure 3.8: Migration results assessed by 4 independent 20× field view per device 63

Figure 4.1: Schamtics of the formation of an ACVB in the microfluidic platform 67

Figure 4.2: The cell co-culture platform with an ACVB 69

Figure 4.3: Schematics of the semi-permeable barrier, which is used to block the transport of certain ligand from one chamber to the other 73

Figure 4.4: Schematics of the process to fabricate the mold for the first PDMS layer 75

Figure 4.5: Demonstration of the semi-permeable barrier with two fluorescent proteins 76

Figure 4.6: Schematic of transport of ligand (A) through a barrier, where it binds to its immobile receptor (B) and forms the ligand-receptor complex (S) 78

Figure 4.7: Ligand's concentration in the barrier as Da = 100 81

Figure 4.8: Relationship between the Damköhler number and the Péclet number 83

Figure 5.1: Design of the microfluidic concentration gradient generator 90

Figure 5.2: Simulation results of concentration distribution at the top of the microfluidic network 96

Figure 5.3: Simulation results of the concentration difference between the two streams in the compensation channels 97

Figure 5.4: Experimental validation of the concentration gradient generator 100

Figure 5.5: Fluorescent intensity profiles in the cell culture and observation zone 101

Figure 5.6: Comparison of fluorescent intensity profiles of micro-fluidic devices with and without the pressure balance zone 102

Figure 5.7: Concentration profiles for 12 h 103

Figure 5.8: Concentration gradients versus time 103

Figure 5.9: Microfluidic 2D gradient generator using
the source/sink construct 105

Figure 5.10: Microfluidic 3D gradient generator and
the mechanism of its integrated valve 107

Figure 5.11: Schematic and operation of the integrated valve 107

Figure 5.12: Mechanisms of Rho-protein regulation..... 108

Figure 5.13: Schematics of the PDMS layers of the 3D
gradient generator 110

Figure 5.14: Z-stack images of HT1080 cells in collagen
matrix acquired by reflection microscopy 112

Figure 5.15: Time lapse images of HT1080 cell migration
in a collage matrix 113

Figure 5.16: Migration velocity of GFP (control) and GFP-Asef2
cells on a 2D surface and in a 3D matrix..... 114

CHAPTER 1

INTRODUCTION

1.1 Background

Microfluidics, the study of fluid flow at microscale and its applications in biological, biomedical, and chemical analyses, has seen tremendous progress over the last two decades (Squires and Quake, 2005). Under the framework of 'lab-on-a-chip', 'micro-total-analysis system (μTAS)' or 'bio-micro-electro-mechanical system (bio-MEMS)', various microfluidic systems have been developed for biological investigations (Dittrich and Manz, 2006; El-Ali, et al., 2006; Narayanan, et al., 2006). Microfluidic systems have many advantages over traditional techniques, such as low cost, low reagent consumption, fast response time, and high-throughput analysis, which have been utilized for biological studies at both molecular (DNA/proteins) and cellular levels. Some microfluidic systems typically miniaturize and shrink the corresponding traditional bulk analysis systems to microscale in order to take some of the above-mentioned advantages; and others create new functions based on the unique physical and chemical characteristics at microscale which are not available for macro-systems. One important class of microfluidic systems are those for cell culture and microenvironment control to interrogate cellular behaviors in specified physiological microenvironments, which are not readily achievable in conventional bulk systems (Thorsen, et al., 2002).

Cell culture *in vitro* is one cornerstone of modern biology, which provides a useful model for understanding fundamental cell biology as well as an approach to mass production of proteins and vaccines (Freshney, 2005). After isolated from donor tissue, cells are supplied with proper media and gas mixture and maintained at an appropriate temperature for their growth and reproduction, which provides a route for understanding cellular behavior in a controlled *in vitro* environment. Since the experiments are performed in a controlled manner, *in vitro* studies usually have the ability to decouple multiple variables to dissect the mechanisms of complex biological interactions. In addition, *in vitro* experiments can help to reduce the costs and labors compared to tissue culture and animal experiments.

Cells that are cultured directly from tissue disaggregation or explants are known as primary cells (Freshney, 2005). Most primary cells in cultures have a limited lifespan, undergo the process of senescence, and lose their ability of replication after a certain number of divisions. Some cells such as neurons even do not divide at all. In contrast, an established cell line extends the cell's lifespan. The cells have theoretically acquired the ability to proliferate indefinitely. In the *in vitro* environment, some cells can grow in suspension, but most cells need to be attached to a solid substrate to survive. Recently three-dimensional (3D) cell culture in which cells are embedded in a bio-gel matrix became popular because cells cultured in a 3D environment better represent their *in vivo* cellular behaviors (Abbott, 2003; Bissell and Radisky, 2001; Cukierman, et al., 2001).

1.2 Cell Microenvironment and Cell-Cell Interactions

In vivo, cells spend all their lives in a complex and dynamic microenvironment characterized by its physical properties, biochemical components, neighboring cells, and specific extracellular matrix (ECM) components (Alberts, 2002). The cell microenvironment varies remarkably in different tissues. Within their microenvironment, cells perform their functions properly through interactions and communication with other cells and the ECM. Recently, understanding cells' response to the ECM and the presence of other cells has attracted significant attentions (Abbott, 2003; Cukierman, et al., 2001; Even-Ram and Yamada, 2005; Sabeh, et al., 2004). One advantage of the *in vitro* cell culture model is to allow researchers to identify the functions of specific factors through designed experiments. However, this task is extremely challenging because of the complexity of cellular interactions in the *in vivo* milieu.

Cell-cell communication and interactions are essential for cell survival, growth, and differentiation during embryogenesis and organogenesis (Skinner, 1991). Surface receptors, soluble extracellular molecules and the ECM all play important roles in cell-cell communication and interactions. Even if a single cell type is maintained, cells must reach a certain density to remain healthy. In addition, the culture media often contain complex cell-derived ingredients including various nutrients and growth factors. Therefore, cells are still in communication with each other and interacting with other cell types indirectly.

In multi-cellular organisms, cells have specialized structures called cell junctions to join with each other or to the ECM to form tissues and organs. Cell junctions usually involve transmembrane receptors that interact with the cytoskeleton on the in-

side of the plasma membrane and bind to other cells or the ECM on the extracellular side (Alberts, 2002). These junctions not only mechanically link cells together but also are essential for cell survival. This is why cells usually need to attach to a proper surface and form a monolayer to survive in a two-dimensional (2D) culture. Some junctions also mediate the passage of signals from one cell to its neighboring cells. Synapse, for example, is a highly specialized intercellular junction that mediates transmission of information between neurons. Another example is that many cell surface-bound proteins bind to receptor tyrosine kinases. Both can simultaneously act as ligands and receptors to guide the cell migrations and axon extensions (Butler, et al., 2010; Cheng, et al., 2002).

Soluble signaling molecules include hormones, cytokines and growth factors secreted by local (paracrine signals) or distant (endocrine signals) cells. These molecules are transported away from the source via diffusion or convection and function as ligands. Target cells sense most of such extracellular signals via their surface receptor proteins and then activate complex intracellular biochemical cascades to regulate the cell physiological behaviors. Not only the concentration but also the spatial and temporal distribution of these soluble factors is important in regulating cell behaviors. Chemotaxis, for example, is a phenomenon in which cells migrate in response to the gradient of a certain molecule, which plays a critical role in tumor metastases (Lauffenburger and Horwitz, 1996; Webb and Horwitz, 2003).

Cells typically reside in an environment with a very specific 3D ECM, which is produced by cells and consists of collagens, proteoglycans, adhesive glycoproteins and associated bound protein (Even-Ram and Yamada, 2005). Cells bond to the ECM

through their cell-ECM junctions. Along with providing a framework within which cells form tissues, the ECM directly modulates cell attachment, shape, morphology, migration, orientation and proliferation. On the other hand, cells can also organize and alter the extracellular matrix dynamically. During protease-dependent migration, for example, cells secret matrix metalloproteinase to cleave ECM fibrils to create a way to proceed (Friedl, et al., 1998).

1.3 Microfluidic Platforms for Cell Culture

Because of the importance of cell culture and microenvironment control in *in vitro* cell biology studies, various microfluidic platforms have been developed in the past two decades (Gross, et al., 2007; Meyvantsson and Beebe, 2008; Yeon and Park, 2007). This development benefits from the rapid progress of microfabrication techniques. Traditionally, microfabrication has been heavily based on silicon and glass as the construction materials, which requires access to expensive state-of-the-art cleanroom facilities and usually involves high costs. In addition, silicon is not transparent, which limits its applications to studies requiring high-resolution imaging capabilities. Therefore, the device development has been severely limited to highly specialized studies. The development of microfluidic systems has gained a great deal of momentum since the soft-lithography technique, based on transparent elastomeric materials ─ typically poly(dimethylsiloxane) (PDMS), became available (McDonald and Whitesides, 2002; Xia and Whitesides, 1998). The soft-lithography technique is of low-costs with the capability of rapid prototyping. In addition, PDMS is non-toxic, biocompatible, thermally and chemically stable, gas permeable, and optically transparent for high-

resolution imaging (McDonald and Whitesides, 2002; Xia and Whitesides, 1998). All of these desirable features make PDMS popular in microfluidic devices targeting at novel biological assays.

Microfluidic platforms have intrinsic advantages for *in vitro* cell culture over conventional biological platforms, which have attracted extensive attention recently (Dittrich and Manz, 2006; El-Ali, et al., 2006; Gross, et al., 2007; Meyvantsson and Beebe, 2008). The characteristics of microfluidic systems include the small length scale, the laminar flow, and the large surface-area-to-volume (SAV) ratio, which grant these systems unique advantages (Paguirigan and Beebe, 2008; Squires and Quake, 2005; Walker, et al., 2004). For example, local pH and nutrient concentration variations have been a severe concern in conventional cell culture, which can be readily addressed in well-designed microfluidic platforms because fresh media flow can evenly distribute nutrients and remove wastes to improve cell viability. Because of the simple laminar flow characteristics in microfluidic platforms, mathematical descriptions of the flow patterns are available and accurate mathematical models can be constructed to design and revise the platform to promote specific cell behaviors. More importantly, various aspects of the cellular microenvironment could be engineered in a precisely controlled manner, which will create a cell microenvironment in a controllable and reproducible fashion to test biological models.

Various novel microstructures open new opportunities for spatial control at a single cell level for cell-cell interactions studies. Taking advantage of this precise spatial control capability, several different microfluidic platforms have been developed for cell co-culture and interaction studies. Micropatterning technique (Bhatia, et al.,

1997; Folch and Toner, 1998; Kane, et al., 2006; Khetani and Bhatia, 2008) modifies the surface chemical properties of the substrate by patterning/coating desired molecules at selected locations. Employing the affinity of cells to the coated molecules, one type of cells can be loaded to the coated region. Other cells can then be loaded to the rest of the substrate and co-cultured with the previously loaded cells. With the benefit of microfabrication, the well-defined adhesive region could be as small as a single cell body (Scholl, et al., 2000; Vogt, et al., 2005). This technique allows for co-culture of different cell populations and examination of cellular activities, which provides the possibility for many interesting biological studies. However, the cells in co-culture are exposed to the same media; therefore, it is impossible for separate treatment to each cell type without affecting the entire culture. In addition, this technique is only suitable for 2D cell co-culture as a result of the inherent limitation of surface-patterning.

In addition to surface patterning, cells can also be trapped in specific locations and cell-cell interactions can be controlled (Hui and Bhatia, 2007; Khademhosseini, et al., 2005; Skelley, et al., 2009). For example, Skelley *et al*. (2009) presented a microfluidic device in which dense PDMS cell trap arrays were fabricated inside a flow channel to capture two types of cells together and study their pairing and fusion. Hui *et al*. (2007) reported a reconfigurable co-culture platform in which two comb-fingers like parts were used to control the separation distance between two cell populations. This development is important in the sense that the platform allows two cell populations to interact with each other in a controlled manner. However, the comb-fingers were made of silicon leading to imaging and cost issues.

In microfluidic systems, because of the small length scale, viscosity effects are more important than inertia effects; therefore, laminar flow dominates in microfluidic systems and turbulent effects become negligible. As a result, the combination of several streams will flow in parallel to each other with only slow diffusion-based mixing. This characteristic of laminar flow has been used for directly patterning the adhesive molecules on a substrate surface and for cell deposition (Berthier, et al., 2011; Takayama, et al., 1999). In laminar flow, soluble factors and suspended particles are transported by diffusion rather than convection in the direction perpendicular to the flow. Therefore, if several streams containing different concentrations of certain substances flow side by side, a stable concentration gradient with complex profiles can be generated in the cross-flow direction (Dertinger, et al., 2001; Jeon, et al., 2000; Jeon, et al., 2002; Lin, et al., 2004; Takayama, et al., 2001; Walker, et al., 2005).

Another important feature of microfluidic systems is the large SAV ratio, which is often several orders of magnitude higher than that of bulk systems. Because relatively more surface areas are available for transfer and less amount of mass and heat to be transferred, the large SAV ratio is efficient for mass and heat transport (Atencia and Beebe, 2005). However, a large SAV ratio can be problematic for microscale cell cultures (Walker, et al., 2004). If the surface of the microchannels could absorb/adsorb molecules (Lee, et al., 2003), for example, the local media composition would change in large surface contexts. It has been shown that closed-channel PDMS systems could impede the growth and survival of neurons at a very low cell density (Millet, et al., 2007). Uncrosslinked PDMS oligomers may also interfere with the growth of cells (Regehr, et al., 2009) in systems with large SAV ratios.

One more notable feature as the size reduces is that surface tension becomes more significant, which can be harnessed to drive the fluid flow. Based on the surface tension effects, a passive pumping method (Berthier and Beebe, 2007; Lynn and Dandy, 2009; Walker and Beebe, 2002) has been developed to pump fluids inside microfluidic systems. This spontaneous pumping method has become more popular for microfluidic cell cultures because it does not require expensive and complicated external equipment. This feature makes the whole cell culture system compact and readily compatible with conventional incubators so that it can help to avoid potential contaminations from the external devices.

1.4 Dissertation Overview

As pointed out above, microfluidic cell culture platforms have unique advantages over conventional *in vitro* cell culture techniques, which have been projected to have transformative impacts to *in vitro* cell biology studies. To date, however, most microfluidic cell culture platforms were still in the proof-of-concept phase (El-Ali, et al., 2006) and were far from widespread uses by the biological and clinical community at large even with all the unique capabilities and advantages. This is partly because the developed microfluidic systems were often targeted for specific applications not for general purpose in different biological studies. Moreover, many platforms still required a significant amount of engineering expertise to operate. A large number of connections to external instruments could also increase the chance of introducing contamination to the culture. To become a common tool in biological laboratories, microfluidic cell culture platforms should have several features such as low-cost and dispos-

able, simple to operate, compact and compatible with conventional cell culture practices, and suitable for various established biological approaches such as high-resolution confocal microscopy.

In this dissertation, several versatile and user-friendly microfluidic platforms have been presented, which have the potential for acceptance by a wide range of end users in different biological fields. The dissertation is organized as follows. Chapter 1 presents a brief overview of microfluidics for cell culture. Chapter 2 describes a microfluidic cell co-culture platform that integrates a microfabricated valve to achieve reversible separation and connection between two adjacent cell populations, which allows for separate culture, treatment of individual cell populations, and observation of cellular interactions under regulations. Microfabricated valves have been mostly used to control fluid flow (Studer, et al., 2004a; Thorsen, et al., 2002; Unger, et al., 2000) or help to sort or trap cells (Irimia and Toner, 2006; Studer, et al., 2004b). Here a microfabricated valve made of a polymer barrier is used as a spacer to isolate two cell populations in close vicinity. Chapter 2 also presents the application of this novel cell co-culture platform to cell biology studies of central nervous systems (CNS) neurons. More specifically, two groups of hippocampal neurons are cultured and transfected separately with different fluorescently tagged genetic molecules coding pre- and post-synaptic proteins for dynamic observation of synapse formation and plasticity. In addition, the platform has been used for glia-neuron co-culture, which has shown significantly different cellular behavior from the presence of glial cells. The successful bioassays demonstrate the great potential of the platform for studies of molecular signaling pathways and cellular interactions between different cell types.

Chapter 3 presents development of a modified version of the valve-enabled cell co-culture platforms and their applications to cancer biology studies. The cancer biology studies focus on cross-migration of 4T1 tumor cells and endothelial cells. Assay results indicate that cross-migration mediated by different molecules shows very different patterns and that tumor cell migration under normoxic and hypoxic conditions is significantly different.

Chapter 4 further explores the potential of the valve-enabled microfluidic platforms. An agarose-coupled valve barrier is integrated to study cell-cell interactions through soluble factors alone. A semi-permeable barrier including ligand traps provides an innovative approach for probing signaling pathways. 3D side-by-side cell co-culture is also demonstrated, which should significantly expand the applications of these microfluidic platforms.

Chapter 5 presents a method to create a stable concentration gradient in the cell culture region through introducing a pressure balancing fluidic circuit, which reduces the pressure difference between two flow streams coming from two passive pumps. This microfluidic system can generate a stable gradient after the two streams are repeatedly split, mixed and recombined in the microfluidic network. In addition, one more system is developed to create a stable gradient without substantial flow in the cell culture region; and therefore, cells will not experience significant shear stress on a 2D surface or in a 3D matrix.

Finally, Chapter 6 summarizes the completed work and discusses the prospective continued work in microfluidic systems for cell culture with microenvironment control.

CHAPTER 2

VALVE-ENABLED MICROFLUIDIC PLATFORMS FOR NEURONAL STUDIES

2.1 Motivation

2.1.1 Synapse formation

Synapses are highly specialized cell-cell junctions that allow for communications between neurons. CNS synapses are structurally composed of a pre-synaptic axonal terminal and a post-synaptic region which in the case of excitatory synapses is composed of dendritic spines (Li and Sheng, 2003; McAllister, 2007). The pre-synaptic terminal is packed with hundreds of synaptic vesicles (SVs) filled with the neurotransmitter glutamates. In response to an action potential, SVs fuse with the plasma membrane of the pre-synaptic terminal resulting in release of glutamates, which diffuse across the synaptic cleft, a 20~50 nm space, and bind to receptors on the post-synaptic terminal. The binding triggers a number of signaling cascades in the post-synaptic terminal and a sequence of events that either stimulates or inhibits the production of an action potential in the post-synaptic neuron.

Dendrites and axons are dynamic structures and their plasticity is thought to be the basis of cognitive functions such as learning and memory (Dunaevsky, et al., 1999; Gray, et al., 2006; Levy and Steward, 1979). Not surprisingly, abnormalities in these structures are associated with a number of neurological disorders including autism, mental retardation, schizophrenia, epilepsy, and Alzheimer's disease (Fiala, et al., 2002; Selkoe, 2002).

Synapse formation is a fast and dynamic process involving the assembly of hundreds of pre- and post-synaptic proteins into a highly specific structure (Craig, et al., 2006; Garner, et al., 2006; Li and Sheng, 2003; McAllister, 2007; Waites, et al., 2005). Initially, both axonal and dendritic filopodia contact their potential targets, which is a fleeting and transitory process. Some filopodia retract but some become stabilized, which is thought to be governed by cell adhesion molecules (CAMs) including integrins, cadherin and the immunoglobulin (Ig) superfamily of CAMs. The pre- and post-synaptic differentiation is triggered and cells obtain the ability to alter their cytoskeletons. The pre- and post-synaptic proteins (SVs, active zone proteins, glutamate receptors, post-synaptic density (PSD), scaffolding proteins) are recruited at the initial contact site. As these proteins accumulate, the nascent synapse grows larger and becomes structurally and functionally mature. One of the most dramatic morphogenetic changes occurs at the post-synaptic side during the maturation process. Synapses are initially proposed to form on dendritic shafts or filopodia, but later these synapses locate on dendritic spines (McAllister, 2007). Moreover, dendritic spines dynamically alter their morphology in mature synapses. There is also a strong correlation between the size of the spine and the strength of the synapse (Dillon and Goda, 2005). The time course of synapse formation varies from hours to days. Mature synapses can maintain for hours, days, or even years.

Studies of the molecular mechanisms of synapse formation heavily rely on imaging the presence of fluorescence-tagged proteins at synaptic contacts in cultured neurons. Particularly, recent progresses in imaging techniques such as image correlation spectroscopy (ICS), image cross-correlation (ICCS) and spatial-temporal image

cross-correlation spectroscopy (STICS) provide powerful tools to measure sub-microscopic protein distributions and their dynamics during the process of synapse formation (Petersen, et al., 1998; Wiseman, et al., 2004).

In these studies, the gene encoding a fluorescent protein is inserted in frame with the gene encoding the protein of interest yielding a chimeric product consisting of that protein with a fluorescent manner (Giepmans, et al., 2006). The ideal result is that the chimeric protein behaves in the same way as the untagged one but has fluorescence. The location, mobility, transport routes and binding interactions of these fluorescence-tagged proteins can be studied in live cells using start-of-the-art imaging technologies.

Foreign DNA can be introduced into live cells via either viral (transduction) or non-viral route (transfection). Compared to viral transduction, transfection is easier to operate and has been adopted in this dissertation. Transfection can be accomplished through either physical methods such as micro-injection and electroporation or chemical methods including artificial lipids, dendrimers, calcium phosphate, etc. (Luo and Saltzman, 2000; Mcneil, 1989). Among all these methods, transfection using a modified calcium phosphate is a simple, rapid and inexpensive choice (Zhang, et al., 2003). In calcium phosphate transfection, negatively charged DNA molecules interact with the calcium phosphate and form fine precipitate complexes. Once the complexes attach onto the cell's surface, they can be internalized by endocytosis.

Fluorescent imaging-based neuronal studies currently face a big challenge of cross-transfection particularly for molecules such as actins and cadherins that are found at both pre- and post-synaptic terminals. It would be of great advantage to be

able to separately tag proteins in the pre- and post-synaptic terminals with different fluorescent markers and observe the dynamics of these proteins in living cells. However, traditional cell culture techniques cannot fulfill this task because all cells are immersed in the same culture media so that it is difficult, if not impossible, to treat a selected group of cells without affecting the entire culture. The compartmentalization technique (Campenot, 1977; Ravula, et al., 2007; Taylor, et al., 2005) could potentially solve the problem; however, in all published literature, different compartments were always in communication in a certain way and a volume of culture media or transfection reagents, though small, could transfer from one chamber to the other, leading to cross-transfection. Recently, Taylor *et al*. (Taylor, et al., 2010) demonstrated that they could infect neurons in the pre- and post-synaptic chambers separately with green fluorescent protein (GFP) and red fluorescent protein (RFP) by Sindbis virus using a multi-inlet microfluidic system. However, this device required three pumps to function well. Moreover, the synapses were formed in long (900 μm) and slim microgrooves, making it difficult to study synapse formation at the primary sites.

2.1.2 Glia and their roles in the nervous system

Glia are important cells in the nervous system, which do not fire action potential as neurons. About 90% of the human brain consists of glia which play crucial roles in the nervous system (Allen and Barres, 2009). Traditionally, glia are thought to support neurons and maintain their proper function. In the CNS, for example, oligodendrocytes enwrap axons and speed up the electrical communication. Astrocytes associate neurons with blood vessels and then regulate the blood supply. As neuronal

activities increase, astrocytes send signals to blood vessels to boost blood flow. Astrocytes also remove excess ions and recycle neurotransmitters to maintain homeostasis in the brain. Recently, it was discovered that glia also played an active role in brain function. Studies showed that astrocytes could release transmitters that modulated neuronal excitability and synaptic transmission (Haydon, 2001; Volterra and Meldolesi, 2005). Moreover, astrocytes are also critical in synapse development, aiding synapse formation and elimination (Allen and Barres, 2005; Pfrieger, 2002). Soluble factors released by glia, such as cholesterol, promote synapse development (Mauch, et al., 2001). Direct intercellular contacts, such as integrin-mediated astrocyte-neuron contacts, was found to enhance synaptic formation (Hama, et al., 2004). In addition, glia were thought to be responsible for the elimination of synapses to refine the neural circuits. To provide insights into both glia-neuron interactions and the roles of glia in the activity of neuronal networks, it is essential to co-culture glia and neurons together and study the effects of glia on neuronal activities.

2.2 Microfluidic Platform Design and Fabrication

The microfluidic co-culture platform (Fig. **2.1**(**a**)) is composed of two layers of PDMS. The first PDMS layer includes two cell culture chambers which are connected by an array of microgrooves. The second PDMS layer, defining a control chamber, is aligned and bonded on the top of the first layer. Each cell culture chamber is connected to an upstream well and a downstream well through two microchannels. One Pyrex cloning cylinder is attached to each upstream well as the liquid medium reservoir. The pressure difference between the reservoir and the downstream (waste) well

generates a continuous fluid flow in each chamber, which is used to load cells into the chambers and to provide nutrition to the cells. This passive pumping method (Walker and Beebe, 2002) allows the whole microfluidic co-culture platform to be placed into a Petri dish so that potential contaminations from additional external instruments such as tubing and syringe pumps are avoided.

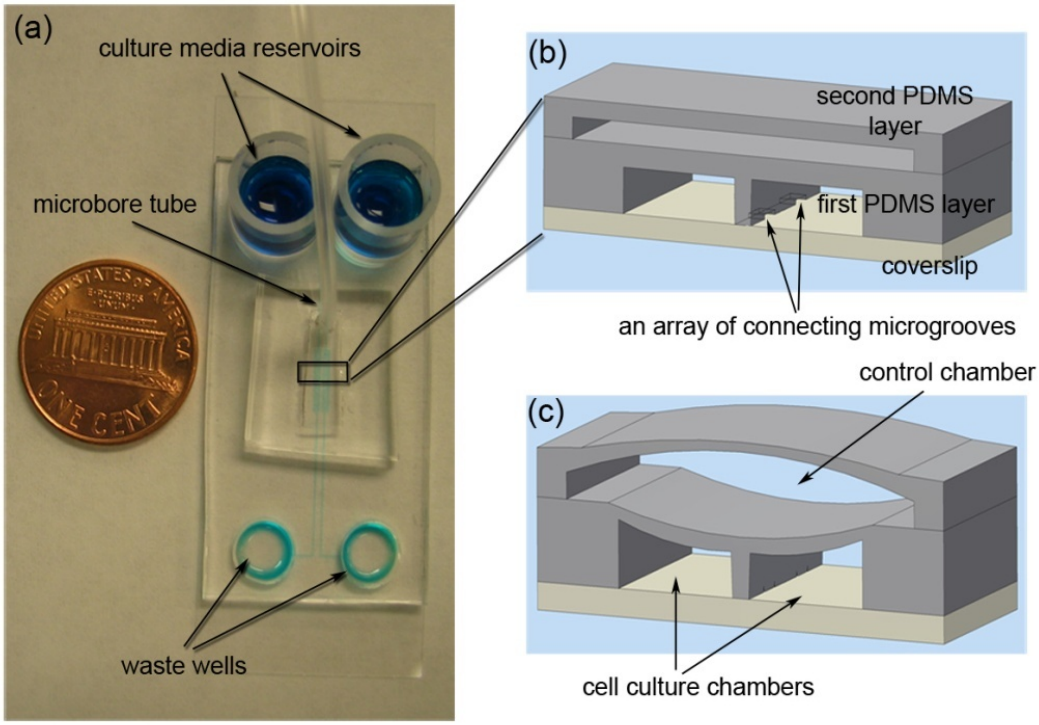

Figure 2.1: The design and operation mechanism of the co-culture platform for cell-cell interaction studies. (**a**) A picture of a fabricated device. Note that the entire device is compact enough to be placed inside a traditional 75-mm diameter Petri dish. (**b,c**) Schematic diagrams showing the working mechanism of the platform. If no pressure is applied to the control chamber, the two cell culture chambers are connected by an array of microgrooves in the barrier (b). When sufficient pressure is applied to the control chamber, the microgrooves are sealed and the two cell culture chambers are isolated from each other effectively (c).

Communication between the two cell culture chambers is regulated by the pressure inside the control chamber. If the control chamber is not pressurized (having ambient pressure), the microgroove array connecting the two chambers is open and culture media can flow and/or perfuse through the connecting microgrooves (Fig. **2.1**(**b**)). However, if adequate pressure is applied to the control chamber by injecting air using a syringe through the microbore tube, the connecting microgrooves are squeezed and then sealed, which effectively isolates the two cell culture chambers from each other (Fig. **2.1**(**c**)). Under this state, treatment can be applied to cells in one chamber without affecting those in the other chamber. Once the pressure in the control chamber is released, the microgrooves are recovered so that the two cell culture chambers are connected to each other again.

The microfluidic platforms were fabricated by soft-lithography techniques using replica molding (McDonald and Whitesides, 2002; Xia and Whitesides, 1998). The fabrication process is depicted in Fig. **2.2**. The master for the first PDMS layer consisted of two layers of negative-type photoresist SU-8 (Microchem, Newton, MA) (Fig. **2.2**(**a**)). Two transparency masks with a 20,000 dpi resolution were generated by a high-resolution printer (Cad/Art Services, Bandon, OR). The SU-8 2005 photoresist was first spun on a silicon wafer at a rate of 3000 rpm to coat the wafer with a thickness of roughly 5 μm. The silicon wafer was then soft baked, exposed through the first transparency mask, and developed to generate an array of photoresist lines (Fig. **2.2**(**a-i)**. The line dimensions were: width = 100 μm, length = 1 mm, and spacing = 200 μm) corresponding to the microgrooves. After cured at 95^{o}C for 20 min, the silicon wafer was spin-coated with approximately 100 μm thick SU-8 2050 photoresist at

a spinning speed of 1650 rpm. The silicon wafer was then soft baked and exposed through the second transparency mask which defined the cell culture chambers, the connecting channels (width = 200 μm), and wells. Since the pre-patterned thin array of photoresist lines (1 mm) were much longer than the spacing between the two cell culture chambers (20 – 200 μm), alignment was readily achieved through manual manipulation. The master for the first PDMS layer was finished with developing process and hard baking (Fig. **2.2**(**a-ii)**). The master for the second PDMS layer was simply obtained by attaching a slab of glass (dimensions: width = 4 mm, length = 12 mm, and height = 1 mm) to a silicon wafer (Fig. **2.2**(**b-i)**). A prepolymer of PDMS solution (Sylgard 184, Dow Corning, MI) was mixed with the curing agent at a 15:1 ratio and poured over the two mold masters. Spacers were used to make sure the thickness of the first PDMS layer to be 1 mm and the second layer to be 3 mm. Then the PDMS was degassed for 1 h and cured at 70^{o}C for another 2 h (Fig. **2.2**(**a-iii)** and **2.2**(**b-ii)**).

Before bonding, thin coverslips (No. 1, VWR Vista Vision, Suwanee, GA) were washed for 36 h with 15.8 N nitric acid and rinsed four times with DI water. After the solidified layers of PDMS were peeled from their masters, holes were punched using sharp punchers (Fig. **2.2**(**a-iv)** and **2.2**(**b-iii)**). The first PDMS layer was bonded to the acid-washed glass coverslip after the surfaces were treated with oxygen plasma, after which the second PDMS layer was manually aligned and bonded on the top of the first layer. Two Pyrex cloning cylinders (Fisher Scientific, Pittsburgh, PA) were attached to the loading wells as reservoirs for culture media and a microbore tube (Cole-Parmer, Vermon Hills, IL) was attached to the control chamber by gluing with liquid PDMS. The entire device was finally placed in an oven for 1 h at 75^{o}C to cure.

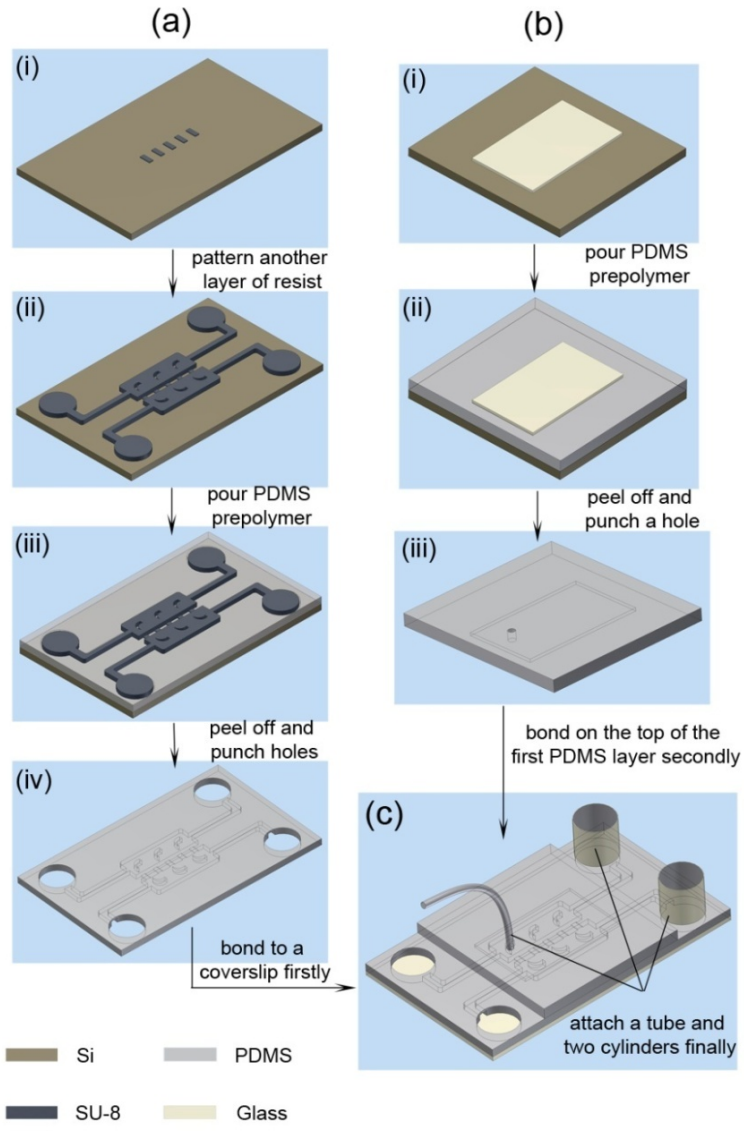

Figure 2.2: Schematics of the fabrication process. (**a**) Fabrication process of the first PDMS layer. (**a-i**) An array of SU-8 lines was patterned on a silicon wafer. (**a-ii**) The second layer of SU-8 was aligned and patterned to define the culture chambers and connecting microchannels, and wells. (**a-iii**) A prepolymer of PDMS was mixed with the curing agent and then poured over the mold. (**a-iv**) The solidified PDMS was peeled from the master and holes were punched. (**b**) Fabrication process of the second PDMS layer. (**b-i**) The mold was obtained by attaching a slab of glass onto a silicon wafer. (**b-ii, iii**) The following replica molding steps similar to those for the first PDMS layer. (**c**) A schematic of the final assembled microfluidic platform.

During curing, approximately 200 µl of sterilized deionized (DI) water was loaded into each reservoir to keep the microchannels filled, maintaining a constant flow in the channels to retain the hydrophilic nature of the PDMS channels. The microfluidic device was then sterilized under UV light in a tissue culture hood for 1-2 h before it was ready for use.

2.3 Device Characterization

2.3.1 Valve performance

Microvalves are one of the basic fundamental components in microfluidic devices, which have been used to control fluid flow (Abate and Weitz, 2008; Oh and Ahn, 2006; Studer, et al., 2004a; Unger, et al., 2000) or help to sort and trap cells (Irimia and Toner, 2006; Studer, et al., 2004b). Here we used an integrated mechanical valve to actively control the interaction between two adjacent cell populations. A pressure change in the control chamber was accomplished by injecting air (a pneumatic valve) or water (a hydraulic valve) through the microbore tube using a syringe. Characterization showed that pneumatic valves could successfully separate the two adjacent chambers for 4-6 hours while hydraulic valves could work for more than one week. This is because PDMS is a gas permeable material (Houston, et al., 2002; Merker, et al., 2000), which allows air to slowly leak through overtime. The leakage reduced the pressure in the air chamber continuously and eventually led to connection between the two cell co-culture chambers. Pneumatic control is easier to implement than hydraulic control because any air bubbles in the control chamber have to be care-

fully removed in the water injection process for the hydraulic valve to be effective over a long period of time.

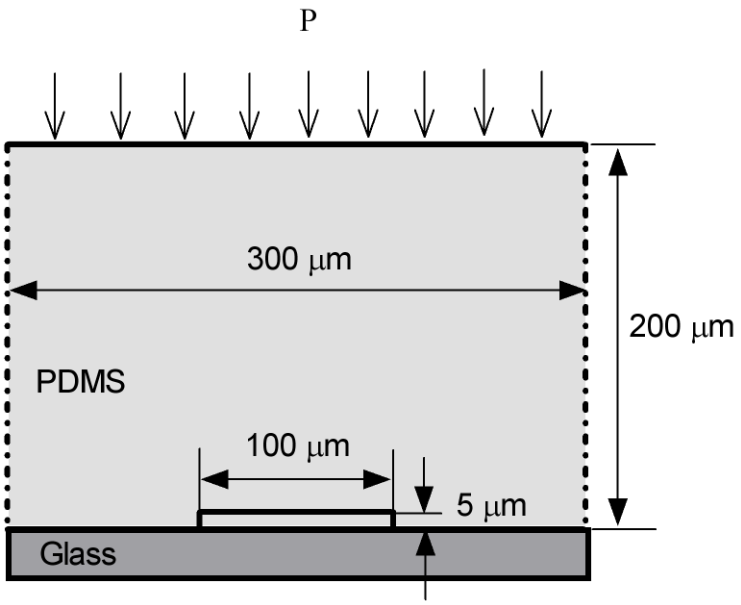

Figure 2.3: Computational model of the mechanical valve.

In order to gain insight into the microfluidic valve design, numerical simulations were performed using the finite element method (Ansys, Canonsburg, PA). The PDMS was modeled as a linear elastic material with a Poisson's ratio of 0.45 (Sasoglu, et al., 2007). Its Young's modulus depends on both the agent-to-base ratio and the baking time (Armani, et al., 1999; Fuard, et al., 2008; Lotters, et al., 1997). In the modeling two values of the Young's modulus (G), 5.5×10^5 Pa and 3.6×10^5 Pa were used, respectively, which correspond to the agent-to-base ratio of 1:12 and 1:15. Considering the periodically repeating nature of the microchannel array, only one microgroove was modeled as shown in Fig. **2.3**. There were two computational domains: a layer of PDMS (domain 1) sat on a slab of glass (domain 2). The bottom boundary of

the glass was fixed and a uniform pressure was applied on the top of the PDMS. Periodic boundary conditions were used on the left and right hand sides of the computational domains. Frictionless contact pairs were enforced between the bottom surface of the PDMS and upper surface of the glass.

The performance of the valve also depends on the thickness of the first PDMS layer. A PDMS membrane will become more flexible as its thickness decreases (Thangawng, et al., 2007). But there is a technical limitation to integrate an ultra-thin layer of PDMS in the cell culture platform. In the real device, the thickness of the first PDMS layer was about 1 mm. In simulations, however, a 200 μm thick computing geometry for PDMS was chosen to save the computational resources. Since the effect of PDMS thickness becomes notable as its thickness becomes comparable with the height of the microgroove, the 200 μm thick computing domain (40 times the height of the microgroove (5 μm)) was a reasonable choice. Based on the computational results, the shape change on the top was trivial in the overall deformation (Figs. **2.4** and **2.5**).

The computational results of the deformed configurations at different actuation pressures are shown in Figs. **2.4** and **2.5**. As predicted, a lower actuation pressure is required for more flexible PDMS. However, the valve cannot be completely closed for a microgroove having a rectangular cross-section. There always exists a deformed triangle hole at each vertical side of the microgroove (Fig. **2.4**(**b**) and Fig. **2.5**(**b**)). At the actuation pressure of 50 kPa, for example, the side and bottom edges of the triangle hole are 3 μm × 12 μm for the PDMS of an agent-to-base ratio of 1:12 and 2.5 μm × 7 μm for the PDMS of an agent-to-base ratio of 1:15. A higher actuation pressure will help to reduce the sizes of these holes. For example, for the PDMS of an agent-

to-base ratio of 1:15, the size of hole shrinks to 1 μm × 2 μm at a pressure of 100 kPa (Fig. **2.5(b)**). However, limitation exists for the maximum pressure applied to the control chamber due to the bonding strength between the two layers of PDMS and the mechanical strength of the base coverslip.

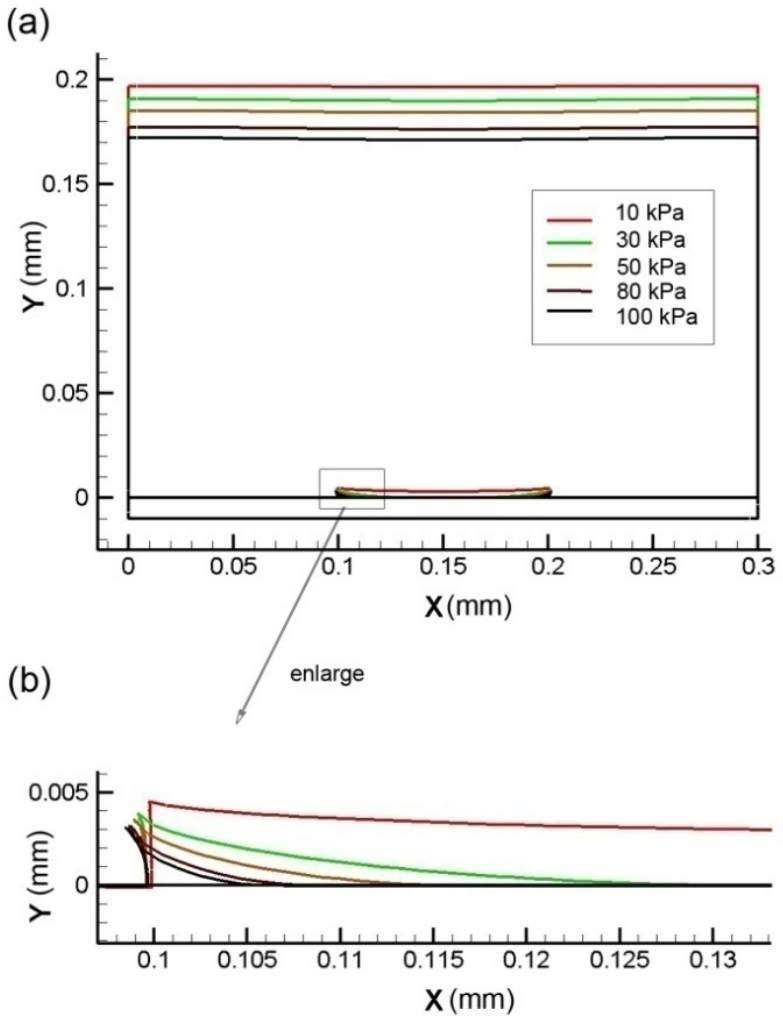

Figure 2.4: Computational results of the deformed configurations at different actuation pressures for the PDMS's agent-to-base ratio of 1:12 ($G=5.5\times10^5$ Pa).

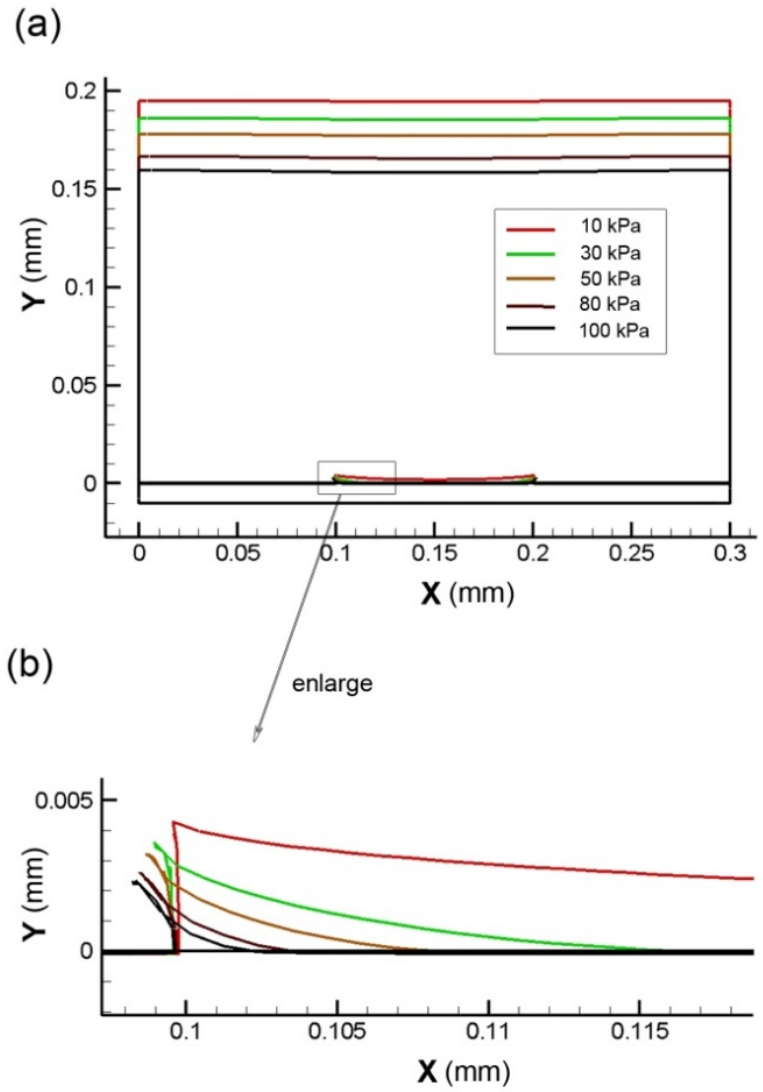

Figure 2.5: Computational results of the deformed configurations at different actuation pressures for the PDMS's agent-to-base ratio of 1:15 ($G=3.6\times10^5$ Pa).

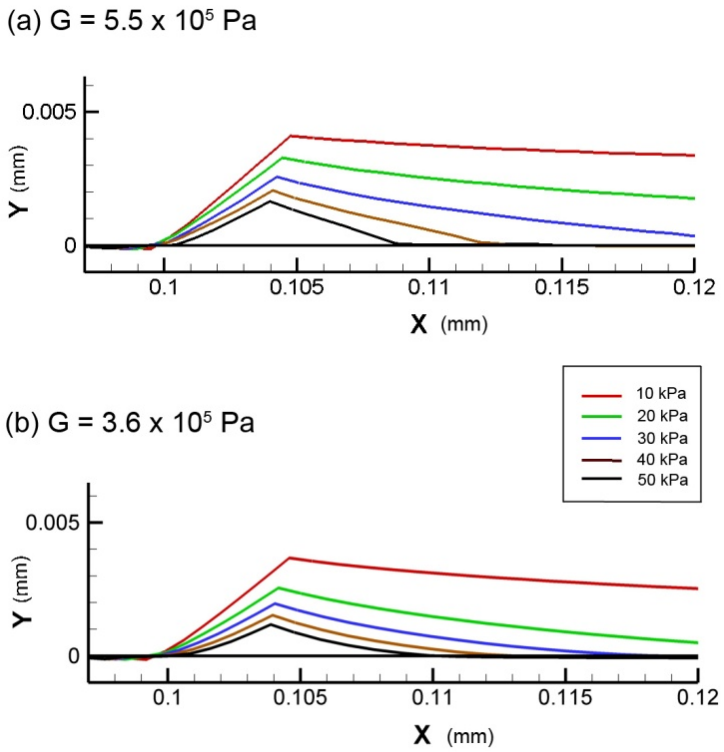

Figure 2.6: Computational results of the deformed configurations of microgrooves with sloped side walls.

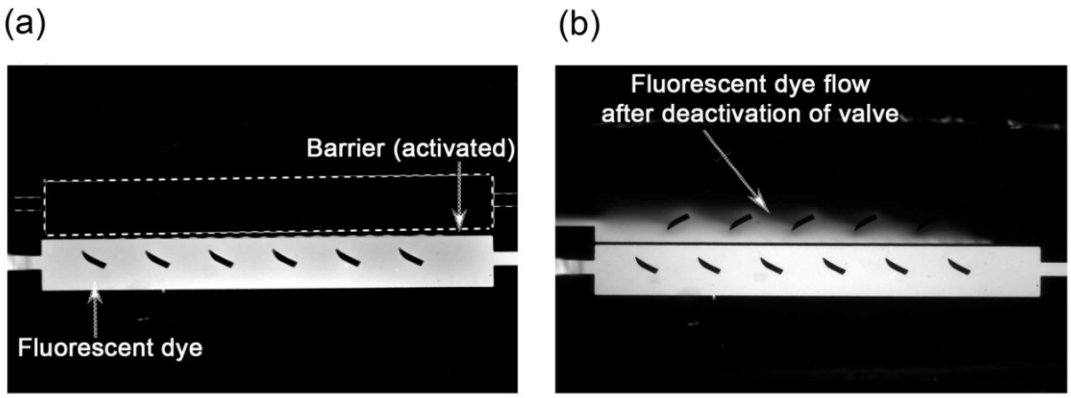

Figure 2.7: Fluorescent images after one chamber was filled with FITC. (**a**) The valve was activated and no fluorescent dye was detected in the adjacent chamber. (**b**) After the air was released from the control chamber, the FITC appeared in the other side.

In practice, the pressure inside the control chamber that can be achieved is about 30~50 kPa while the valve is activated. To reduce the size of the hole and obtain a better sealing, tapered SU-8 structures were fabricated using the overexposure technique (Chang, et al., 2007). Instead of the recommended dosage of 100 mJ/cm^2 by Microchem®, a dosage of 1,500 mJ/cm^2 was used to pattern the array of photoresist lines (the step shown in Fig. **2.2**(**a-i)**) resulting in microgrooves with sloped side walls. Figure **2.**6 shows the computational results of the deformed configurations of microgrooves with sloped walls, whose slope angle is 45^o. At the actuation pressure of 50 kPa, the side and bottom edges of the triangle hole are reduced to 1.6 μm × 7.5 μm for the PDMS of an agent-to-base ratio of 1:12 and 1.1 μm × 7.5 μm for the PDMS of an agent-to-base ratio of 1:15.

Even though the numerical simulation results show that there always exists small residue connections between the two chambers through the corners of squeezed microgrooves, the squeezed channels are of much reduced dimension and can effectively block the exchange of media between the two chambers (avoiding cross transfection and cell migration). To experimentally determine how well the valve separated the two cell culture chambers, we pressurized the control chamber and added fluorescent isothiocyanate (FITC) (Thermo Fisher Scientific, Rockford, IL), which is soluble in DI water at a concentration of less than 0.1 mg/ml, into one chamber. FITC was not detected in the other chamber after 4 h, indicating that the barrier valve effectively separated the two chambers (Fig. **2.7**(**a**)). In contrast, after the pressure in the control chamber was released and the microgrooves were recovered, FITC quickly

perfused into the adjacent cell culture chamber, indicating significant liquid exchange between the two chambers (Fig. **2.7**(**b**)).

2.3.2 Flow field

Because of the small size of the microfluidic channels, the Reynolds number is low and the flow is laminar in nature. If a hydrostatic pressure gradient is applied along the microchannel, a Poiseuille-type flow is generated, which is characterized by a parabolic velocity profile. To distribute the nutrition more evenly and to promote media exchange between the two chambers, several PDMS semi-lunar shaped supporters (shown in Fig. **2.1(a**)) were fabricated in each cell culture chamber. In addition, these supporters prevent large deformation of the roofs of the cell culture chambers when the control chamber is pressurized, which can be detrimental to cells. To better understand the flow characteristics inside the cell chamber, the flow fields were simulated using Fluent (Ansys, Canonsburg, PA), a computational fluid dynamics (CFD) software.

In the modeling, the chamber dimensions were taken as the same as those of the real culture device, which were 800 μm wide, 6.4 mm long and 100 μm high. The inlet condition was set as a constant volume flow rate of 1.2 μL/min (corresponding to an average velocity of 1 mm/s). Non-slip boundary conditions were applied at the walls. The simulations were three dimensional. Figure **2.8** plots the velocity magnitude at a slice 10 μm above the bottom surface. Comparing the two velocity fields, it can be seen that the velocity near the bottom surface is enhanced by these semi-lunar

shaped supporters. Asymmetric supporters also enhance the convection near the grooves, increasing the flow exchange between the two cell chambers.

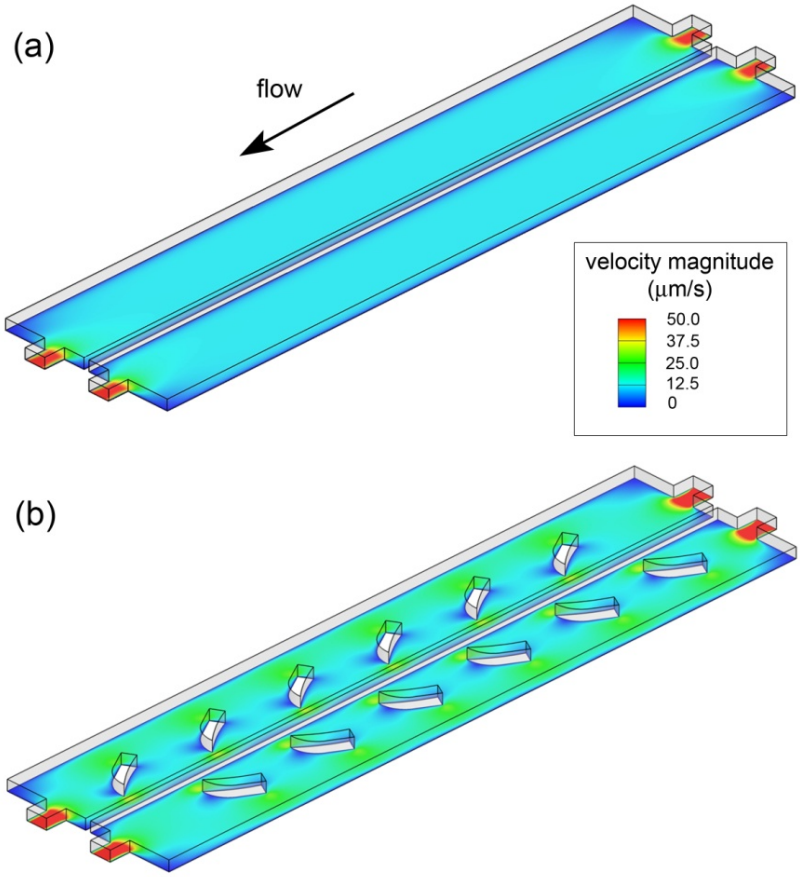

Figure 2.8: Simulation results of the velocity profiles in the cell culture chambers without **(a)** and with **(b)** asymmetric semi-lunar shaped supporters.

2.3.3 Passive pump

Even though flow generated by a syringe pump or an electroosmotic pump could have a better control with more accurate, stable, and adjustable volumetric flow rates, utilization of these pumping methods introduces external equipment and connections that are generally much larger. It renders the whole set-up incompatible with

conventional cell culture incubators unless special accommodations are implemented. The required extra effort usually hinders the widespread acceptance of these microfluidic platforms by the biological community. A simpler pumping method, therefore, can be very beneficial. In our microfluidic platform, Pyrex cloning cylinders were attached to the upstream wells as the liquid media reservoirs and the pressure difference between the reservoirs and the waste wells generated a continuous fluid flow through the microchannels and chambers. This usage of the passive pumping method (Walker and Beebe, 2002) ensured that the whole device was compact enough to be placed into a Petri dish and avoided potential contaminations from external instruments such as syringe pumps.

Precise prediction of the flow rate induced by passive pumping as a function of time is complicated because quite a few factors affect the flow rate collectively. These factors include the height of the liquid column in the media reservoirs and waste wells, surface wetting properties, air/liquid meniscus shapes, and evaporation, which are all functions of time and/or external environmental conditions. In fact, this inherent limitation of the passive pumping mechanism was one of the reasons why we chose to introduce the valve barrier to actively separate two chambers because it was very difficult to precisely balance the pressure of the two chambers over time to avoid the transverse flow between the two cell chambers. In the cell co-culture platform the flow rate changes over time, which is determined primarily by the menisci and the amount of liquid in the loading and waste reservoirs (Lynn, et al., 2009). Estimations of the pressure difference between the loading and waste wells for some ideal situations are discussed as follows.

Figure **2.9**(**a**) shows a configuration where the meniscus in the waste well is incomplete, corresponding to the case right after the liquid in the waste well is removed. The pressure difference across the microchannel in this case is largest and can be expressed as (Lynn and Dandy, 2009)

$$P_{\mathrm{A}} - \mathrm{P_B} = \gamma\left(\frac{\cos\theta_{\mathrm{B}}}{h} + \frac{1}{R_{\mathrm{B}}} - \frac{2\cos\theta_{\mathrm{A}}}{R_{\mathrm{A}}}\right) + \rho g H, \tag{2.1}$$

where γ is the surface tension between the liquid and air, θ is the contact angle, R is the radii of the reservoir, h is the height of the meniscus and H is the height difference between the loading and waste wells. The subscribe A and B represents the loading and waste wells, respectively. As the flow continues, the liquid volume in the waste well increases and the meniscus there becomes complete as shown in Fig**. 2.9**(**b**). For the complete meniscus, the pressure difference can be evaluated as

$$P_{\mathrm{A}} - P_{\mathrm{B}} = 2\gamma\left(\frac{\cos\theta_{\mathrm{B}}}{R_{\mathrm{B}}} - \frac{\cos\theta_{\mathrm{A}}}{R_{\mathrm{A}}}\right) + \rho g H. \tag{2.2}$$

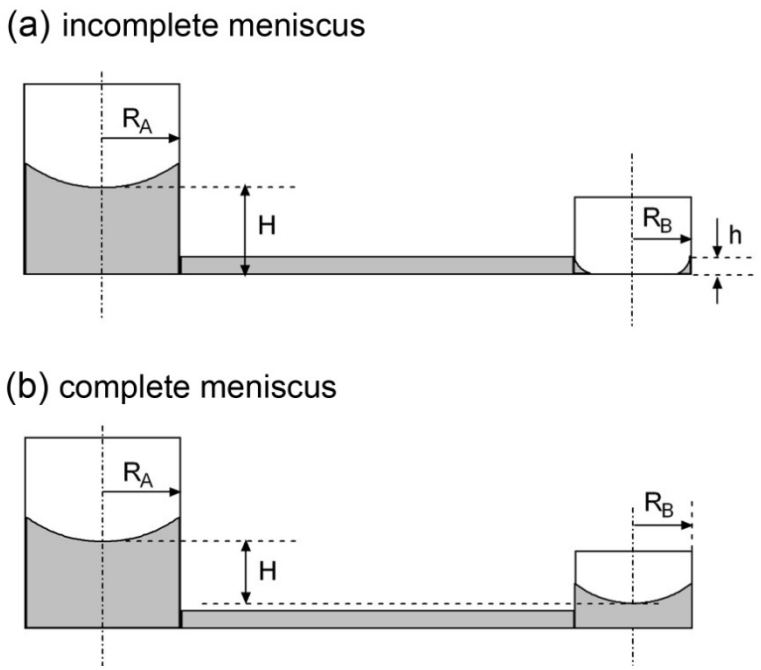

Figure 2.9: Schematics of the menisci to estimate the flow rate.

In one design of the microfluidic platform, for example, the reservoirs have the size of R_A = 4 mm and R_B = 2.5 mm, respectively. An approximate estimation of the flow rate at one time point is as follows. The surface tension is taken as γ = 70 mN/m and the contact angles are assumed to be the same for the glass and PDMS surface as $\theta_A = \theta_B = 30^o$. It is worth noting that after plasma treatment the PDMS surface becomes hydrophilic and the contact angle can be as small as 10^o for water-air interface. However, its wettability changes over time and the contact angle can increase up to 110^o, which means that PDMS recovers its hydrophobic nature. The height of the incomplete meniscus can be taken as h = 0.1 mm and the initial height difference is taken as H = 5 mm. Under these conditions, the pressure difference between the inlet and outlet will be about 1,119 Pa. This will generate an average flow velocity of 0.5 mm/s in the microchannels, corresponding to a volumetric flow rate of 0.6 μL/min in the microfluidic devices (The geometry of each chamber is the same as described in the previous section; the length, width and height of each channel is 12 mm, 200 μm and 100 μm, respectively).

If the waste well has a complete meniscus (Fig. **2.9**(**b**)), the flow velocity will be much reduced because the curvature of the interface is much smaller. Note that there still exists a continuous flow with an average velocity of 7.7 μm/s in the microchannel (9.2 nl/min in flow rate) even if the surface heights are the same for the inlet and outlet reservoirs (H = 0), as a result of the different size of the reservoirs. Every 1 mm height difference will contribute an additional velocity of approximately 4 μm/s (4.8 nl/min) in the microchannels. In our experiment, we found that even this low flow rate could provide enough fresh media exchange for cells to remain healthy.

2.4 Neuronal Study Results

2.4.1 Synapse formation

For synapse formation study, the microfluidic platform was first UV sterilized and then coated with poly-L-lysine (PLL) (Sigma-Aldrich, St. Louis, MO) by flowing 1 mg/ml PLL through the chambers for 12 h at 37^{o}C. To remove excess uncoated PLL, the chambers were washed with sterilized DI water for at least 1 h at 37^{o}C. The chambers were then washed with B27 supplemented Neurobasal™ media (GIBCO™ Invitrogen, Carlsbad, CA) containing L-glutamate to equilibrate the cell chambers. Following coating and washing, dissociated rat hippocampal neurons, which were isolated from E19 rat embryos, were re-suspended in B27 Neurobasal™ media at a density of 5,000 cells per microliter of media and loaded into each of the loading reservoirs by adding 15-20 µl of neuron suspension into the wells (Fig. **2.10**(**a**)). The microfluidic platform was then placed in a cell culture incubator with 5% CO_2 for 2-3 h at 37^{o}C to allow neurons to attach to the PLL-coated glass coverslip. When cells had visibly attached to the surface, approximately 300 µl of culture media was added to one loading reservoir and half of this volume was added to the other loading reservoir. This allows for sufficient flow rate through the microgrooves between the two chambers. Every 36-48 h, neurons were supplied with fresh B27 Neurobasal^{TM} media, which was conditioned over a monolayer of glial cells. At this time, the media were also aspirated from the waste wells. Neuronal culture can be maintained in this manner for at least several weeks.

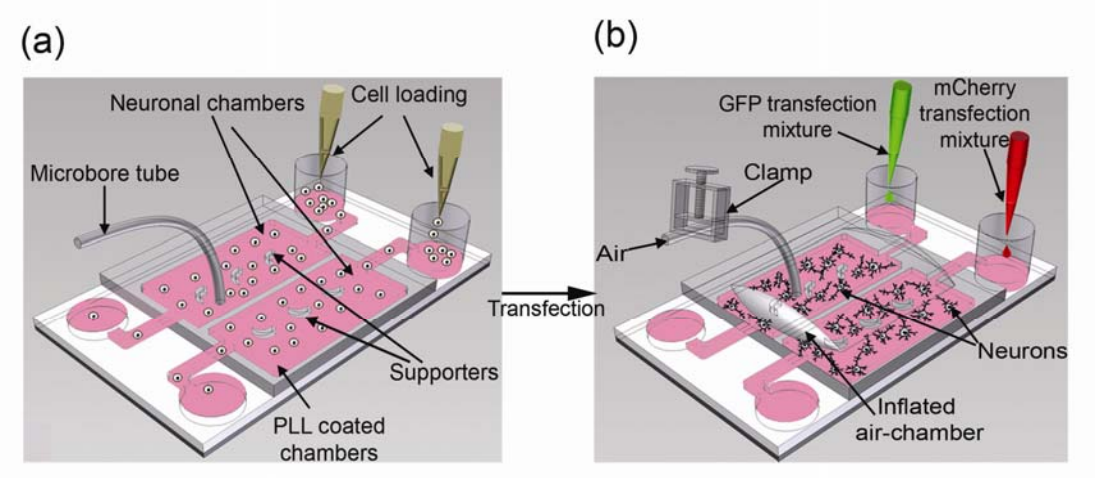

Figure 2.10: Schematics of cell loading and separate transfection.

Three days later the valve barrier was pushed down pneumatically to separate the two chambers. Neurons in the two chambers were subsequently transfected with different cDNA solutions for approximately 1.5 h using a modified calcium phosphate method (Zhang, et al., 2003). After the two chambers were isolated by injecting air into the control chamber, the transfection solution containing different cDNAs, one encoding GFP (green) and the other m-Cherry (red) fluorescent protein, were loaded into the two reservoir cylinders (Fig. **2.10**(**b**)). The cDNA-calcium phosphate precipitates were introduced into the respective chambers by continuous flow and some complexes were observed to attach onto the cell body surface, which was expected for a successful transfection. Since we found that a low, compared to a high flow rate led to an improvement in transfection efficiency, we added a drop of culture media into each waste well 10-15 min after loading the transfection solution to reduce the flow rate. The procedure consistently led to an approximately 40% transfection efficiency, which was significantly higher than the efficiency that we achieved on traditional culture

plates under identical experimental conditions (as shown in Fig. **2.13**). The chambers were then incubated with the transfection mixture for 1-1.5 h at 37^{o}C. After transfection, the DNA-calcium phosphate complexes were washed off and fresh culture media were filled into the loading reservoirs. A slight negative pressure was applied to the control chamber to release the valve barrier, allowing for neuronal processes from neurons in one chamber to contact neuronal processes from neurons in the other chamber.

When transfected neurons in each chamber were visualized by fluorescent microscopy, expression of the fluorescent proteins, GFP (green) and mCherry (red), was observed. Importantly, expression of mCherry was confined to the culture chamber that received the mCherry cDNA transfection solution and was not seen in the adjacent chamber; similar results were obtained with GFP. This indicated that the pneumatic valve successfully isolated the chambers and prevented transverse flow between the two chambers. Neurons with different fluorescent markers were observed to extend processes toward the opposite chamber. Neuronal processes (axons and dendrites) appeared to interact with each other across the two chambers (Fig. **2.11**(**a**)). To show that neurons formed synapses, cells in the device were immunostained for the SV2 (vesicle protein 2). A high-resolution image shows that the neuronal contacts did form synapses as indicated by the presence of SV2 clusters (Fig. **2.11**(**b**), yellow).

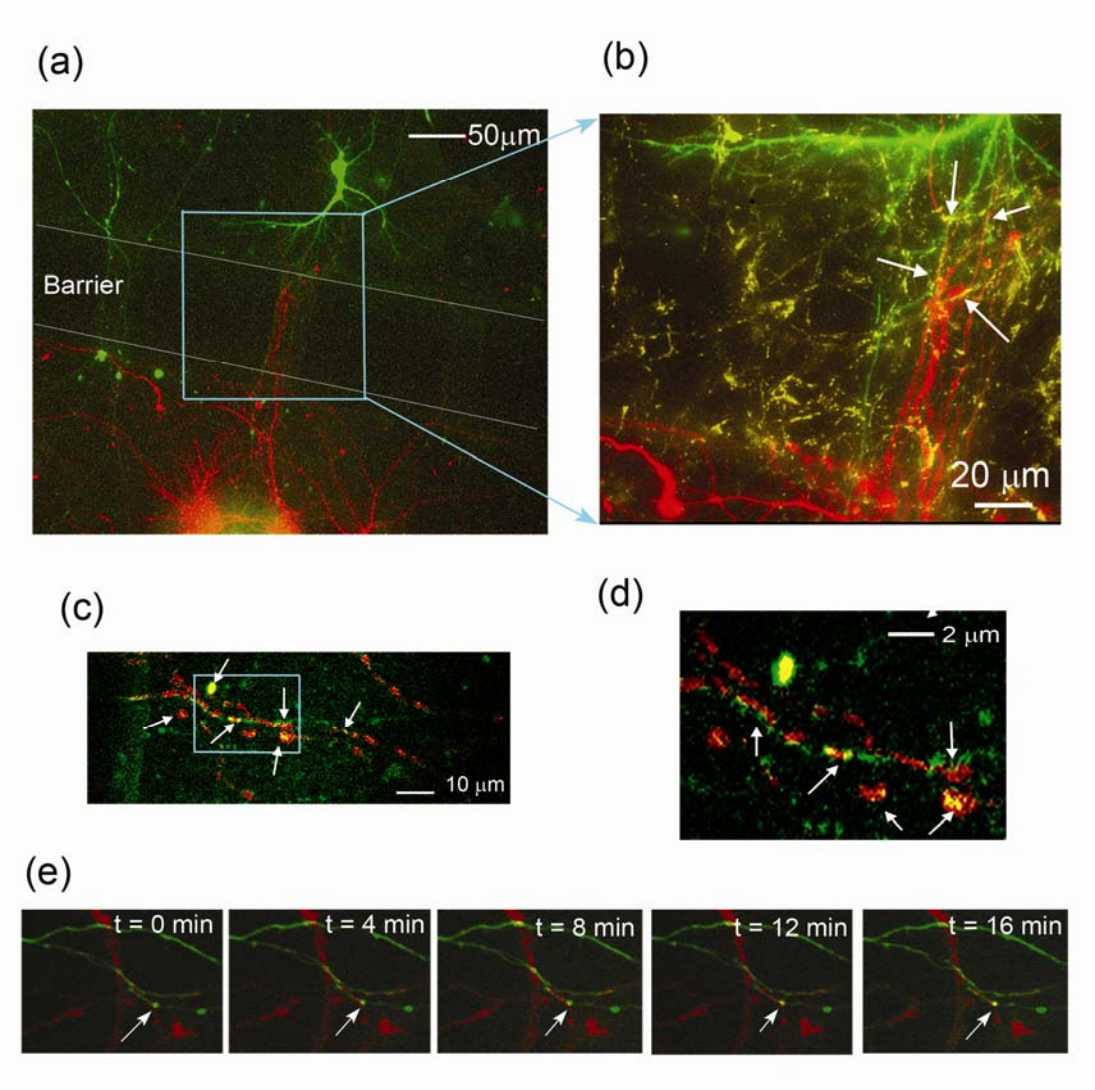

Figure 2.11: Images of neuronal processes in microfluidic chambers. (**a**) Neurons in one chamber expressed mCherry and neurons in the other chamber expressed GFP. (**b**) A high-magnification image of the boxed region in (**a**) after the neurons were immunostained for the synaptic marker SV2 (yellow). (**c**) A high-magnification image of the contact region. (**d**) Zoom-in view of boxed region in (c). (**e**) Time lapse images show a synapse forming (yellow puncta, arrowhead). Arrows in these images point to synapses. Because one terminal is green and the other is red, there will be a yellow spot when the two colors approach to each other

To demonstrate the capability of dynamic observation of synapse formation, neurons in the two chambers were transfected to express fluorescently tagged pre-and post-synaptic proteins, mCherry-synaptophysin and GFP-post-synaptic density protein-95 (GFP-PSD-95), respectively. We then mounted the microfluidic platform onto the confocal microscope to exam the neuronal process. The microfluidic chambers were maintained at 37^{o}C under humidified conditions. Confocal microscopy was performed on Quorum WaveFX spinning disk confocal system attached to a Nikon Eclipse Ti microscope with a PlanApo 60X TIRF objective (NA 1.49). Examination results did show that neuronal processes from the two chambers contact each other to form synapses, as shown in Fig. **2.11 (c)** and **(d)**. We then perform live-cell imaging, which lasted 12 hours with 4 min intervals. As shown in Fig. **2.11**(**e**), we imaged a neuron expressing mCherry-synaptophysin forming a synapse with a GFP-PSD-95 expressing neuron, suggesting that we can dynamically image synapse formation using these platforms. This ability will allow us to study the functions of various molecules that are considered important to CNS synapse formation.

2.4.2 Side-by-side neuron-glia co-culture

In the brain, the complex interdependency between neurons and glia is essential for the growth, development, differentiation, and functionality of these cells (Bains and Oliet, 2007; Pfrieger, 2009). An obstacle for studying neuron-glia interactions is the lack of available methods that can provide a controlled environment to fostering communication between these two cell types. The microfluidic platform could function in this capacity because it allows for culture of different cell populations with

their respective optimal microenvironment as required for glia and neurons. For example, glial cells are typically grown on laminin- or collagen-coated surfaces with serum containing minimal growth media while neurons are attached to PLL and require different growth media.

To set up co-cultures, the two chambers were first isolated using the hydraulic valve. The neuronal chamber was coated with PLL as described above. The glial chamber was coated with 10 μg/ml type I collagen (BD Biosciences, San Jose, CA) for 12 h at 37^{o}C. After coating, excess PLL and collagen were washed away by sterilized DI water. The glia were isolated from the brains of post-natal day 2 pups (Goslin, et al., 1998). Approximately 30,000 glia in 75 μl of Minimum Essential Medium (MEM) (Invitrogen, Carlsbad, CA), containing 10% horse serum and penicillin/streptomycin (Invitrogen, Carlsbad, CA), were first loaded into the glial chamber. After maintaining the culture for 2-3 days, glial cells typically reached 80% confluence, which was sufficient to support the growth of neurons. Then the neurons were isolated and loaded as described in section **2.4.1**. After the neurons attached and spread, the two chambers were connected (Fig. **2.12**(**a**)). Fresh neuronal media was added to the reservoir for both the glial (300 μl) and the neuronal (100 μl) chambers. The culture media level of the glial side was kept higher than that of the neuronal side to introduce a media flow from the glial chamber to the neuronal chamber.

In the absence of glial cells or glia-conditioned media, neurons were not healthy and could not survive for more than a week. In the co-culture platform, however, cells in both chambers were kept healthy and viable for the entire duration of our

experiments (more than 3 weeks), indicating that glial cells provide necessary nutrients for neuronal survival (Fig. **2.12** (**b-d**)).

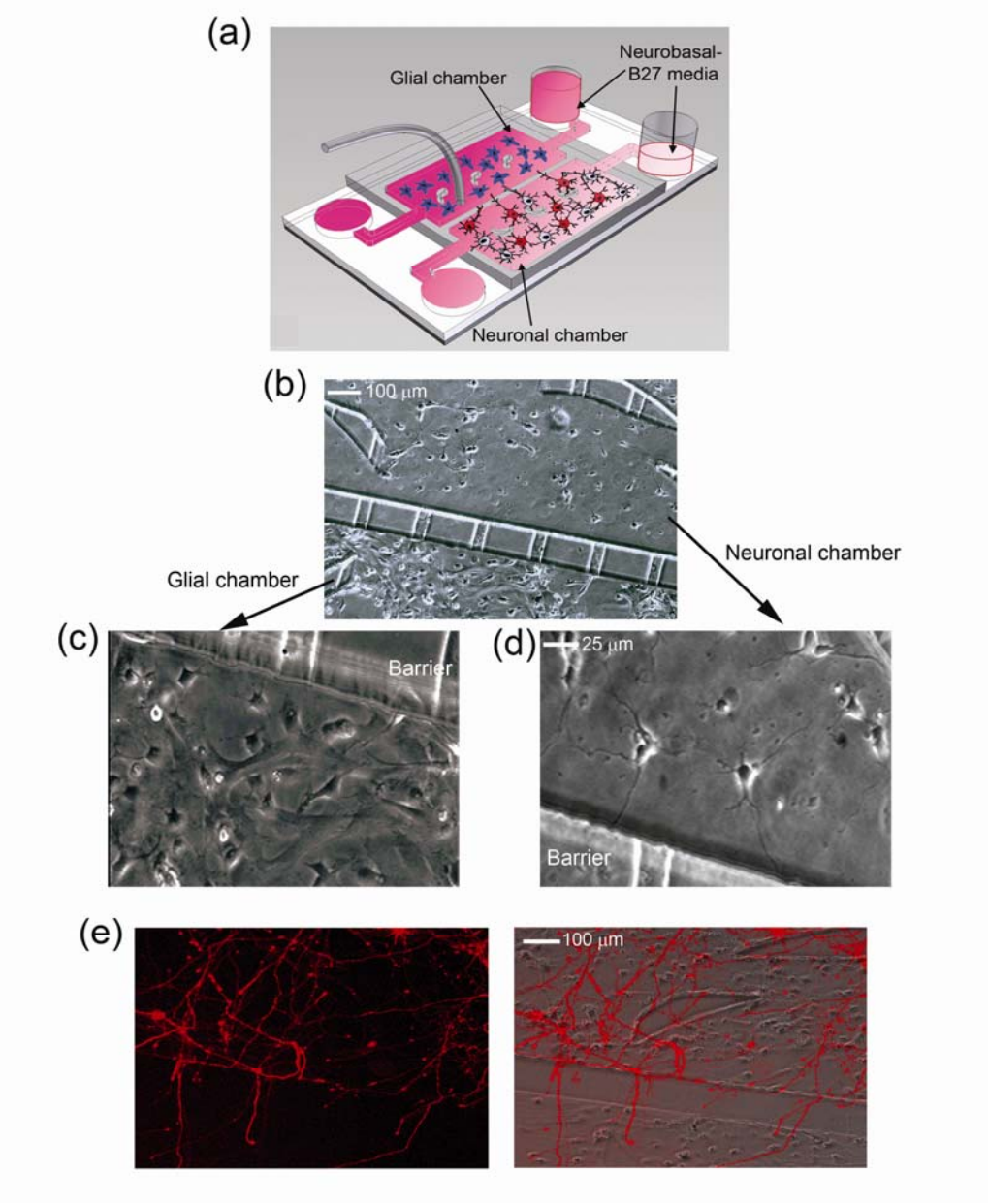

Figure 2.12: Co-culture of neurons and glia in the microfluidic platform. (**a**) A schematic showing the co-culture of neurons and glia. (**b**) Images of neurons and glia. (**c**,**d**) higher magnification images of glia and neuron culture. (**e**) A fluorescent image (left) and fluorescent/phase overlay (right) of neurons expressing mCherry.

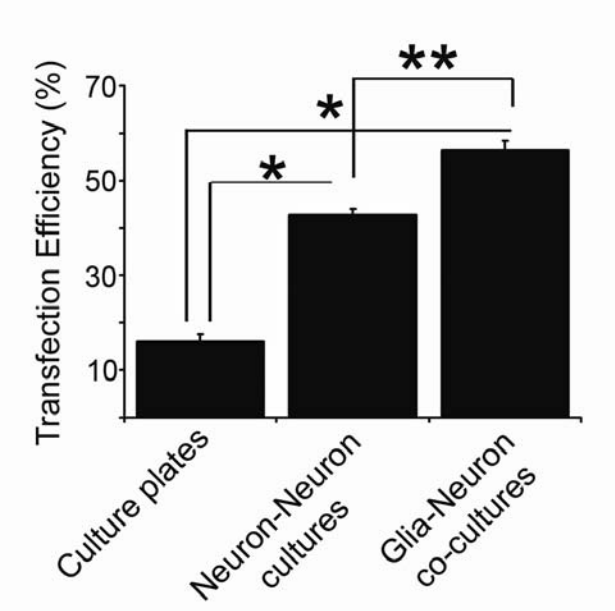

Figure 2.13: Transfection efficiencies for neurons cultured in traditional culture plates and in microfluidic platforms containing neuron-neuron and neuron-glia cultures. Error bars represent S.E.M. for 30-40 neurons from three separate experiments(*$p < 0.0001$; **$p < 0.001$).

Transfection of neurons in the co-culture chambers was also performed to demonstrate the feasibility of these experiments and as an additional index of the health of neurons since unhealthy neurons are difficult to survive during transfection. After transfection, neurons were healthy and extended axons and dendrites from the cell bodies, which in some cases crossed the barrier and grew into the adjacent chamber of glial cells (Fig. **2.12**(**e**)). The transfection efficiency is proportional to the cDNA number inserted inside the neuron's body with the precipitate complexes (Shin, et al., 2009). The slight flow would continuously bring new precipitate complexes to the neuron's surface and then increase the cDNA intake rate. But the flow rate should not be too large so that the complexes are washed away. Therefore, we added a drop

of culture media into each waste well 10-15 min after loading the transfection solution to reduce the flow. After neurons were transfected to express GFP or mCherry, the results show that the transfection efficiencies were increased in both the microfluidic chambers than the conventional culture plate which has stationary environment during transfection (Fig. **2.13**). In addition, the transfection efficiency was approximately 60% in the glia-neuron co-cultures, which most likely reflected the improved health of neurons when co-cultured with glial cells.

Collectively, these results show that neurons in the co-culture system are healthy and can be consistently transfected with high efficiency. Conditioned media contain undefined molecular components having long and short half-lives. Some components may degrade rapidly. For example, the half-life of neurotensin was measured as only 180 s with pleural cells (Cochrane, et al., 1991). Because the culture media flow from the glial to the neuronal chamber directly, this side-by-side co-culture system can conserve those fast degrading component secreted by glia. Therefore, neurons in this co-culture configuration are supposed to grow healthier. In addition, the integrated valve can isolate the two chambers. Individual treatment on one side will not affect the other side. We already took this advantage of the design to coat their respective optimal substrate molecules on each side and during transfection of neurons.

2.4.3 Quad-chamber side-by-side neuron-glia co-culture

The presented microfluidic platform provides a novel platform for studying neuron-glia interactions in the nervous system under physiologically relevant condi-

tions. Because these neurons in the co-culture system are healthier and can be consistently transfected with higher efficiency, the microfluidic platform was modified to study synapse formations in the presentence of glia. As shown in Fig. **2.14**, there are four cell chambers in the new and modified co-culture platform. The two inner cell chambers are used to culture neurons. The outside chambers adjacent to each of the neuronal chambers are used to grow glial cells to support the growth of the neurons. The four cell chambers are separated by three PDMS barriers under which microgrooves connected the respective two adjacent chambers (similar to the one shown in Fig. **2.1**). The open and close status of the microgrooves are modulated by a common control chamber. Once adequate pressure is applied to the control chamber, the microgrooves are squeezed and each cell chamber is isolated from others.

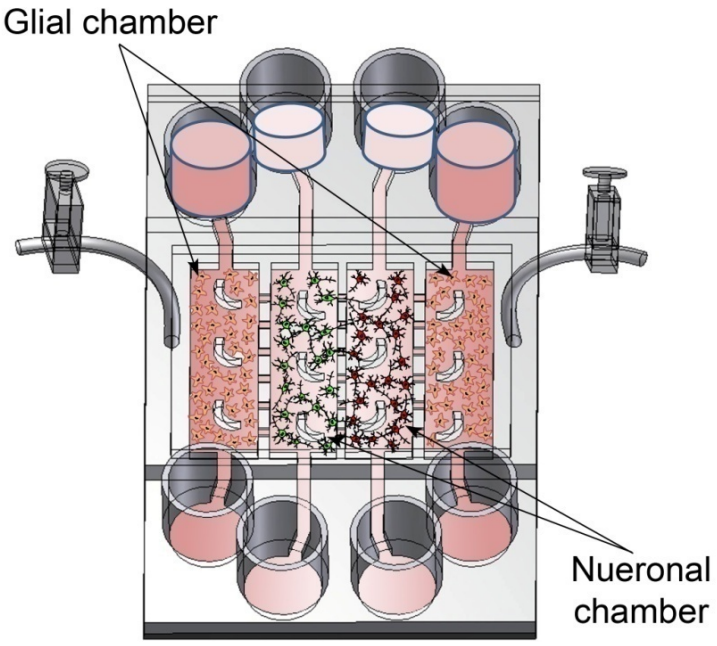

Figure 2.14: Schematic of the quad-chamber side-by-side neurons-glia co-culture.

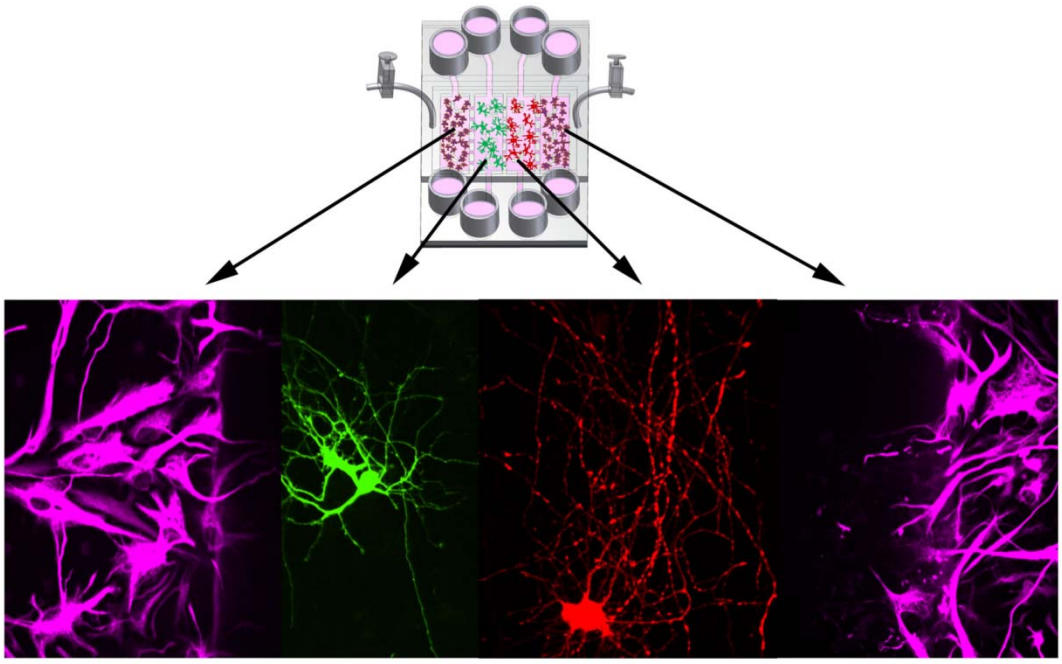

Figure 2.15: Fluorescent images of cells in the quad-chamber co-culture system. Neurons were transfected to express GFP and mCherry-synaptophysin in each neuronal chamber and Glial cells were stained by GFAP (Glial specific fibrillar acidic protein).

The neurons and the glial cells were cultured using a combination of protocols described in the sections **2.4.1** and **2.4.2**. In brief, the cell chambers were first isolated by applying a hydraulic pressure to the control chamber. The two glial chambers were coated with type I collagen while the two neuron chambers were coated with PLL. After coating, excess collagen and PLL were washed with sterile PBS or water. Subsequently, the glial chambers were equilibrated with glial media. The isolated and thawed glial cells (30,000 cells per chamber) were loaded into the glial chambers as described previously in section **2.4.2**. After the glial cells reached 80-90% confluence after 2-3 days in culture, the neurons were isolated and loaded into the neuronal chambers that were previously equilibrated with neuronal B27 media. Subsequently, the

liquid was released from the control chamber. Before releasing the control chamber pressure, all media from the glial and the neuronal chambers were removed by aspiration. The reservoirs that provided media to the glial chambers were filled with 500 µl of fresh B27 Neurobasal media. The reservoirs connected to the neuronal chambers were filled with 250 µl of B27 Neurobasal media. The culture media were added in each reservoir in this way such that there was a continuous flow of media from the glial chambers to the neuronal chambers through the microgrooves resulting in continuous supply of freshly glial-conditioned media to the neuronal cells. The media collected in the waste reservoirs were removed and the media reservoirs were replenished with the fresh media every 36-48 hours.

The four chambers were separated by three vale barriers, which were regulated by a common control chamber. Transfection could individually be conducted to the cells in each chamber as shown in Fig. **2.15**. For transfection of neurons, for example, the control chambers were re-pressurized to squeeze shut in order to separate the cell chambers at day 3 after loading neurons in culture. Neurons in the two inner chambers were transfected with different cDNA solutions as described in section **2.4.1**. When transfected neurons were visualized by fluorescent microscopy, synapse formations were shown to increase in the co-culture system, which will be discussed in the following section.

2.4.4 Vertically-layered neuron-glia co-culture

In last two sections, we showed that neurons are healthier when they are cultured side by side with glia than when cultured alone within the glial conditioned

media. In the quad-chamber side-by-side neuron-glia co-culture, the culture media was forced to flow through the microgrooves from the glial chamber to the neuronal chamber. To observe the interactions between neuronal processes with the presence of glial cells, we further developed another co-culture configuration in which the glia were placed onto the PDMS 'roof' of the chamber while the neurons grew on the co-verslip 'floor' as shown in Fig. **2.16**.

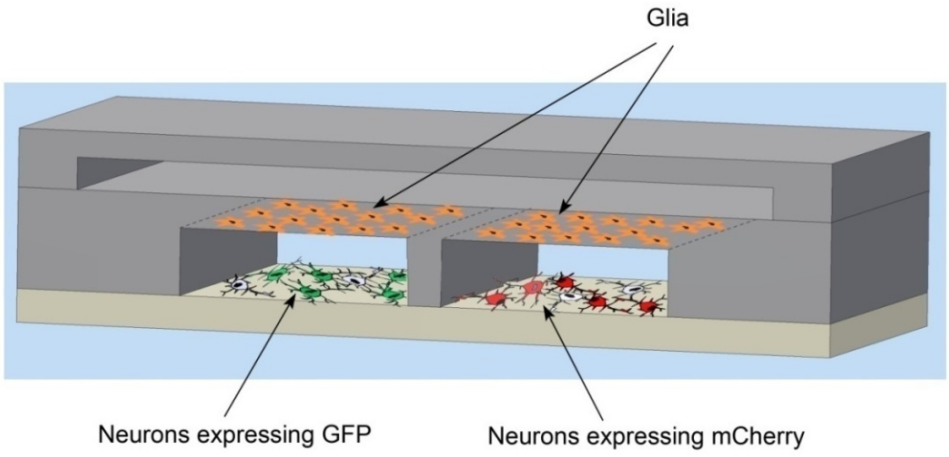

Figure 2.16: Schematic of the vertically-layered neurons-glia co-culture.

This innovative co-culture configuration allows intense crosstalk between two cell populations, which is representative of what happens *in vivo*. In the side-by-side configuration described in the last section, the interactions between two populations occur through a boundary. But the interactions and crosstalk occur through the whole surface in this vertically-layered configuration. In this vertically- layered design, the glia also receive feedback from neurons simultaneously and adjust their physiological responses according to the external microenvironmental conditions rapidly. Same as the side-by-side configuration, this configuration allows for separate transfections of

two groups of neurons with pre- and post-synaptic proteins, which enables us to observe synapse formation in a microenvironment much closer to the *in vivo* case.

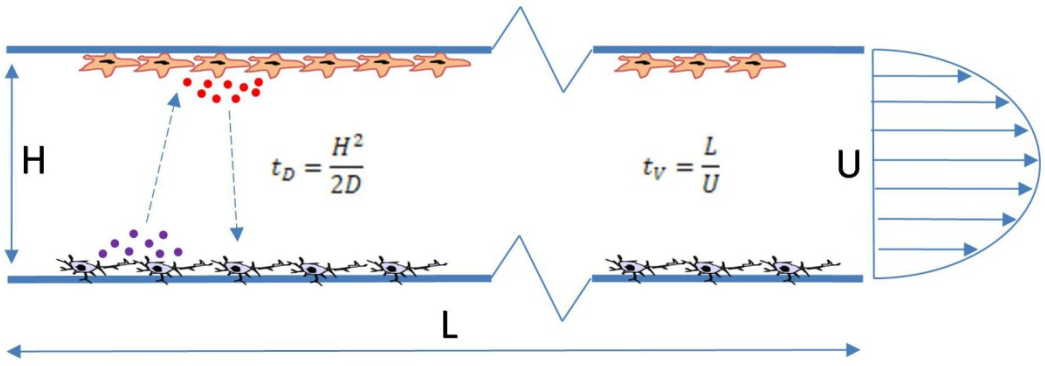

Figure 2.17: Intense crosstalks between the two cell populations.

The success of this co-culture configuration relies on the small length scale of the microfluidic platforms. Because of the small Péclet number involved, the microfluidic chamber is very efficient for mass transport. For example, the diffusion coefficient of nerve growth factor (NGF) was measured as D = 126 μm^2/s (Stroh, et al., 2003). The diffusion length (ℓ) can be simply estimated using the formula: $\ell = \sqrt{2Dt_D}$, where t_D is the time of diffusion. NGF would take about 40 s to diffuse across the 100 μm distance from the PDMS roof to the coverslip floor. As a result, molecules can reach the targets before being washed out of the chamber by the flow. We created a characteristic time ratio (ε) to describe this effect, which is the ratio of convection to diffusion,

$$\varepsilon = \frac{t_V}{t_D} = \frac{2DL}{UH^2}. \tag{2.3}$$

In the microfluidic platform, it takes about 20 - 60 min for the culture medium to flow through the cell culture chamber. Thus ε is in a range of 25 - 100 for NGF.

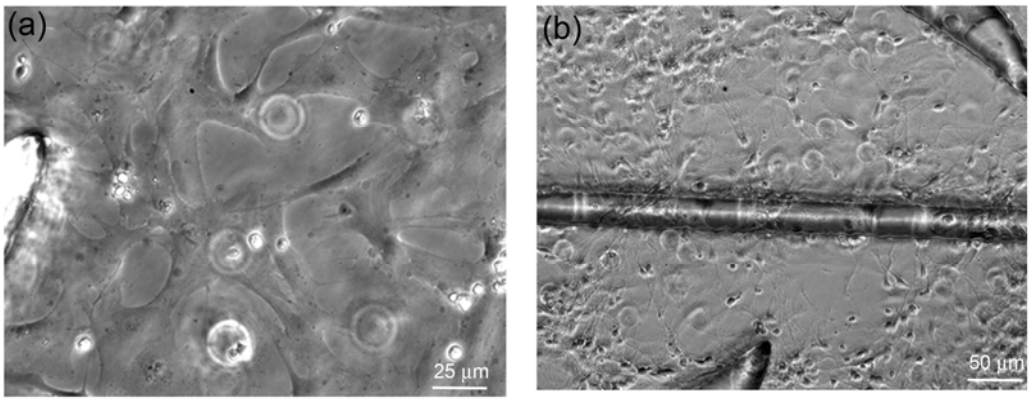

Figure 2.18: Phase contrast images of vertically-layered neurons-glia co-culture.

The devices used in the vertically-layered co-culture system were the same as those described in section **2.4.1**. After being sterilized, the microfluidic device was coated with PLL as described before. After the chambers were equilibrated with B27 supplemented Neurobasal^{TM} media, approximately 30,000 glia in 75 µl of MEM supplemented with 10% horse serum (both obtained from GIBCO® Carlsbad, CA) were loaded into both reservoirs. Immediately after loading, the platform was flipped upside down and placed into an incubator to allow for glia to deposit and spread on the PDMS surface that was also coated with PLL. Because only a small volume of medium was added in the each reservoir, the surface tension could hold the drop. Dripping of the medium from the reservoir was not seen after the device was flipped over. In addition, the flow rate was fast initially because of the incomplete meniscus in the waste wells (shown in Fig. **2.9**(**a**)). We did not see glia depositing on the coverslip before flipping. After 2 - 3 h, the platform was taken out of the incubator and excess

loading medium was removed from the reservoirs. The platform was flipped over again and fresh supplemented MEM was added. Glial cells typically reached 80-90% confluence after 2 - 3 days as shown in Fig. **2.18**(**a**).

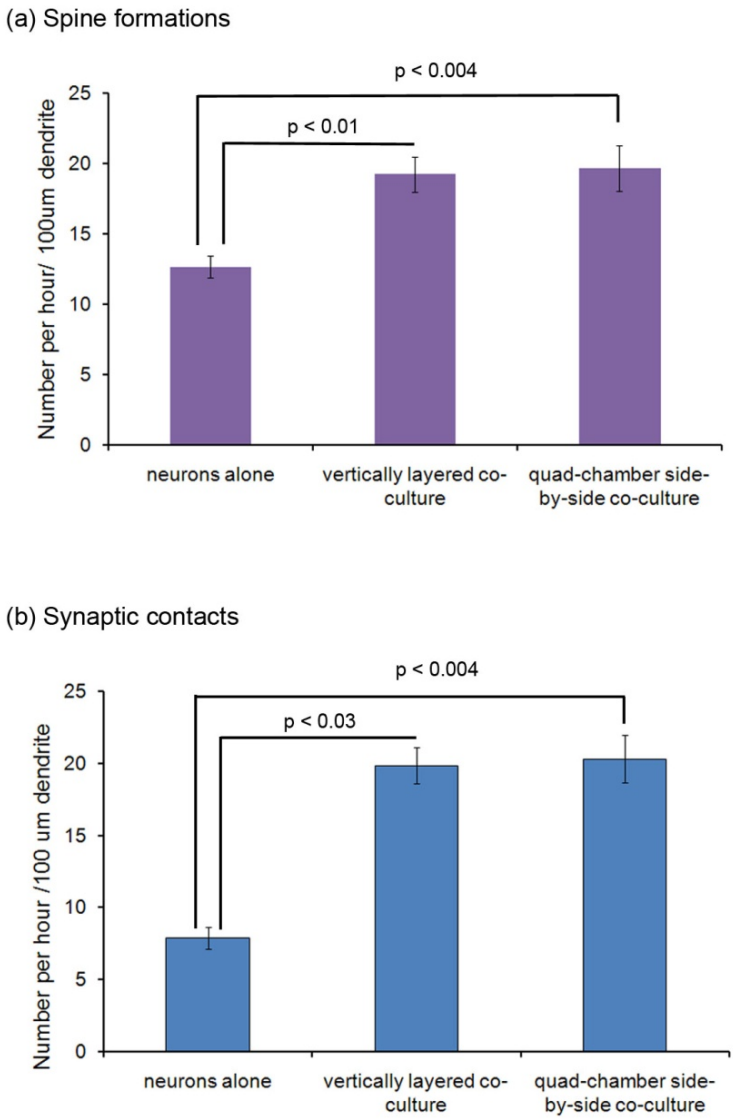

Figure 2.19: Quantification of number of spine formations and synaptic contacts in neurons cultured in three different microfluidic platforms. Error bars represent S.E.M. for neurons in three movies for neuron alone, six movies for quad-chamber side-by-side co-culture and four moves for vertically-layered co-culture from three individual separate experiments.

In the side-by-side co-culture scheme, we tried to coat the glass surface with PLL alone, but the glial cells did not grow healthily. Interestingly, the glial cells grew very well on the PLL-coated PDMS surface. After the glia reached 80-90% confluence, neurons were loaded, cultured and transfected separately in the microfluidic platform as described in section **2.4.1**. The neurons in this co-culture configuration is shown in Fig. **2.18**(**b**).

In addition to that the neurons could be transfected with high efficiency, more spines and synapse contacts were found in both neuron-glia co-culture systems compared with the system of neurons alone (Fig. **2.19**). Figure **2.19**(**a**) shows the average number of spines (visualized by GFP alone) along 100 μm dendrite per hour from living-cell images. More spine formation indicates healthier and more active neurons. Combined with higher transfection efficiency, the number of observed synaptic contacts (visualized by both GFP and mCherry) also increased about 2.5 fold. More synaptic contacts shown in one field of view of the live-cell images will facilitate future study of synapse formations visualized by fluorescent proteins.

In conclusion, both side-by-side culture and vertically-layered co-culture provide powerful techniques for investigating synapse formation in living cells. In the vertically-layered co-culture, the cellular interactions are intense and bi-directional. But the side-by-side co-culture allows glial cells to be separated from neurons and treated individually, independently of the neurons. Both co-culture configurations will provide opportunities for interesting investigations into the roles of glial cells in synapse formation and other neuronal activities.

2.5 Summary

We have constructed a valve-enabled microfluidic cell co-culture platform that permits separate control and manipulation of the microenvironment of different cell populations and allows for real-time imaging of cell-cell interactions. Numerical simulations were performed for the behaviors of the valve and the flow fields inside the culture chambers. A theoretical model was developed to predict the flow rate induced by the passive pumping method in the platform.

We used the platform to study synapse formations between hippocampal neurons. Results indicated that the platform provides a highly adaptable system for studying dendritic spine morphology and synapse formation in the CNS. By combining the platform with advanced microscopy, it is possible to measure the dynamic interactions of synaptic proteins in CNS spines and synapses as they develop.

We also presented two configurations, side-by-side and vertically-layered, for co-culturing glial cells and neurons, which provide new opportunities for investigating the complex interactions between these two cell types. The neurons are observed to be healthier in the presence of glia than cultured alone within glia-conditioned media, indicating the complex microenvironment in the co-culture not captured from the glia-conditioned media.

Although the described development only enabled studies of cell-cell interactions between two cell populations, the technology can be easily extended to study multi-cell populations in multiple chambers separated by individually controlled valves. Beside glia-neuron co-culture, these microfluidic co-culture techniques can be used to study interactions of other cell populations.

CHAPTER 3

MICROFLUIDIC PLATFORMS FOR TUMOR BIOLOGY STUDIES

3.1 Introduction

A tumor is a heterogeneous and structurally complex mixture of several cell types within a specific ECM. The cellular components include abnormal cells which define the tumor compartment itself as well as surrounding specialized cells such as fibroblasts, inflammatory cells, and endothelial cells (ECs) (Bhowmick and Moses, 2005; Mueller and Fusenig, 2004). These specialized cells and the specific type of ECM define a connective-tissue framework of the tumor called the tumor stroma (Mueller and Fusenig, 2004). The evolving crosstalks among different cell types and their surrounding ECM play a crucial role in carcinogenesis (Liotta and Kohn, 2001; Tlsty, 2001).

Recent work has shown that cancer-associated fibroblasts (CAFs) are important contributors to tumor formation and progression (Bhowmick, et al., 2004b; Kalluri and Zeisberg, 2006; Micke and Ostman, 2004). In fact, fibroblasts (e.g. loss of transforming growth factor-β (TGFβ) signaling) isolated from tumor tissue could convey malignant transformation to otherwise benign epithelial cells (Bhowmick, et al., 2004a; Kuperwasser, et al., 2004). Another example is the cross-talk between tumor cells and host vasculature endothelium, which is critical in tumor growth, progression, and ultimate metastasis (Coleman and Ratcliffe, 2009; Kaelin, 2008). Migration of both cell types is a key component of vascular recruitment through the process of an-

giogenesis as well as transendothelial cell migration in the processes of intravasation and metastasis (Li, et al., 2000).

A hurdle to dissect the respective contribution of these processes in tumor migration is the lack of appropriate co-culture platforms. Most existing co-culture platforms either mix two cell types or seed one type of cells on the confluence layer of the other (Bhatia, et al., 1997; Kane, et al., 2006; Samoszuk, et al., 2005). The lack of initial spatial separation makes it difficult to interpret the nature of their interactions. Additionally, stromal cells and tumor cells generally require very different culture conditions *in vitro*. In existing co-culture conditions, e.g. transwells, these cells are placed in a single culture environment that is sub-optimal for both cell types. Furthermore, stromal cells and tumor cells often become activated and are further modified by each other once they are cultured together. When and where their extensive crosstalks occur is currently beyond control.

3.2 Microfluidic Platforms with Etched Glass Slides as Substrates

A modified version of the presented microfluidic co-culture device provides an effective platform to study the relationships between stromal cells and tumor cells in a controlled manner. The two cell types are initially cultured in the two separate chambers with their own respective optimal culture medium. At this stage, the valve barrier separating these two chambers is pushed down tightly to prevent any communication between the two cell populations. At a desired time point, for example, after both cell types achieve confluence or the tumor cells are treated by an anti-cancer therapeutic drug, the barrier can be lifted up to allow for crosstalks. In this way the co-culture

platform acts as a powerful tool to study fundamental biological interactions between tumor cells and stromal cells as well as a screening tool to test the effectiveness of anti-cancer drugs.

To increase the opportunity for the two cell populations to interact with each other, we replaced the PDMS valve barrier with parallel microgrooves at the bottom with a solid PDMS barrier, which sat on an etched glass substrate to create a continuous gap between the two cell populations as shown in Fig. **3.1**. This modification, in addition to increase the cell-cell interaction routes, helps to completely separate the two cell populations when the valve barrier is pushed down since there are only two rounded corners at each end of the valve barrier from wet-etched region of glass slides.

In this version of the microfluidic platform, instead of a flat glass coverslip, a selected area of the glass coverslip was etched using buffered hydrofluoric acid (HF) (Fig. **3.1(a)**) to define a 1-16 μm deep cell culture region. Isotropic etching will leave tapered side walls (Wilson, et al., 1993). The new version also eliminates the requirement of two-step patterning for the mold of the first PDMS layer, which is now composed of a structure similar to that described in the last chapter without the array of microgrooves underneath the valve barrier. Therefore, the two chambers in the first PDMS layer are separated by a PDMS valve barrier with a flat bottom surface. Before bonding all surfaces except the bottom of the valve barrier and the etched region on the coverslip were treated with oxygen plasma. This way, other than the contact between the valve barrier and the coverslip, the PDMS and the coverslip formed a strong irreversible bonding (Duffy, et al., 1998). Similar to the working mechanism of the platform described in section **2.2**, depending on the pressure in the control chamber,

the valve barrier can be either pushed down or released up (Fig. **3.1**(**c**, **d**)). In the 'up' position, the gap between the bottom of the PDMS valve barrier and the surface of the etched coverslip allows for interactions and communication between the two cell populations in the two chambers (Fig. **3.1**(**c**)). In the 'down' position, the valve barrier effectively isolates the two chambers for separate culture or individual treatment of each cell population (Fig. **3.1**(**d**)).

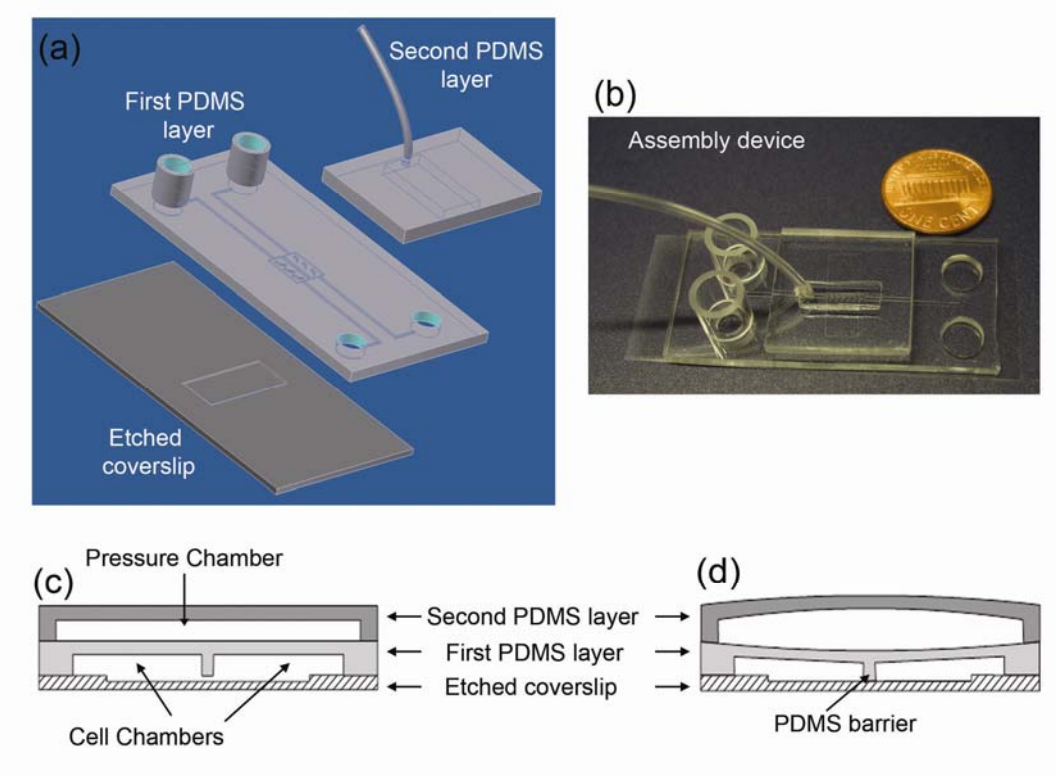

Figure 3.1: Schematics of microfluidic platforms for cancer biology studies. (**a**) A schematic of the main components. (**b**) A picture of the assembly device with a penny for size comparison. (**c, d**) Schematic diagrams showing the valve working mechanism. When the valve is inactive, a gap under the PDMS barrier allows for interactions and communication between the two cell populations (**c**). Upon activation of the valve, the two cell populations are isolated and cells in the two chambers can be treated separately (**d**).

Characterization showed that pneumatic valves could successfully separate the two adjacent chambers for 4-6 h while hydraulic valves could work for more than one week. This is because PDMS is a gas permeable material (Merker, et al., 2000), which allows air to leak through overtime; therefore the pressure in the air chamber is reduced gradually that leads to connection between the two chambers eventually.

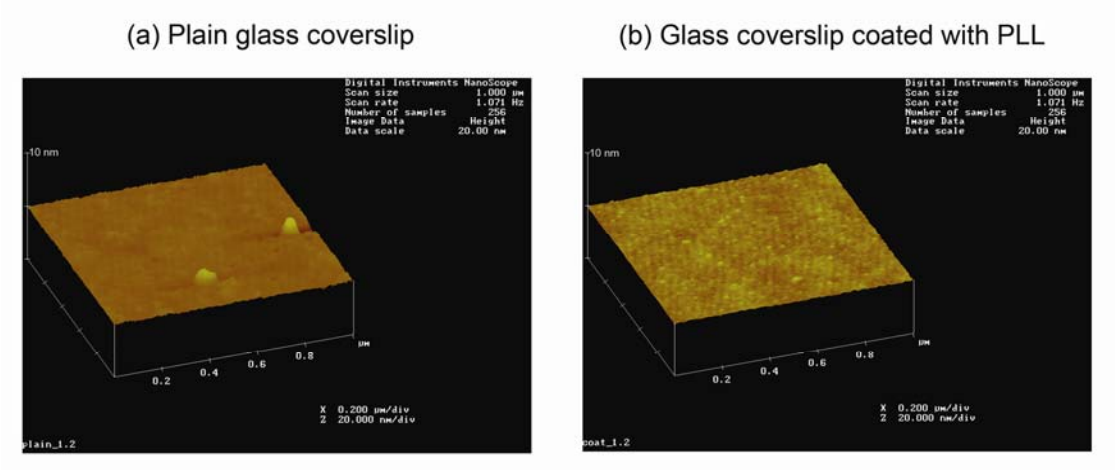

Figure 3.2: AFM images of a plain and PLL coated glass coverslip.

Without the plasma treatment, the glass coverslip and the PDMS come together and form a reversible bonding. It is easy to remove the PDMS piece from the glass coverslip as desired. During the device development, we have tried out another idea of bonding a PDMS construct including two separated chambers to a non-etched coverslip through reversible bonding. Cells were seeded in each chamber and allowed to grow. The PDMS construct could be peeled off from the coverslip at a desired time point, leaving the two cell populations on the substrate to interact with each other. However, the reversible bonding is not as tight as the irreversible one. To be effec-

tive, it is necessary to keep both surfaces of the coverslip and the PDMS ultra clean before bonding. This requirement is in contradiction to many cell culture practices that needs coated surfaces to support cell growth and migration. As shown in Fig. **3.2**, atomic force microscopy (AFM) studies show that the surface roughness of PLL coated coverslips increased significantly, which prevent a good reversible bonding. In addition, since the microfluidic devices are made over a thin cover glass, keeping the culture immersed in liquid media after the PDMS construct is removed becomes a challenge. Moreover, manipulating the flow in the PDMS microchannels and chambers allows us to control the microenvironment and media exchange between different cell populations. In the reversible bonding approach, this important capability is lost after removal of the PDMS construct.

3.3 Tumor angiogenesis under normoxic and hypoxic conditions

Angiogenesis, the formation of blood vessels, is an essential step in tissue growth, repair and regeneration, which covers the majority of human diseases. Angiogenesis is a multistep process that includes EC proliferation, migration, and assembly into vascular structures followed by the recruitment of smooth muscle cells to form mature and functional blood vessels (Coleman and Ratcliffe, 2009; Kaelin, 2008). Tumor angiogenesis is an integral process in cancer development as well as tumor metastasis (Haessler, et al.). The newly formed blood vessels not only transport nutrients and oxygen to tumors, but also provide routes for tumor cells to spread into different organs during metastasis. Tumor angiogenesis is initiated by tumor cells producing angiogenic growth factors, such as vascular endothelial growth factors (VEGFs),

which activate their cognate receptors on ECs and induces angiogenesis toward tumors.

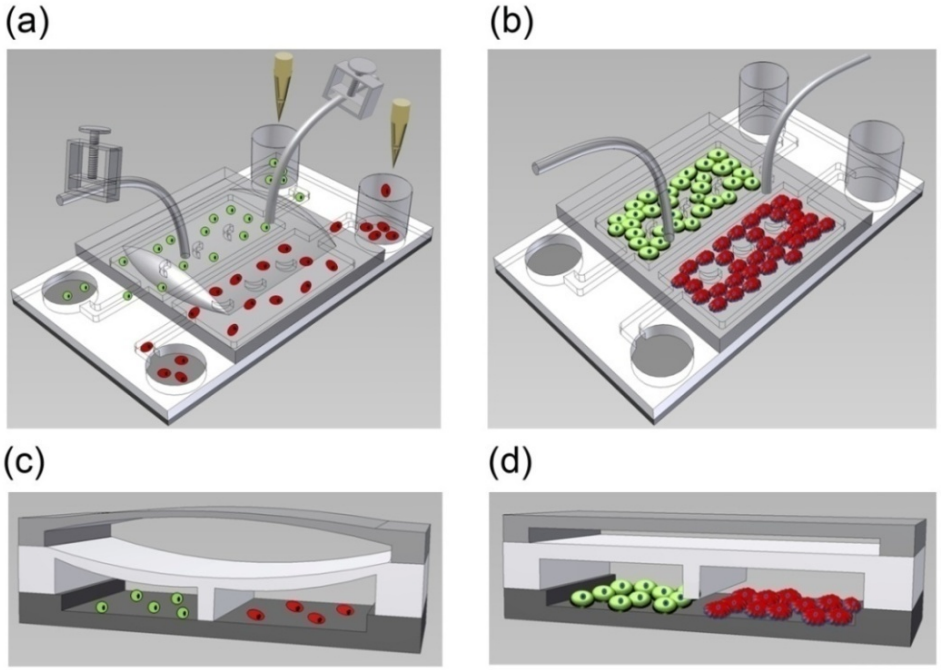

Figure 3.3: Schematics of the microfluidic platforms for tumor angiogenesis studies. 4T1 and ECs are loaded into each chamber and co-cultured for 24 hour (**a**), after which the valve barrier is released and cross-migration is assessed (**b**). The schematics of the cross-section views are shown in (**c**) and (**d**).

We applied the microfluidic cell co-culture platform to study the dynamic interaction between tumor cells and ECs *in vitro*. Since the device is on a glass slide, we can specifically and quantitatively modulate the microenvironment in each chamber and simultaneously image the kinetic changes of biological processes using real-time microscopy. In control experiments, while the barrier valve was closed by hydraulic pressure, murine 4T1 mammary tumor cells, which stably expressed a red fluorescent protein (RFP-4T1), were seeded in one chamber, and human dermal microvascular

endothelial cells stably labeled with green fluorescent protein (GFP-HDVEC) were seeded in the other chamber (Fig**. 3.3**(**a**)). Culture media (high glucose Dulbecco's Modified Eagle's Medium, (Mediatech, Inc., Herndon, VA) supplemented with 10% fetal bovine serum and 1% penicillin/streptomycin) were continuously flowed through the chamber to provide a physiological environment. When cell density reached ~75% confluence (after about 24 h), the valve barrier was lifted and the kinetics of cell migration was imaged for two additional days (Fig. **3.3**(**b**)). Under this condition, we found that cell migration was bidirectional: RFP-4T1 migrated toward GFP-HDVEC and GFP-HDVEC also migrated toward the tumor cells (Fig. **3.4**(**a**, **b**)), indicative of both tumor angiogenesis and intravasation/extravasation.

One major advantage of this device is to permit separate treatments of cells in each chamber, which we used to observe the effects of hypoxia on tumor angiogenesis. Hypoxia is a key regulator of angiogenesis. When tissue growth outpaces the growth of blood vessels the tissue becomes hypoxic. Hypoxia upregulates a variety of angiogenic genes that promote angiogenesis toward tissues and restore homeostasis (Carmeliet, et al., 1998; Ikeda, et al., 1995; Mandriota and Pepper, 1998; Pugh and Ratcliffe, 2003).

For experiments studying the effect of hypoxia, RFP-4T1 and GFP-HDVEC were seeded in separate chambers as previous described. After the cells reached ~75% confluence, 300 μM cobalt chloride ($CoCl_2$) (Sigma, St. Louis, MO) was added to the tumor cell chamber for 24 h to induce hypoxia. $CoCl_2$ mimics hypoxia by binding to the oxygen-dependent degradation domain (ODDD) in hypoxia-inducible factor-1α (HIF-1α) (Liu, et al., 1999; Yuan, et al., 2003). This binding prevents ubiquiti-

nation and degradation of HIF-1α and leads to the accumulation/stabilization of HIF in cells. Genes encoding proteins involved in numerous aspects of tumor cell proliferation, growth and metastasis are transcriptionally activated by HIF-1α (Bertout, et al., 2008). HIF-1α induces production of growth factors to promote endothelial cell proliferation and blood vessel formation. For example, VEGF, which is a key angiogenic factor secreted by cancer cells, are activated by HIF-1α (Harris, 2002).

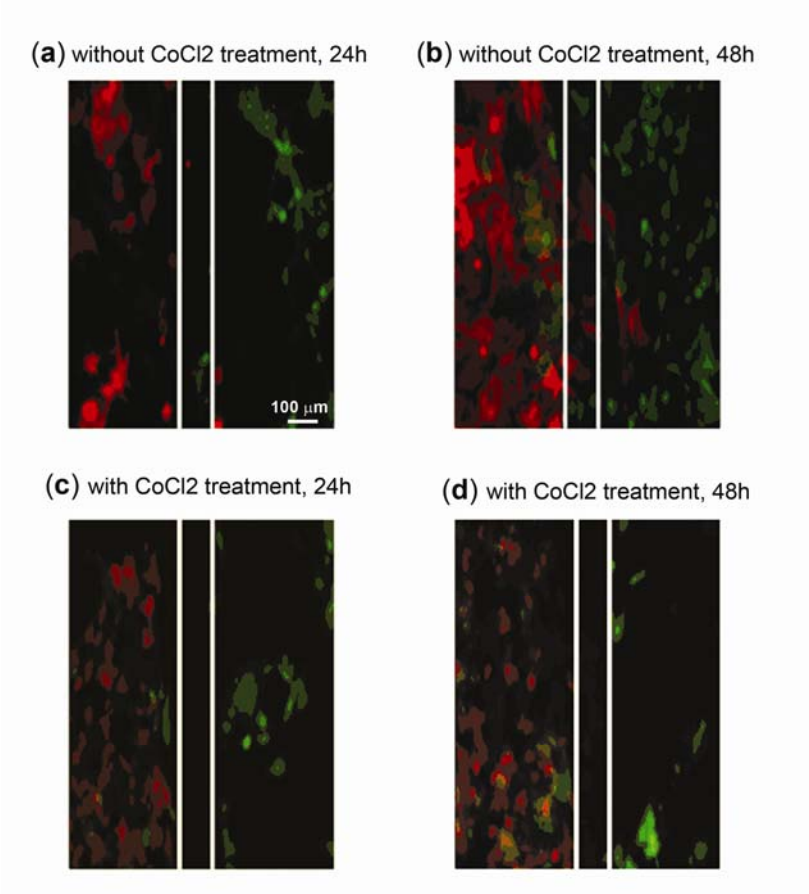

Figure 3.4: The interactions of tumor cells and ECs. To investigate the cross-migration under normoxic and hypoxic conditions, GFP-HDVEC cells were seeded in the right chamber and RFP-4T1 were seeded in the left chamber and cultured with (**c**,**d**) or without (**a**,**b**) $CoCl_2$ (300 μM). Images in panels (**a,b**) show bidirectional cell migration under the normoxic condition. Images in panels (**c,d**) show migration of endothelial cells only after hypoxic treatment of tumor cells.

After $CoCl_2$ treatment, fresh media flowed through the chambers to remove excess $CoCl_2$ from the system and then the two chambers were connected by releasing the valve barrier. We continuously examined the kinetics of cell-cell interactions for two additional days. Intriguingly, under this condition, it became a one-way traffic. Only migration of GFP-HDVEC toward RFP-4T1 was observed, but not the vice versa (Fig. **3.4**(**c**, **d**), which was quite different from the observations we made under normoxic conditions. These experiments suggested that under normoxic condition, both tumor cells and ECs recruit each other. However, the hypoxic treatment of tumor cells suppresses their migration ability and prompts release of angiogenic growth factors to attract ECs and the process is angiogenesis only.

3.4 Cross-migration of 4T1 tumor cells and ECs

Crosstalks between tumor epithelium and host vasculature endothelium promotes tumor progression in several cancer types. However, the molecular mechanisms that couple receptors to migration and angiogenesis remain unclear, particularly cooperative signaling with and regulation of other angiogenic factors. Ephrin and Eph receptors are one of key regulators of physiological and pathological processes in development and disease (Cheng, et al., 2002). EphA2 receptor tyrosine kinase is overexpressed in tumor and associated tumor vasculature for several types of cancers, including breast cancer, where they regulate proliferation, motility, and angiogenesis. Several studies reported that EphA2 and its primary ligand, ephrin-A1, regulate angiogenesis. For example, it has been found that ephrin-A1 stimulates ECs migration and assembly (Butler, et al., 2010).

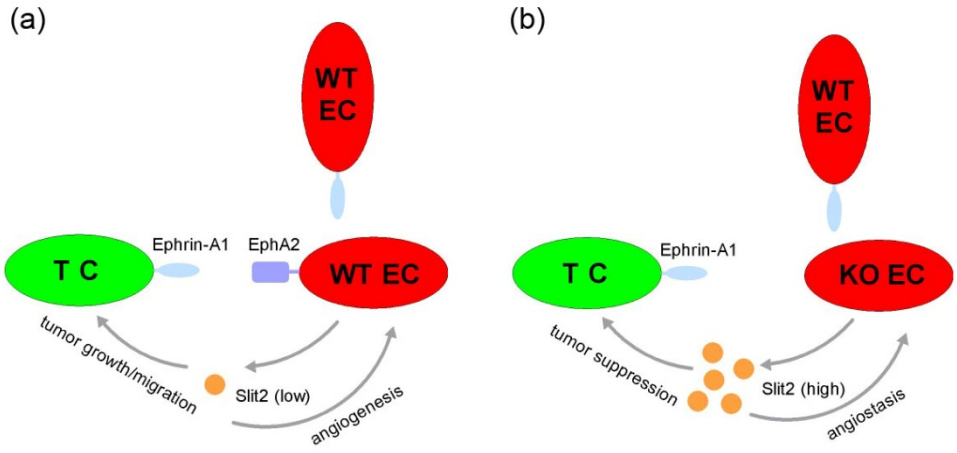

Figure 3.5: Hypothesis of endothelial EphA2 regulates Slit2 to modulate tumor angiogenesis. (**a**) In WT ECs, their EphA2 can be activated by ephrin-A1 ligand on adjacent tumor cells. Active EphA2 suppresses Slit2 expression. Reduced Slit2 levels permit angiogenesis and tumor growth. (**b**) In KO ECs, failure to respond to ephrin-A1 increases slit2 expression. Elevated Slit2 inhibits angiogenic remodeling and suppressing tumor growth.

To determine whether EphA2 regulates angiocrine function, a traditional method is to treat the tumor cells with conditioned medium (CM) derived from wild-type (WT) ECs or EphA2-deficient (KO) ECs. Tumor cells were shown to form large and more regular spheroid colonies in WT EC CM, while those growing in KO EC CM produced small and more uniform colonies (Debnath, et al., 2003). However, the communication between ECs and tumor cells is bi-directional. It was hypothesized that EphA2 downregulates Slit2 in endothelium (Brantley-Sieders, et al., 2011). WT ECs receive the ephrin-A1 ligand expressed on tumor cells through their EphA2 receptors (Fig. **3.5**(**a**)). Active EphA2 suppresses Slit2 expression, which promote angiogenesis as well as tumor cell growth and motility. But the KO ECs fail to respond to ephrin-A1 and the slit2 expression is elevated, which inhibits both EC and tumor cell

migration (Fig. **3.5**(**b**)). To test this hypothesis, we co-cultured 4T1 mammary tumor cell with WT or KO microvascular ECs side by side in the microfluidic platform and quantified the cross-migration of these cell types simultaneously.

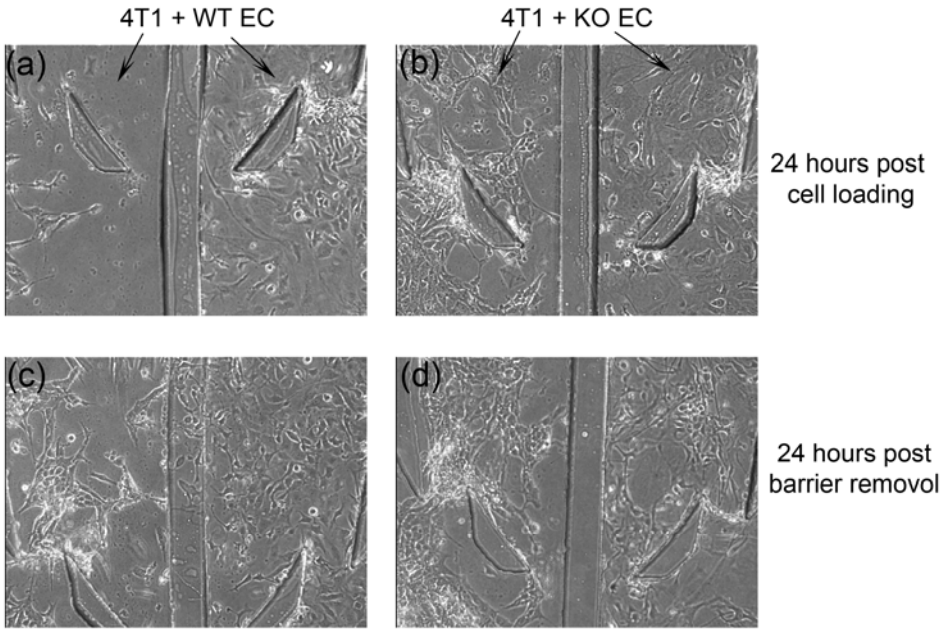

Figure 3.6: Phase contrast images of 4T1 and ECs cross-migration. 4T1 mammary tumor cell with WT (**a**) and KO ECs (**b**) were loaded into the co-culture chambers. After another 24 h the valve barrier was released. The cross-migration of tumor cells and ECs was examined, which showed very different patterns (**c**, **d**). The width of the barrier is 100 μm.

Primary microvascular ECs were isolated from wild-type or EphA2-deficient animals. 4T1 mouse mammary adenocarcinoma cells were purchased from American Type Culture Collection (ATCC, Manassas, VA). Cell chambers were first coated with growth factor reduced Matrigel^{TM} (BD Biosciences, San Jose, CA) and equilibrated by growth media. After the PDMS barrier was pushed down by pressurizing the control chamber with DI water, GFP labeled 4T1 tumor cells were loaded into one

chamber and CellTracker Orangel labeled ECs were loaded into the other chamber. After 24 hours, we replaced growth medium with starvation medium (Optimen/2% FCS) (Fig. **3.6**). Then the barrier was released to permit cross-migration. After another 24 hours, we counted tumor cells and ECs that crossed the central valve barrier in 4 independent 20× field views per devices simultaneously on the basis of cell morphology and differential fluorescent labeling as shown in Fig. **3.7**.

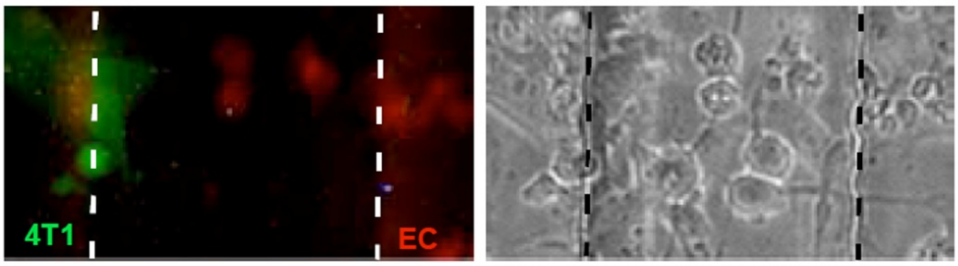

Figure 3.7: Cross migration of 4T1 and ECs. The width of the barrier is 100 μm.

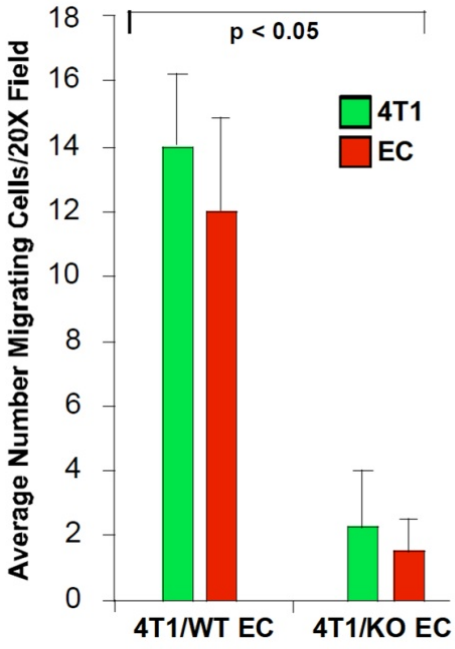

Figure 3.8: Migration results assessed by 4 independent 20× field view per device.

The results showed that co-culture between 4T1 and WT ECs promoted cross-migration of both cell types. By contrast, we found that loss of EphA2 in endothelium inhibits cross-migration of tumor cells and ECs (Fig**. 3.8**). These data show that tumor cells stimulate ECs to produce angiogenic signals that modulate their growth and motility, and these signals are regulated in part by EphA2 receptor tyrosine kinase.

3.5 Summary

The valve-enabled microfluidic platform has been modified to satisfy the requirement for cell cross-migration studies in cancer biology. Instead of a barrier with the parallel microgrooves, a solid straight PDMS wall sits onto an etched coverslip to form the functional platform. The platform allows for separate control of the cell microenvironment, treatment of selected cell populations, and observation of cell-cell communication between two cell populations at a desired time point. Therefore, it can be used to quantify cross-migration of two cell types simultaneously.

We demonstrated the applications of the platform through co-culture of tumor and endothelial cells and examined their cross-migration under normoxic and hypoxic conditions, reaffirming the significance of the microenvironment in biological reactions. Results showed that under normixic condition, both angiogenesis and metastasis occurs while hypoxic treatment of tumor cells suppresses the migration capability of tumor cells and the process is angiogenesis only. In addition, we obtained different cross-migration patterns mediated by different receptors and ligands, which helps to dissect the important functions of ephrin and Eph ligand-receptor pairs in tumor angiogenesis and metastasis.

CHAPTER 4

MICROFLUIDIC CULTURE PLATFORMS WITH PERMEABLE AND SEMI-PERMEABLE BARRIERS

4.1 Introduction

Cell-cell interactions occur through either direct cell-cell physical contacts or extracellular soluble factors. For example, it was found that the clonogenic growth of human breast tumor cells were dramatically and consistently enhanced when they were co-cultured in direct contact with fibroblasts (Samoszuk, et al., 2005). It would be extremely desirable to design a cell culture platform that has the ability to differentiate between cell-cell interactions through direct physical contacts and soluble factors. The reported microfluidic platform, as discussed in Chapters 2 and 3, allows for cell-cell interactions through both direct physical cellular contacts and soluble factors. To extend the capabilities of the platform, a variation of the valve barrier has been designed and implemented. An agarose-coupled valve barrier (ACVB) was patterned which prevented a miscellany of cells but allowed for communications between two populations through soluble factors alone.

A molecule functions as a ligand by binding to a receptor embedded within the plasma membrane of the target cell. The binding initiates a sequence of responses in the receiving cell. Cells communicate with one another through a huge variety of extracellular soluble signaling molecules. Chemical inhibitors are normally used for determining ligand's definitive roles. However, a cocktail of inhibitors can deal with

multiple candidate molecules. Another method to investigate the signaling pathways is to inactivate the gene coding the interested ligand or receptors using modern DNA technology, known as gene knockout (Brantley-Sieders, et al., 2004; Wolfer, et al., 2002). However, gene knockout is a time-consuming and cost-prohibitive process and requires huge amounts of effort to conduct. Here we have developed a simpler approach to probe the extracellular signaling pathways by further engineering the permeable barrier between two cell chambers to be able to selectively block the transport of certain type of ligands.

To better mimic the *in vivo* microenvironment, it is desirable to culture cells and study the cellular interactions in a 3D context. The cell-matrix interaction in a 3D framework mediates physiological responses that are important for cell growth, differentiation, and survival (Bissell and Radisky, 2001; Jacks and Weinberg, 2002). For example, fibroblasts cultured within a 3D ECM showed different morphology and migration patterns from those cultured on 2D surfaces (Cukierman, et al., 2001). The current microfluidic platforms have the capability to accommodate both 2D and 3D cell cultures. In this chapter, we also explored the potential of cell culture in a 3D matrix by loading cells together with bio-gels into the microfluidic chambers.

4.2 Microfluidic Platforms with An Agarose Coupled Valve Barrier

4.2.1 Design principle

This new design of a barrier is intended to study cell-cell interactions through soluble factors alone (Fig. **4.1**(**a**)). The ACVB is fabricated using two PDMS barriers that form an agarose channel after being pushed down. The pre-gel solution of aga-

rose is then filled into this middle channel (Fig. **4.1**(**b**)). After polymerization, the PDMS valve barriers are released into the 'up' position and the agarose remains attached to the glass substrate and subsequently forms an agarose-coupled barrier. This barrier can block transport of cells (Fig. **4.1**(**c**)) but allows soluble signaling molecules to perfuse through. In this way, the platform with an ACVB permits cell-cell interactions solely through soluble factors. In addition, by loading cells together with biogels into the chambers, the microfluidic cell co-culture platform is adaptable for 3D cell co-cultures.

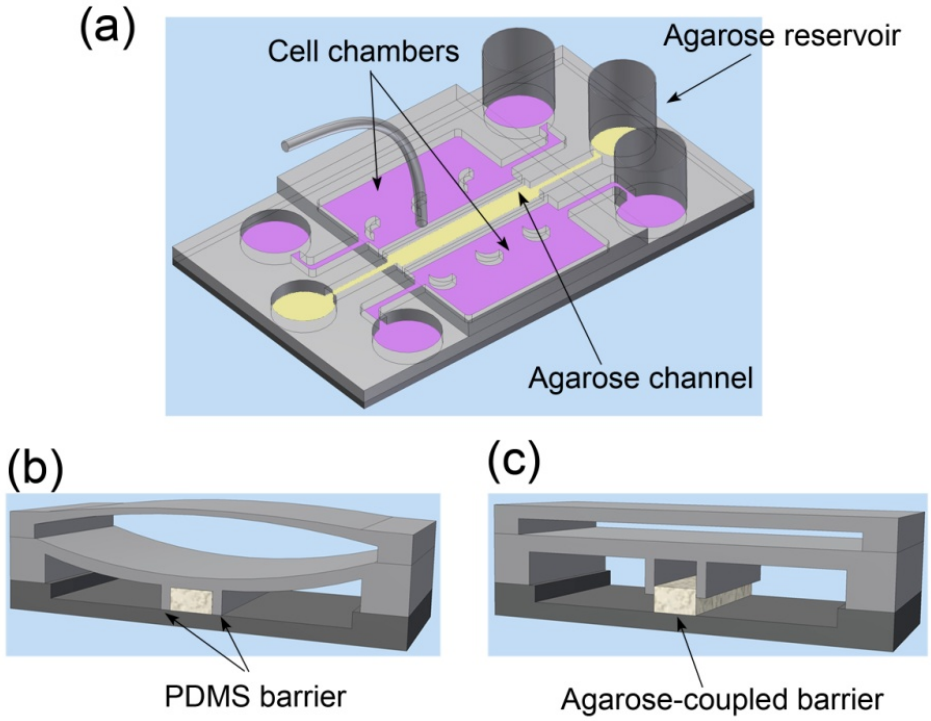

Figure 4.1: Schamtics of the formation of an ACVB in the microfluidic platform. (**a**) A schamatic of the microfluidic device. (**b**) After the two PDMS valve barriers are pushed into the 'down' position to form a channel, pre-gel (agarose) is loaded into the middle channel. (**c**) Once the PDMS valve barriers are released into the 'up' position to form an ACVB, soluble factor exchanges between the two chambers can occur.

4.2.2 Surface treatment and barrier formation

To reduce the bonding between the agarose and the PDMS so that the agarose would not move up with the PDMS, the PDMS barriers were pre-treated with ethylene glycol or Fluoronic 127 following the published protocols (Golden and Tien, 2007; Tang, et al., 2003). In addition, the glass slide was coated with aminopropyl triethoxysilane (APTES) to form aminosilane on the surface, which could enhance the agarose attachment to the glass coverslip to help the agarose to still stay on the substrate once the valve barriers were released. The details of these treatments are described as follows. After the PDMS was peeled off from the SU8 mold and the reservoirs were punched, it was adhered to a clean coverslip directly, forming a reversible bonding. Ethylene glycol or Fluronic 127 (Sigma-Aldrich, Atlanta, GA) was filled into the channel by capillary force to treat the channel inner surfaces at 37^{o}C. After 1 h, DI water was filled into the channel to wash off the excess ethylene glycol or Fluronic 127 (30 min at 37^{o}C). The PDMS was then peeled from the coverslip and dried overnight. For the glass substrates, the microscopic slides were first immersed in a 10% nitric acid solution at 80-90^{o}C with gentle shaking for 1 h. After rinsed with water, the slides were placed in a 10% solution of APTES (Sigma-Aldrich, Atlanta, GA) at a pH value of 3.4. The solution was heated to 70^{o}C with stirring for an additional 3 h. The silanized slides were then thoroughly rinsed with water and dried overnight.

After the platform was assembled and the two PDMS valve barriers were pushed into the 'down' position to form a channel (Fig. **4.1**(**b**)), agarose pre-gel solution was loaded into the middle channel with the entire platform placed on a hotplate at 60^{o}C. The agarose pre-gel solution was prepared by adding phosphate buffer to a

measured amount of agarose powder (Sigma-Aldrich, Atlanta, GA) to a concentration of 1 mg/ml. The mixture slurry was then heated in an oven to 90^{o}C till the agarose power was completely dissolved. The hot agarose pre-gel solution was then loaded into the middle channel, after which the platform was removed from the hotplate to cool down at room temperature allowing for gelation of the agarose.

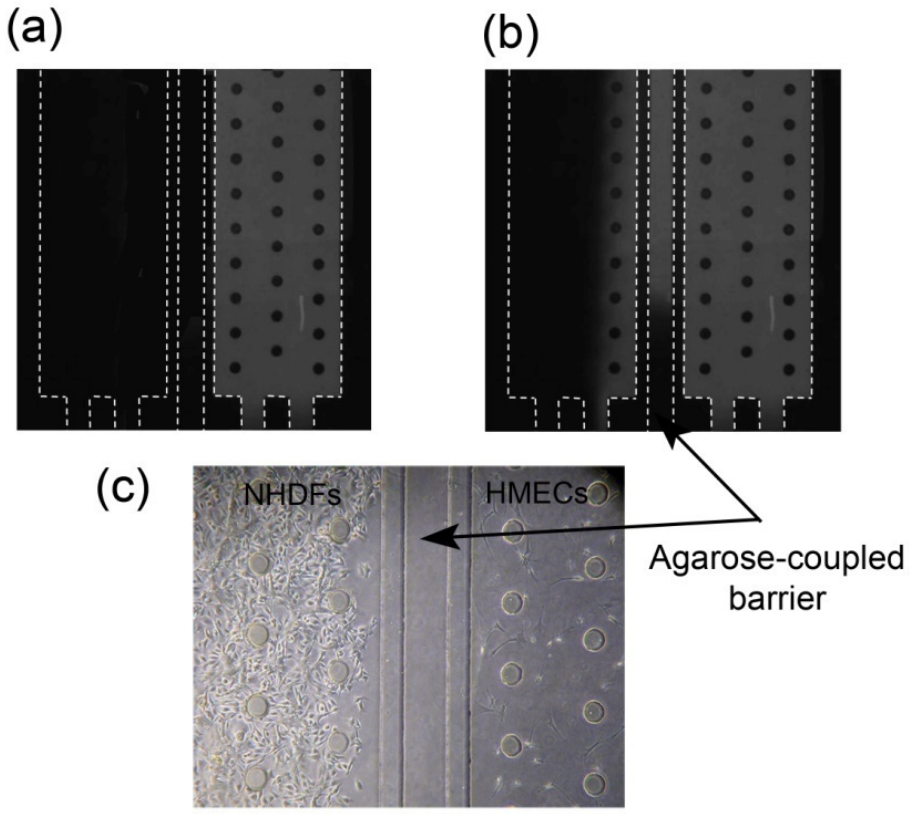

Figure 4.2: The cell co-culture platform with an ACVB. (**a**) FITC was added in one chamber with the PDMS valve barrier closed. (**b**) After releasing the valve barrier, fluorescent signals were observed in the opposite chamber, indicating that the dyes perfused through the nanoporous agarose. (**c**) HMECs in Matrigel^{TM} and NHDFs in type I collagen were loaded and cultured side by side. The two cell populations could communicate with each other only through soluble factors because the nanoporous agarose blocked the cells from migrating through the valve barrier.

The pore size of agarose varies from 50 nm to several hundred nanometers depending on the concentration (Narayanan, Xiong et al. 2006). Figure **4.2**(**a**, **b**) show fluorescence images of the microfluidic devices with an ACVB after one cell chamber was filled with Fluorescein isothiocyanate (FITC) (Thermo Fisher Scientific, Pierce, IL). After the gelation of the agarose while the PDMS barriers were in 'down' position, FITC was loaded into one cell culture chamber. A fluorescent image was taken as Fig. **4.2**(**a**). There was no fluorescence detected in the other cell chamber. After the PDMS valve barriers were released, fluorescent signal appeared in the opposite cell chamber (Fig. **4.2**(**b**)).

4.2.3 3D cell co-culture and discussions

We have demonstrated that the ACVB could block cells from migrating into the opposite chamber by loading the two chambers on each side of the valve barrier with human mammary epithelial cells (HMECs) in Matrigel^{TM} and normal human dermal fibroblasts (NHDFs) in type I collagen. Because the cell-gel mixtures were viscous, a vacuum-driven loading method was employed to load HMECs and NHDFs with their distinct 3D matrix as follows. The harvested HMECs and NHDFs were suspended in their respective growth media at a density of $1x10^6$ cells/ml. The suspended media and the microfluidic platform with the hydraulically activated valve were placed on ice prior to cell loading. The HMECs were prepared in Matrigel^{TM} (BD Biosciences, San Jose, CA) at the following volumes: 25 µl cells with 75 µl of Matrigel^{TM}. After mixing these two components to homogeneity, the 100 µl mixture was added to the loading well of HMECs, upon which vacuum was applied at the cor-

responding waste well to help the mixture to flow down to the cell culture chamber. For the NHDFs, 40 µl of type I collagen (BD Biosciences, San Jose, CA) and 60 µl of NHDF suspended medium was mixed homogeneously with the help of 0.5 µl of 1 M NaOH. The mixture was then added to the loading well of NHDFs and vacuum was applied in the same manner as for HMECs. The co-culture platform was then placed into a humidified incubator at 37°C for 30 min to polymerize the matrices, after which the loading reservoirs of the HMECs and NHDFs were filled up with their respective culture media.

The HMECs and NHDFs were first maintained for 7 days with the valve closed. On day 8 the valve was opened. The nanoporous ACVB allowed soluble factors to perfuse through but prevented cells from crossing the barrier and migrating into the opposite chamber (Fig. **4.2**(**c**)).

Due to the fact that convection is hindered in Matrigel^{TM} and collagen (McCarty and Johnson, 2007; Ramanujan, et al., 2002), wider loading channels were designed to provide sufficient culture medium to the cells. Instead of 150 µm wide loading channels for 2D cell culture, 400 µm wide channels were used here. It was shown that cells could be cultured in the microfluidic chambers for as long as 3 weeks. Another problem that was encountered in the 3D cell co-culture is that collagen fibers will contract during cell culture in response to the cell-matrix interactions. To overcome this issue, columns of posts were patterned in each chamber as anchors for the gel fibers to adhere, as indicated in Fig. **4.2**(**c**). Multiple experiments showed that these anchors could effectively prevent the collagen fibers from contracting during cell culture and interaction period.

4.3 Microfluidic Platforms with a Semi-permeable Barrier

4.3.1 Design principle

To this point, the cell co-culture platform can control cell-cell interactions through soluble factors alone using the ACVB. As discussed in the introduction section, to dissect the functions of individual molecules in biological studies, it is extremely desirable to be able to selectively filter out the exchange of certain molecules between the two cell populations, which can help to identify the specific functions of the interested molecules. Therefore, we further modified the co-culture platform to implement a semi-permeable barrier by imbedding "ligand traps", which selectively block the exchange of certain soluble signaling molecules (ligands).

Ligand traps are engineered protein-coated nano/micro-particles. The proteins have the ability to bind to certain ligand(s) selectively with high affinity. In the literature, the vascular endothelial growth factor (VEGF)-Trap, which was a soluble decoy receptor to prevent VEGF binding to its normal receptors, has been used as a VEGF targeted therapy (Holash, et al., 2002). Since the receptor proteins are small and can perfuse in the nanoporous gel, they are conjugated to nanoparticles in our studies. After mixing with ligand traps, the pre-gel solution is loaded into the middle channels, following a similar procedure as shown in Fig. **4.1**. As the size of the nanoparticles is much larger than the pore size of the gel, the conjugated receptors cannot leak out of the barrier after formation. Smaller particles are preferable because for the same volume they will provide larger surfaces to conjugate receptors so that the available binding sites are increased to effectively block the transmission of targeted ligands. In

addition, smaller particles make it easier to achieve a more homogenous distribution of these ligand traps.

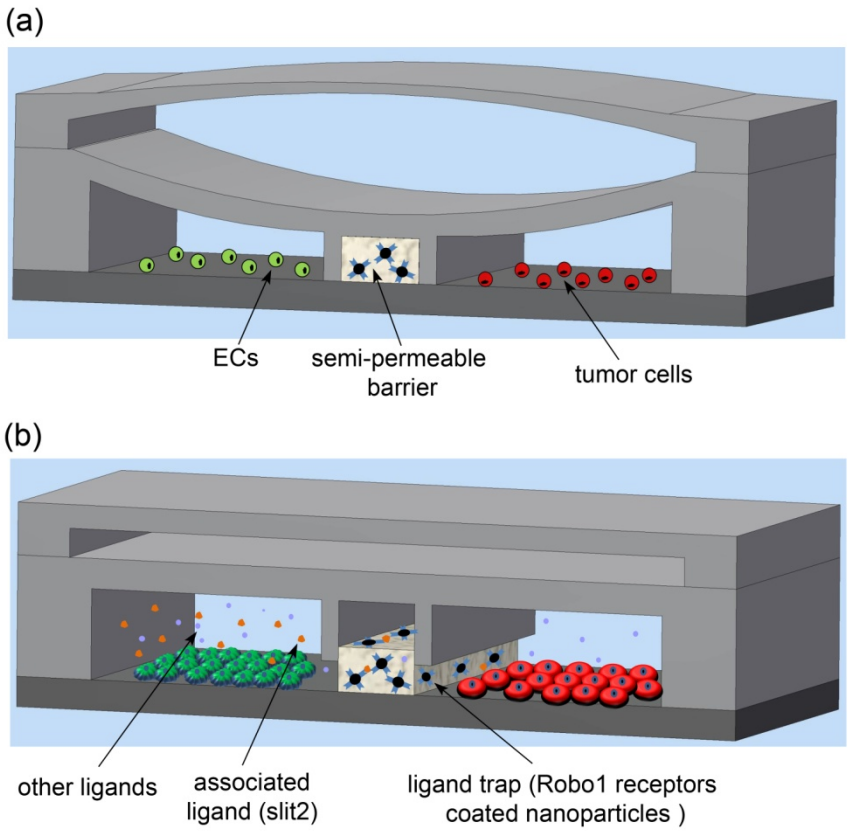

Figure 4.3: Schematics of the semi-permeable barrier, which is used to block the transport of certain ligand from one chamber to the other. (**a**) ECs and tumor cells are loaded into their respective chamber with the valve closed. (**b**) Exchange of soluble factors are allowed excluding the specific molecule. For example, the ligands (slit2) bind to the immobile receptors (such as Robo1) inside the barrier and hence are blocked from reaching the other chamber.

Once the associated ligands are transported through the barrier, they will be 'trapped' by binding to the receptors with high affinity. If all ligands bind to their receptors before moving out of the barrier, the targeted soluble ligands are fully blocked

from the soluble factor exchange between the two chambers. In the design for tumor cell and EC cross-migration studies, for example, Robo1 receptor coated nanoparticles are expected to be able to block the perfusion of soluble Slit2 secreted by ECs. As shown in Fig. **4.3**, tumor cells in the right chamber can sense all signaling molecules secreted by the ECs in the left chamber except Slit2, which are all expected to be trapped by the Robo1 receptors inside the barrier when they try to cross the barrier.

4.3.2 Demonstration of ligand traps by two fluorescent proteins

In the last chapter, the microfluidic platforms use an etched coverslip as the base. The two chambers communicate with each other through the gap between the etched surface and the bottom of the PDMS barrier, whose height is defined primarily by the etching depth. In fabricating the co-culture platforms with semi-permeable valve barriers, however, we used a two-layer fabrication technique similar to that shown in Fig. **2**.**2**; but the fabricated platform is similar to the one in Chapter 3, i.e., with a continuous gap for cell-cell interactions. In the fabrication process, instead of an array of lines, a long rectangular SU-8 layer was first patterned on the silicon wafer as shown in Fig. **4.4**. A second layer, defining two PDMS valve barriers and two larger cell culture chambers and a narrow middle gel channel, was then created. The schematic of the mold to construct the first PDMS layer is shown in Fig. **4.4**(**b**). The second PDMS layer is produced in the same way as those in previous chapters. This new fabrication process avoids the glass etching process involving hazardous hydrofluoric acid (HF). In the platform, the height of the gap is defined by the thickness of the first rectangular SU-8 block, which is also easy to be controlled by the selection of

the type of SU-8 and the spinning speed. In this dissertation, we fabricate microfluidic platforms having a 20 µm gap between the two chambers of 100 µm in height.

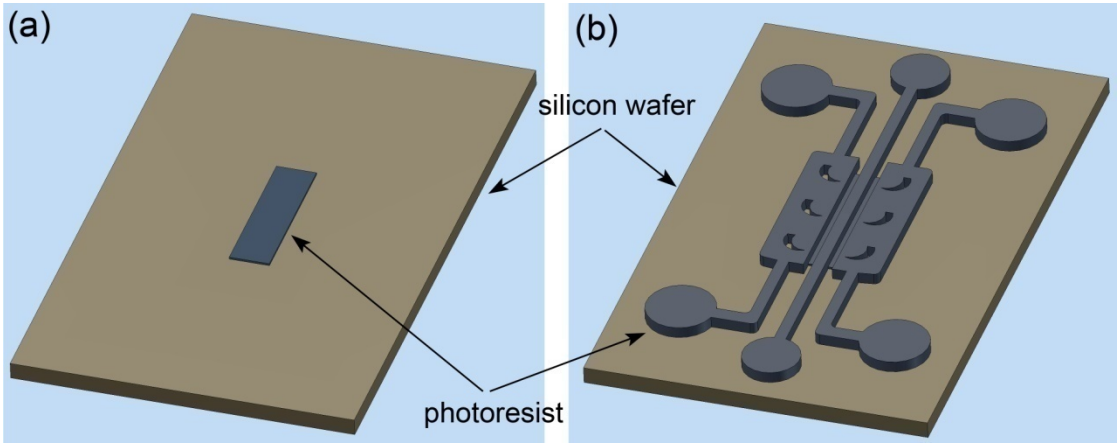

Figure 4.4: Schematics of the process to fabricate the mold for the first PDMS layer. (**a**) A rectangular SU-8 layer is first patterned on a silicon wafer, whose thickness defines the gap height between the two chambers. (**b**) Another SU-8 layer is aligned and patterned onto the first SU-8 layer to define the channels and chambers.

As mentioned in section **4.2.2**, the coverslip was treated by ethylene glycol to enhance the attachment of the gel and the PDMS surface was coated with APTES to facilitate the releasing of the PDMS barrier. Biotin coated polystyrene particles (0.7 – 0.9 µm in diameter; Spherotech, Lake Forest, IL) were chosen as the ligand trap. Instead of agarose, collagen was used as the scaffold for the ligand traps because implement of agarose involves high temperature which will damage the receptor proteins. The gel was prepared by adding 10 µl 10× PBS and 0.38 µl NaOH (Sigma-Aldrich, Atlanta, GA) into 73 µl polystyrene particles solution. Vortex mixer was used to disperse the particles. Subsequently, 16.6 µl collagen (BD Biosciences, San Jose, CA) was added and mixed homogeneously to get a final collagen concentration of 1.5

mg/ml and a particle concentration of 2.59×10^{10} particle/ml. After the valve was activated by injecting DI water in the control chamber, the platform was placed on ice. Subsequently, the pre-gel mixture was filled into the mid-channel in a manner similar to that shown in Fig. **4.1**. After loading, the whole platform was placed into a humidified incubator at 37°C for 30 min to polymerize the matrix.

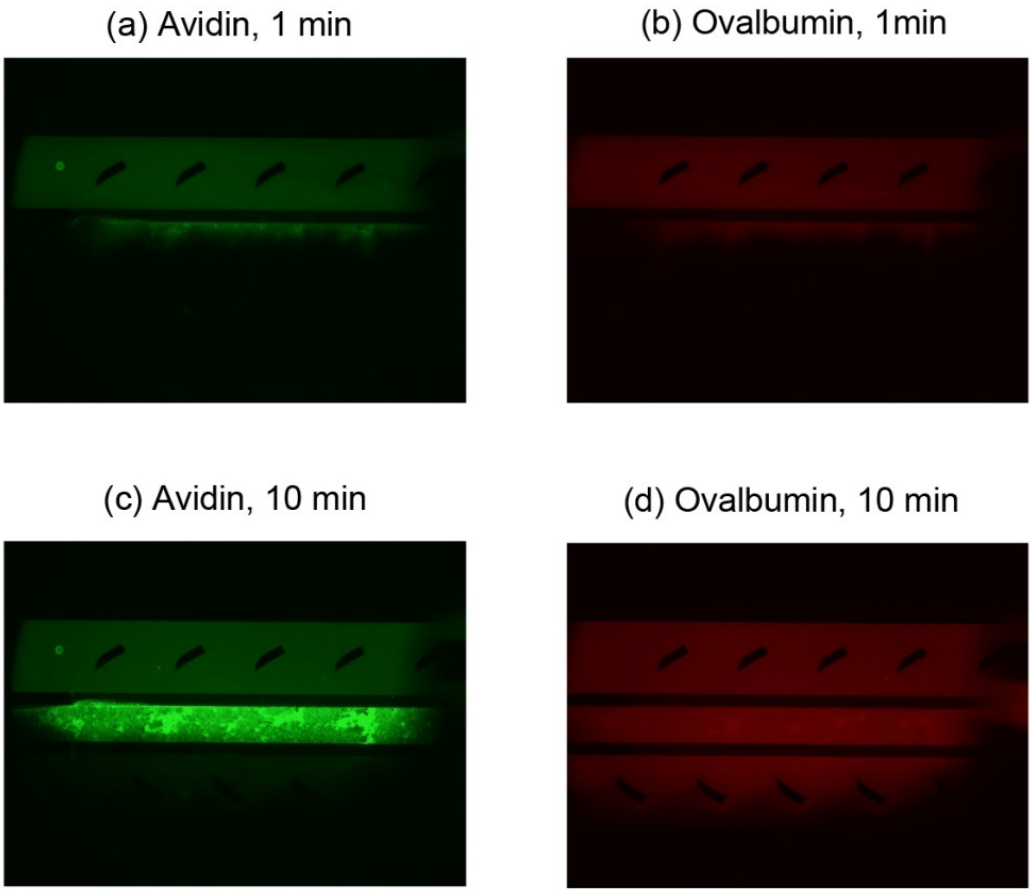

Figure 4.5: Demonstration of the semi-permeable barrier with two fluorescent proteins. Avidin-Alexa Fluor 488 (green) is trapped by the biotin coated nanoparticles inside the barrier and therefore cannot transport from one chamber to the other. However, ovalbumin-Alexa Fluor 647 (red) can pass through the barrier and perfuse into the other chamber. (The width of the barrier is 200 μm)

After gelation, the semi-permeable valve barrier was formed by releasing the DI water from the control chamber. Two fluorescent proteins, avidin-Alexa Fluor 488 and ovalbumin-Alexa Fluor 647 (both from Invitrogen, Carlsbad, CA), were added into one chamber. Avidin was known to bind to biotin with a high degree of affinity. The dissociation constant of biotin and avidin was measured as 10^{-15} M (Green, 1963). Therefore, we expected avidin-Alexa Fluor 488 to be trapped by the immobile biotin coated particles inside the barrier, while the ovalbumin-Alexa Fluor 647 could pass the barrier and perfuse into the other chamber.

The experimental result is shown in Fig. **4.5**, which clearly indicates that the avidin (green) binds to the immobile biotin inside the barrier and therefore is trapped by the biotin coated polystyrene particles. But the ovalbumin (red) can pass through the barrier and perfuse into the opposite chamber. As a result, avidin was effectively blocked from the molecular exchange between the two chambers.

In the fluorescent imaging based experiment, however, a high concentration for each fluorescent protein had to be used to obtain sufficient fluorescent signals for demonstration. The concentration added to the chamber was 0.48 μM/ml for avidin and 1.47 μM/ml for ovalbumin. According to the collagen matrix recipe described above, the ligand traps' binding ability to avidin is calculated as 1.69 μM per ml gel.

The experiment shows that the gel quickly becomes saturated with avidin, especially if there exists a transverse flow, which seems a problem. In real biological systems, however, the amount of ligands secreted by cells is orders of magnitude lower in concentration than the fluorescent proteins used here for demonstration. For example, homogeneous amounts of VEGF production by myoblast clones have been

measured ranging from 5.5 ng/10^6 cells/day to 191.2 ng/10^6 cells/day (Ozawa, et al., 2004). Suppose there are 10,000 myoblast clones in one chamber, which will secrete 2.4 – 83.3 × 10^{-6} nM VEGF in 10 days. This is a very tiny fraction, about 0.0023 – 0.082%, of the total binding ability of the ligand traps in the barrier (Suppose the gel's binding ability to VEGF is 1.69 μM/ml and the total volume of the gel in the barrier is 0.06 μl). Therefore, we expect that saturation would be very rare in real bioassays. To guide the design of the semi-permeable barrier, an analytical model of the barrier's performance has been developed and is presented in the next section.

4.3.3 An analytical model of the barrier's performance

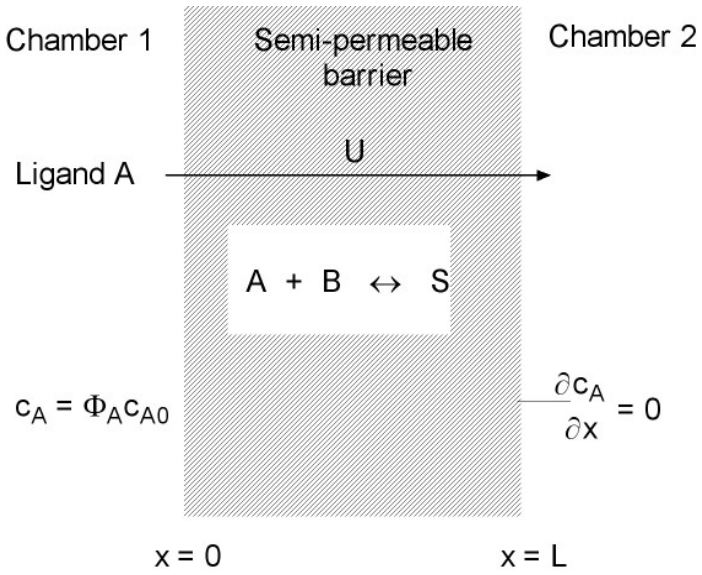

Figure 4.6: Schematic of transport of ligand (A) through a barrier, where it binds to its immobile receptor (B) and forms the ligand-receptor complex (S).

Here we develop a simple model for the concentration of the ligand in the semi-permeable barrier to obtain design rules for microfluidic platforms. Assume that

the ligand (A) in chamber 1 is able to enter the barrier with thickness (L) due to flow (U) and diffusion, where it binds to its receptor (B) and form the ligand-receptor complex (S) (Fig. **4.6**). For a successful semi-permeable barrier, all ligands from chamber 1 are expected to bind to their immobile receptors before reaching chamber 2. In the model, we first assume the concentration of receptors (B) is much larger than the concentration of ligands (A), which is reasonable since the ligands secreted by cells are usually of a very low concentration. Therefore, the binding becomes a pseudo first order reaction whose rate (R_{vs}) can be written as,

$$R_{vs} = k_{on}C_{B0}C_A - k_{off}C_S, \tag{4.1}$$

where C_A, C_{B0} and C_S denote the concentration of the ligand, receptor and ligand-receptor complex, respectively; k_{on} and k_{off} are the association rate constant and dissociation rate constant, respectively. We also assume that the ligand binds to its receptors with a high affinity. Thus the dissociation constant (k_{off}/k_{on}) is a small value. For example, the dissociation constant of biotin and avidin was measured as approximately 10^{-15} M (Green, 1963). Thus the second term on the right hand side of Eq. (4.1) can be dropped off. If we consider a transient case, the governing equation for the ligand's concentration in the barrier becomes,

$$\frac{\partial C_A}{\partial t} = D\frac{\partial^2 C_A}{\partial x^2} - U\frac{\partial C_A}{\partial x} - k_{on}C_{B0}C_A;$$

$$C_A(t,0) = \Phi_A C_{A0}, \quad \frac{\partial C_A(t,L)}{\partial x} = 0 \text{ and } C_A(0,x) = 0. \tag{4.2}$$

Here D is the diffusion coefficient of the ligand in the gel; Φ_A is the partition coefficient which describes how the a macromolecular solute will be influenced by its size,

charge, and by the composition and physical arrangement of the gel (Kosto and Deen, 2005).

Using L, L/U and C_{A0} as the characteristic length, time and concentration scales, respectively, Eq. (4.2) can be non-dimensionalized as,

$$Pe\frac{\partial\theta}{\partial\tau} = \frac{\partial^2\theta}{\partial X^2} - Pe\frac{\partial\theta}{\partial X} - Da\,\theta;$$

$$\theta(\tau,0) = \Phi_A, \quad \frac{\partial\theta(\tau,1)}{\partial X} = 0 \text{ and } \theta(0,X) = 0. \tag{4.3}$$

Here θ, X and τ are the dimensionless concentration, length and time, respectively. In Eq. (4.3), Pe is the Péclet number defined as, Pe = UL/D, which is the ratio of the mass transported by convection to the mass transported by diffusion; the Damköhler number, $\mathrm{Da} = k_{on}C_{B0}L^2/D$, is the ratio of the reaction rate to the diffusive rate. Using finite Fourier transform method (Deen, 1998), the analytical solution of Eq. (4.3) was obtained as

$$\theta(X,\tau) = \sum_{n=1}^{\infty}\frac{\Phi_A a_n \beta_n}{Pe b_n}\left[1 - e^{-b_n\tau}\right]e^{\frac{Pe}{2}X}sin(\beta_n X),$$

where β_n is the root of the equation " $\beta_n \cot\beta_n = -\frac{Pe}{2}$ ", $a_n = 2\frac{\beta_n^2 + Pe^2/4}{\beta_n^2 + \frac{Pe^2}{4} + \frac{Pe}{2}}$, and $b_n = 2\frac{\beta_n^2 + \frac{Pe^2}{4} + Pe\,Da}{Pe}$.

To illustrate the characteristics of the concentration distribution in the gel, we took the parameters as the following. The width of the barrier (L) is 100 μm; the concentration of receptors (C_{B0}) is 10^{-6} M, the diffusion coefficient (D) is 10^{-3} $mm^2\,s^{-1}$, and the reaction rate (k_{on}) is 10^7 $M^{-1}s^{-1}$ (Note that the biotin-avidin reaction rate was measured as 6.5×10^7 $M^{-1}s^{-1}$ (Green, 1963)). In this case, the Damköhler number Da = 100. For a small velocity (Pe = 1, which corresponds that U = 10 μm/s), all ligands

can be trapped in the barrier as shown in Fig. **4.7**(**a**). For a higher velocity (Pe = 10, which corresponds that U = 100 μm/s), the ligands would be on the edge to penetrate the barrier as shown in Fig. **4.7**(**b**). It should be mentioned here that the boundary condition in Eq. (4.2) at $x = L$ is only valid before the ligands penetrate the barrier in situations such as for a short time period or a small Péclet number.

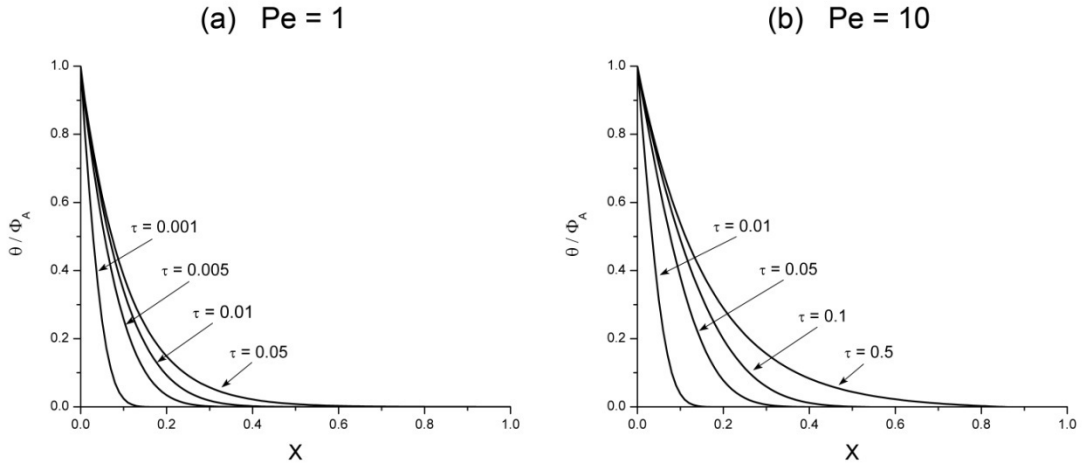

Figure 4.7: Ligand's concentration in the barrier as Da = 100. Under the current assumptions, the concentration profiles would not change as τ further increases in both figures.

A larger value of Da corresponds to a faster reaction, while a larger value of Pe represents faster trans-barrier flow. To be fully blocked from the exchange between the two chambers, the target ligands shall bind to their receptors before moving out of the barrier by the flow. It is informative to examine the relationship between Pe and Da to guide the selection of ligand traps and the design of the barrier. Therefore, we consider the long time behavior of the concentration profiles in the barrier. Neglecting the time derivative in Eq. (4.3), the governing equation and boundary conditions read,

$$\frac{d^2\theta}{dX^2} - Pe\frac{d\theta}{dX} - \mathrm{Da}\,\theta = 0;\ \theta(0) = \Phi_\mathrm{A}, \frac{\partial\theta(1)}{\partial X} = 0. \tag{4.4}$$

The analytical solution of Eq. (4.4) is

$$\theta(\mathrm{X}) = \Phi_\mathrm{A}\left[\cosh(\gamma \mathrm{X}) - \frac{\gamma\tanh(\gamma)+\frac{\mathrm{Pe}}{2}}{\gamma+\frac{\mathrm{Pe}}{2}\tanh(\gamma)}\sinh(\gamma \mathrm{X})\right] e^{\frac{Pe}{2}X}, \tag{4.5}$$

where $\gamma = \sqrt{\frac{\mathrm{Pe}^2}{4} + \mathrm{Da}}$. For a specific ligand-receptor reaction, it is important to find out the maximum velocity at which the ligand cannot penetrate the barrier under a given reaction rate. Suppose 'leakage' is defined as the concentration of ligand at the right boundary ($X = 1$) exceeding a certain value, $\alpha\Phi_\mathrm{A}$. By analogy with sieving coefficient in modeling ultrafiltration (Deen, 1998), the leakage coefficient, defined as $\alpha = C_{x=L}/C_{x=0}$, measures the overall effectiveness of the blocking for the interested ligand. That $\alpha = 0$ represents that all ligand entering the barrier are trapped (no leakage), while ligands completely transport through the barrier when $\alpha = 1$.

To look for the situations that $\theta(1) = \alpha\Phi_\mathrm{A}$, we first consider the case where there is no flow (U = 0), i.e., Pe = 0. The concentration at X = 1 then becomes,

$$\cosh\sqrt{\mathrm{Da}} = \frac{1}{\alpha}. \tag{4.6}$$

From Eq. (4.6), if we set $\alpha = 0.01$ then $\mathrm{Da} \approx 28.07$, which means that the Damköhler number cannot be smaller than 28.07 if we want the concentration of ligand is smaller than 1% of $\Phi_\mathrm{A}C_{\mathrm{A}0}$ on the right edge of the barrier.

If there exists a flow, where Pe > 0, Da must be larger than the value in the case without flow as presented in Eq. (4.6). At such a situation, the coefficient in side Eq. (4.5) becomes,

$$\frac{\gamma\tanh(\gamma)+\frac{\mathrm{Pe}}{2}}{\gamma+\frac{\mathrm{Pe}}{2}\tanh(\gamma)} \approx 1.$$

Then from Eq. (4.5), the following relationship is obtained,

$$\mathrm{Pe} = \log\left(\frac{1}{\alpha}\right)\mathrm{Da} + \log(\alpha). \tag{4.7}$$

The result is plotted in Fig. **4.8** for $\alpha = 0.01$ according to Eq. (4.7). If a pair of Da and Pe numbers falls below this line, all ligands will be trapped in the barrier. From the above analysis, we draw a conclusion that a big Da number is required to sustain a large transverse flow, which can be achieved by choosing the receptor with a high reaction rate, raising the receptor's concentration or increasing the barrier thickness from the definition of the Damköhler number.

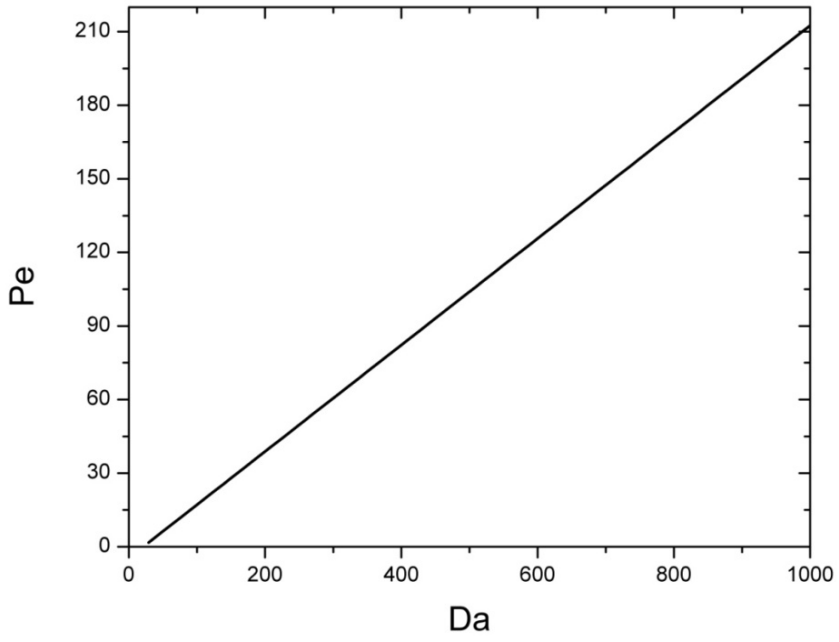

Figure 4.8: Relationship between the Damköhler number and the Péclet number. If a point (Da, Pe) is below this line, the concentration of the ligand out of the barrier will be smaller than 1% of the concentration on the other side of the barrier.

If the ligands and their receptors are already chosen, the design of the barrier can be shown in the following example. We try to find the minimal width of the barrier to block the transport of the ligand for a certain trans-barrier flow. From above analysis, to be a successful barrier, the following inequality shall be satisfied,

$$\mathrm{Pe} \leq \log\left(\frac{1}{\alpha}\right)\mathrm{Da} + \log(\alpha) \tag{4.8}$$

This equation can be transformed to another form

$$\frac{k_{on}C_{B0}}{\log(\alpha)}L^2 + \mathrm{UL} - \mathrm{D}\log(\alpha) \leq 0 \tag{4.9}$$

A meaningful solution of Eq. (4.9) is

$$L \geq \frac{U+\sqrt{U^2+4k_{\mathrm{on}}C_{\mathrm{B0}}D}}{2k_{\mathrm{on}}c_{\mathrm{B0}}}\log\left(\frac{1}{\alpha}\right) \tag{4.10}$$

Notice that $0 \leq \alpha \leq 1$. For example, we can perform a calculation with the following parameters: the concentration of receptors (C_{B0}) as 10^{-6} M; the diffusion coefficient (D) as 10^{-3} mm^2 s^{-1}, and the reaction rate (k_{on}) as 10^7 M^{-1}s^{-1}. Under these conditions, for $\alpha = 0.01$, Eq. (4.10) yields a width of the barrier as 74.5 μm to sustain the striking of a trans-barrier flow of 100 μm/s.

4.4 Summary

In this chapter, we present two variations of the valve-enabled microfluidic platform with different functions inspired by biological research needs, which are expected to significantly enhance the capability of the device, and hence extend its applications to a wider variety of biological studies.

The first variation is a nanoporous gel-coupled valve barrier, which could prevent cells from migrating through the barrier but allow soluble factors to perfuse

through. Therefore, two cell populations co-cultured side by side in this microfluidic platform communicate with each other through soluble signaling molecules alone. Together with the previously presented version, the valve enabled microfluidic platforms allow us to distinguish cell signaling pathways through either direct contact or soluble factors alone.

One more variation is the gel-coupled valve barrier with ligand traps embedded inside the barrier. In this version, the ligand traps could selectively block the transport of a specific kind of molecule from one chamber to the other. This provides an innovative new technique for dissecting extracellular signaling pathways. A mathematical model has been developed to correlate the relationship between the Damköhler number and the Péclet number to guide the design of a successful semi-permeable valve barrier.

We have also successfully implemented 3D side-by-side cell co-culture in the platform. Both HMECs in Matrigel^{TM} and NHDFs in collagen grow healthily up to 3 weeks. The ability to culture cells in a 3D context would help to more closely mimic *in vivo* cell behavior, which would be very attractive to the biological research community.

CHAPTER 5

MICROFLUIDIC CULTURE PLATFORMS WITH CONCENTRATION GRADIENTS

5.1 Introduction

Cell migration plays a critical role in many biological and pathological processes including embryogenesis, the immune response, wound healing, tissue repair, and tumor metastasis (Lauffenburger and Horwitz, 1996). Chemotaxis is a phenomenon in which a cell migrates directionally in response to a certain chemical concentration gradient. The cell senses the relatively shallow external gradient of a chemotactic agent and responds with highly oriented polarity and motility (Weiner, 2002). Thus, an understanding of the molecular basis of chemotaxis could lead to new therapeutic opportunities for many pathological processes underlying cell migration.

Not surprisingly, there is considerable interests in developing assays to generate a chemotactic gradient. Traditional methods to create gradients of chemotactic agents include the pipette-based assay (Gerisch and Keller, 1981), the under-agarose assay (Kohidai, 1995; Nelson, et al., 1975), the Boyden/transwell assay (Boyden, 1962), and the Dunn assay (Zicha, et al., 1991; Zicha, et al., 1997). In recent years, various microfluidic chemotactic platforms have been developed which were typically miniaturized variations of these traditional assays. For example, with the Dunn chamber, the linear chemotactic gradient was originally created in a glass bridge between two concentric wells, and the microfluidic version included a source/sink construct to generate the chemotactic gradient in a microfabricated device (Abhyankar, et al.,

2006; Cheng, et al., 2007; Diao, et al., 2006; Shamloo, et al., 2008). To slow down the decay of the gradient, microcapillaries (Shamloo, et al., 2008), hydrogels (Cheng, et al., 2007), and membranes (Abhyankar, et al., 2006; Diao, et al., 2006) were used to serve as high fluidic resistances to minimize the convective transport and maintain a diffusion-dominating environment.

However, in real device operation, various factors can prevent the formation of precise molecular gradients that are stable in space and time for biological studies. In the Dunn chamber, for example, the agents will deplete in the source and accumulate in the sink, which will lead a drift of the concentration gradient over time. To prevent the depletion and accumulation, two continuous fluid streams have been introduced to replace the two still liquid reservoirs in microfluidic platforms (Irimia, et al., 2007; Saadi, et al., 2007). Another microfluidic concentration gradient generator was a pyramidal microfluidic device presented by Whitesides and co-workers (Dertinger, et al., 2001; Dertinger, et al., 2002; Jeon, et al., 2000; Jeon, et al., 2002). In this scheme, two laminar streams carrying different concentrations of chemotactic agents created a concentration gradient perpendicular to the flow direction after they were repeatedly split, mixed, and recombined in the microfluidic network extending in a pyramidal way. Even though there are several drawbacks such as that cells experience shear stress and the concentration gradient depends on both the position along the flow direction and the flow velocity (Walker, et al., 2005), this type of devices can build up a concentration gradient very quickly and has been widely used for chemotaxis studies (Chung, et al., 2005; Jeon, et al., 2002; Lin, et al., 2004; Saadi, et al., 2007).

One requirement for both of the above-mentioned schemes is that external syringe pumps are used to maintain equal flow rates/pressures of the two loading streams, which is essential to the generation and maintenance of the stable concentration gradient. This requirement limits the widespread use of these devices for long-term cell culture by biologists. Even though active pumping methods such as syringe pumps or electroosmotic pumps can provide more accurate and adjustable volumetric flow rates, the utilization of these pumps requires external equipment which is generally large in size and complex to operate. Moreover, considering the series of activities in cell culture and biological investigations such as cell seeding, culture maintenance, treatment, and observation, the external instruments and their connections complicate the device's experimental usages and increase the chance of introducing contamination.

In view of this, it is desirable to develop a simple microfluidic platform that can generate a stable concentration gradient without the need for complex external instruments. As mentioned in the previous chapters, the passive pumping method (Berthier and Beebe, 2007; Lynn and Dandy, 2009; Walker and Beebe, 2002) provided an easy approach to drive fluid to flow through microchannels. However, it is difficult to directly apply this pumping method to create a concentration gradient because it lacks precise control of the flow rates and balance of the pressures between the two streams from two individual passive pumps. Considering various factors that can affect the pressure and the flow rate in passive pumping, a tiny operational variation may lead to significant drifts in the final concentration gradient.

In this chapter, a fluid circuit has been designed which could automatically generate two streams with equal pressure from two separate passive pumps. By feeding the pyramidal microfluidic circuit with these two streams, a linear concentration gradient is created and maintained at the downstream. The resulting microfluidic platform sheds syringe pumps and the complicated external connections. Its compact nature, therefore, allows the whole platform to be placed into a 75-mm diameter Petri dish and no external accessories are associated with it, which is compatible with the everyday practice of experimental cell biologists. The platform is also extremely easy for biologists to operate by themselves and to be mounted on conventional microscopes for long-term, high-resolution live-cell imaging.

5.2 Design Principle of the Pressure Balance Circuit

Compared to reported microfluidic gradient generators (Dertinger, et al., 2001; Jeon, et al., 2000), we changed the pumping component from the external syringe pumps to the semi-autonomous passive pumps. This passive pumping method (Berthier and Beebe, 2007; Lynn and Dandy, 2009; Walker and Beebe, 2002) eliminated any connections and ensured that the whole device was compact enough to be placed into a Petri dish. However, the passive pumps also face several challenges. The main issue confronting the passive pumping method is to maintain pressure equilibrium between the two feeding streams of different chemotactic agent concentrations to form a linear concentration gradient. Pressure imbalance between the two streams will disturb the side-by-side streams. As a result, they cannot be split and recombined equally in the pyramidal microfluidic circuit as expected.

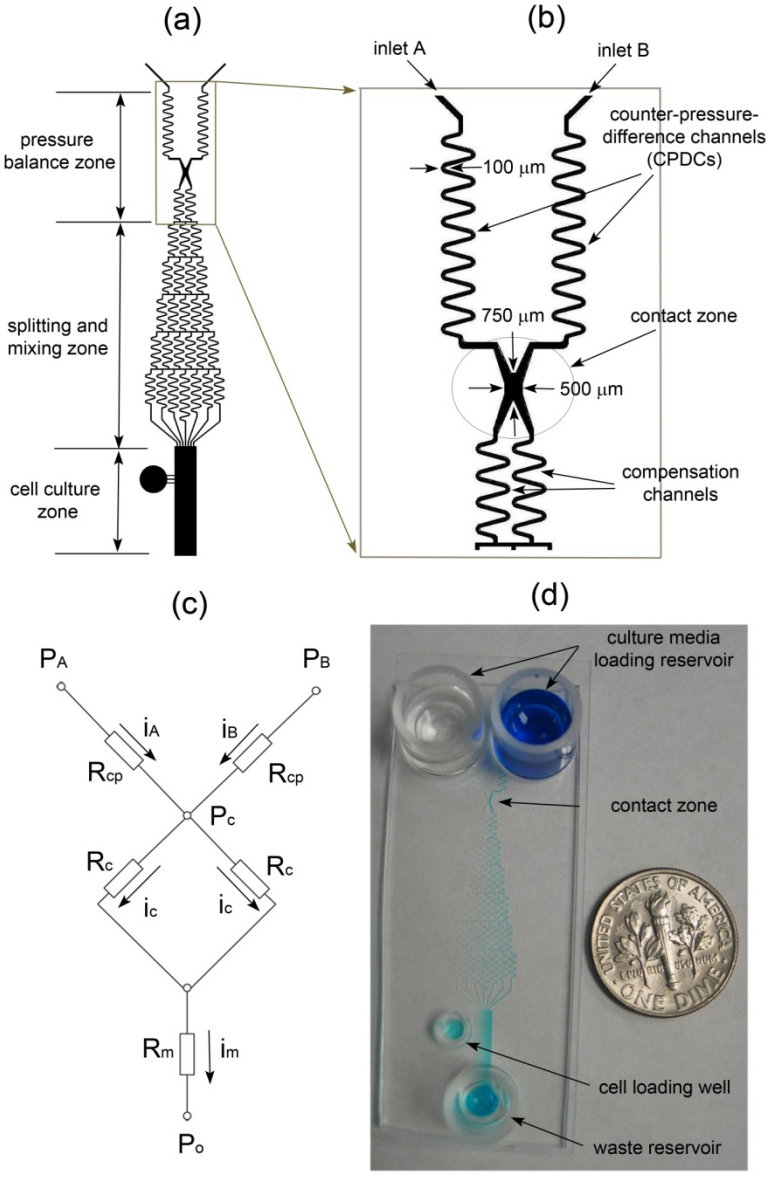

Figure 5.1: Design of the microfluidic concentration gradient generator. (**a**) A schematic of the microfluidic circuit. Once the two streams, A and B, with different concentrations of a chemotactic agent, travel through the balance zone and equilibrium zone, their flow rates and pressures become the same, which is critical for generation of a stable and linear concentration gradient in the culture and observation zone. (**b**) An enlarged view of the pressure balance zone. (**c**) An equivalent electrical circuit model. (**d**) A picture of the assembled device. Water and ink were added to the left and right reservoirs and allowed to flow through the device.

In passive pumping, the laminar flow inside the microfluidic channels and chambers is maintained by the pressure difference between the loading and waste wells (reservoirs) due to the media elevation and capillary effects (Lynn and Dandy, 2009; Walker and Beebe, 2002). It is extremely difficult to achieve a precise pressure balance between the two inlets because of the inevitable slight variations in the amount of media loaded into each well, the physical properties of the media (e.g., capillary properties, viscosities, etc.), and the inner surface properties of each reservoir. In practice, for example, the only control is to load equal amounts of media measured by a pipette; however, slight differences always exist because of the inevitable operational variations. The combination of these effects could disrupt the stable and reproducible concentration gradient (Irimia, et al., 2007). To overcome the issue of the imbalanced pressure and flow rate between the two feeding streams, we designed and implemented a fluidic circuit including a pressure balance zone at the upstream as shown in Fig. **5.1**(**a**), through which two streams with equivalent pressure were generated automatically.

The pressure balance zone includes two serpentine channels with high flow resistance functioning as counter-pressure-difference channels (CPDCs) (Fig. **5.1**(**b**)). Each channel is connected with a liquid reservoir for holding media (the passive pump). After the two fluidic steams travel down these two serpentine channels, they meet at a contact zone which is designed to equilibrate their pressures. Once passing this contact zone, the pressures of the two streams become the same. Note that mixing can occur when the media flow through the contact zone and a small portion of the media from the higher pressure stream are pushed to the stream of a lower pressure.

Each stream will flow through another serpentine channel in which the media will achieve a new uniform concentration. Then, they continuously travel down into the pyramidal microfluidic network and form a concentration gradient in the cell culture and observation zone. Due to the inevitable slight mixing at the contact zone, this microfluidic platform would provide a smaller concentration range (the concentration in the observation chamber spans a narrower range than the concentration difference between the two loading reservoirs). In the chemotaxis applications, fortunately, one normally cares for the concentration gradient that cells experience locally rather than the minimum and maximum absolute concentration in the whole chamber.

To demonstrate the design principle, an equivalent electric circuit model of the microfluidic network is shown in Fig. **5.1**(**c**). A simple analogy led to the following equation,

$$i_{\mathrm{A}} - i_{\mathrm{B}} = \frac{P_{\mathrm{A}} - P_{\mathrm{B}}}{R_{\mathrm{cp}}}, \tag{5.1}$$

where P_{A} and P_{B} represent the pressure at each inlet; R_{cp} represents the flow resistance of the counter-pressure-difference channel; and i_{A} and i_{B} denote the flow rate of each stream. Our aim is to minimize the difference between these two flow rates. According to Eqn. (5.1), this goal can be achieved through either reducing the pressure difference (P_{A} - P_{B}) or increasing the flow resistance R_{cp}. As mentioned above, a pressure difference cannot be completely avoided in reality. Therefore, one can increase the flow resistance of the counter-pressure-difference channel, R_{cp}, as a mean of diminishing the effect of the pressure imbalance, which is the reason for adding two long serpentine channels before the contact zone (Fig. **5.1**(**b**)). It is worth noting that the contact zone has been used by (Irimia, et al., 2007) and (Lee, et al., 2011); however, in

their schemes, there is no high flow resistance serpentine channels as the CPDC before the two streams meet at the contact zone.

5.3 Pyramidal Microfluidic Device using A Pressure Balance Circuit to Generate Concentration Gradient in 2D

5.3.1 Device fabrication

The microfluidic devices were fabricated using the standard soft-lithography techniques (Whitesides, et al., 2001) as presented in Chapter 2. Again, PDMS was chosen as the construction material because of its attractive features such as biocompatibility, thermal and chemical stability, and optical transparency for imaging. The mold was created using a photo-sensitive material (SU-8 2025) patterned through a transparency mask and positioned over a silicon wafer (McDonald and Whitesides, 2002). A pre-polymer solution of PDMS was then mixed with a curing agent at a 10:1 ratio and poured over the mold. After degassing, the PDMS was allowed to solidify over the molds at 70^{o}C for 2 h. The solidified PDMS layer was then peeled from the mold, and a sharp metal puncher was used to generate holes for the medium wells. After the surfaces were treated with oxygen plasma, the PDMS was bonded to a glass coverslip (No. 1, VWR Vista Vision, Suwanee, GA). The thin glass coverslip was used as the base to facilitate observations by high-resolution microscopy. The microfluidic system was finished by attaching three cloning cylinders (Fisher Scientific, Pittsburg, PA) to the punched holes as reservoirs. A picture of the final assembled devices is shown in Fig. **5.1**(**d**).

Two types of devices have been fabricated. The channel heights of both devices are 60 μm. In device I, the compensation channel and each branch in the splitting and mixing zone have a width of 100 μm and a length of 7 mm. The contact zone is 500 μm wide and 750 μm long. An 18 mm long and 100 μm wide serpentine channel works as the CPDC, whose flow resistance is 2.57 times that of the flow resistance of the compensation channel. In device II, the CPDC is replaced by a 19 mm long and 50 μm wide serpentine channel. As a result, its flow resistance increases to 9.82 times that of the compensation channel.

5.3.2 Numerical modeling of the performance

To validate the design, three-dimensional numerical modeling was performed to illustrate the working mechanisms of the pressure balance circuit. In the simulation, the diffusion coefficient of the chemotactic agent was chosen as 7×10^{-10} m^2/s (for comparison, the diffusion coefficients of glucose and glycine are 6.7×10^{-10} and 10.1×10^{-10} m^2/s, respectively (Longsworth, 1953)). The density of the media was taken as 10^3 kg/m^3 and its viscosity as 10^{-3} Pa·s. ANSYS Fluent was used to simulate the three-dimensional flow field and media concentration in the pressure balance zone. The geometries of the simulation domain were the same as the real devices.

At the inlet A, the chemokine concentration c was set to be 1, while it was set as 0 at the inlet B. The pressure at each inlet was set as 344 Pa and the pressures at the exits of the compensation channels were set as 0 Pa. This pressure difference would generate a flow rate of 15 nl/s in device I. Ideally, the two streams entering the spliting and mixing zone should have the same flow rate and pressure as shown in Fig.

5.2(**a**). In practice, however, the ideal case usually cannot be achieved. There always exists a pressure difference between the two inlets because of variations in the liquid heights in the two inlet wells, liquid surface shapes, and/or other factors in the experiment. Though Irimia et al. (2007) have designed the contact zone to overcome this issue, large imbalanced pressure would eventually generate an undesired concentration profile at the cell culture and observation zone. As shown in Fig. **5.2**(**b**), if the pressure at inlet B is higher than that at inlet A by 30%, the concentration of the left stream in the compensation channel will decrease dramatically to 0.37, instead of 0.95 as in Fig. **5.2**(**a**). This is exactly the reason that we introduce long serpentine counter-pressure-difference channels to reduce the effects of pressure difference between the two streams.

According to Eqn. (5.1), the flow rate difference between the two streams would decrease as the flow resistance of the CPDC increases. To demonstrate this effect, two more cases with the presence of CPDC were simulated. If we denote the flow resistance of each compensation channel as R, then the flow resistance of the CPDC is $2.57R$ for device I as in Fig. **5.2**(**c**) and $9.82R$ for device II as in Fig. **5.2**(**d**). With the CPDCs, even when the pressure at inlet B is higher than that at inlet A by 30%, the concentration of the left stream in the compensation channel only decreases to 0.81 for device I or 0.84 for device II, which is significantly better than that without the CPDCs. These results demonstrate that the CPDC can effectively offset the effects of the pressure difference between the two streams and diminish the effect of inlet pressure variations during device operation.

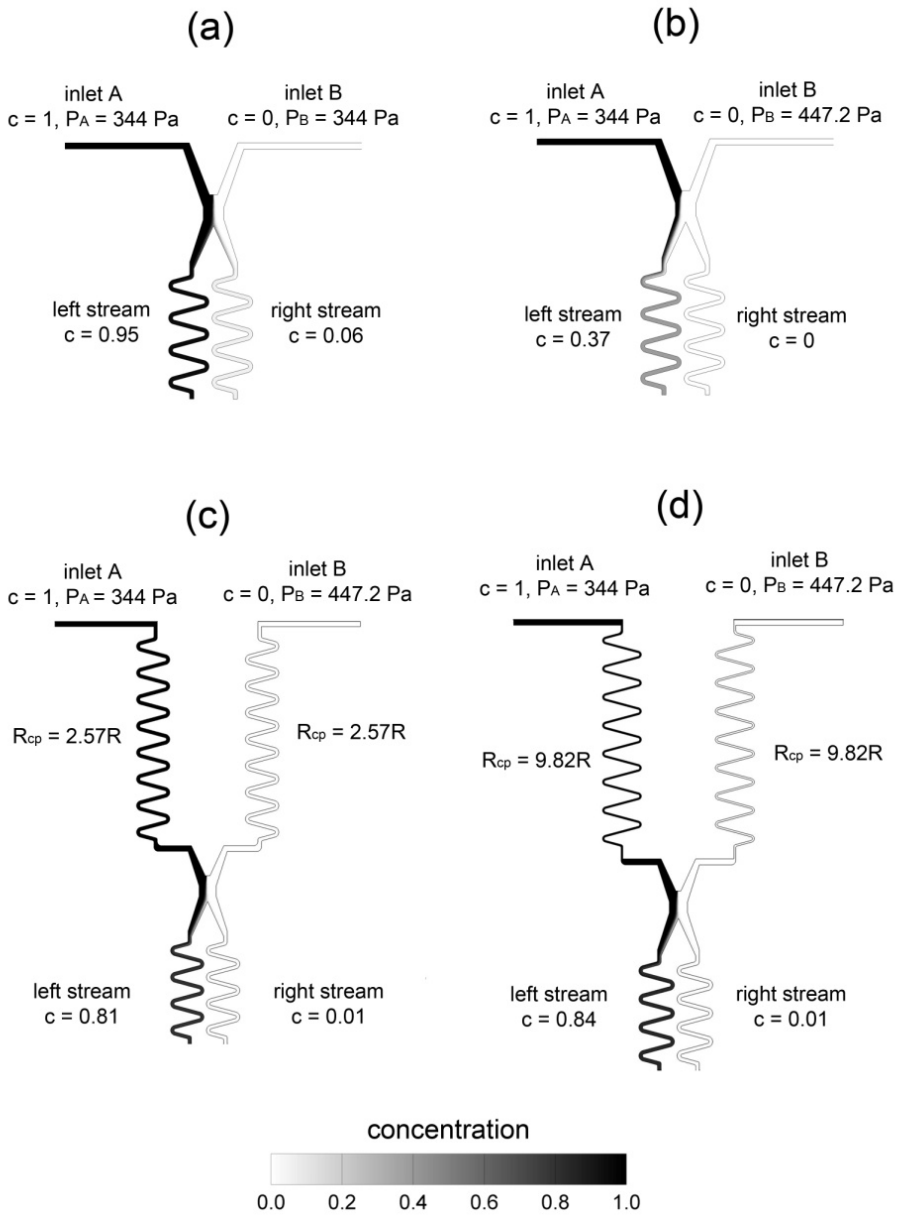

Figure 5.2: Simulation results of the concentration distribution at the top of the microfluidic network. (**a**, **b**) Without the CPDCs, the microfluidic platform will fail to generate satisfactory gradients if there exist a pressure difference between the two inlets. (**c**, **d**) With the CPDCs, a good concentration difference can be maintained even if there is a pressure difference as large as 30%. (**c**) In device I, the flow resistance of the CPDCs is 2.57 times that of the compensation channel. (**d**) In device II, the flow resistance of the CPDCs is 9.82 times that of the compensation channel.

The concentration difference between the two compensation channels is plotted in Fig. **5.3** for various pressure differences in three types of devices: devices without CPDC, and device I and II as described above. Even when the pressure difference is as high as 50%, it is still possible to obtain a reasonable concentration difference for the devices with CPDC. It is worth noting that the flow rate will reduce for the devices with a higher flow resistance, leading to more mixing at the contact zone due to diffusion. For the case with very small pressure difference, therefore, the concentration difference for Device I and II is smaller than that for devices without CPDC. However, the devices with CPDC perform much better if there is sensible pressure difference between the two inlets, providing an acceptable concentration difference feeding the pyramidal splitting and mixing network.

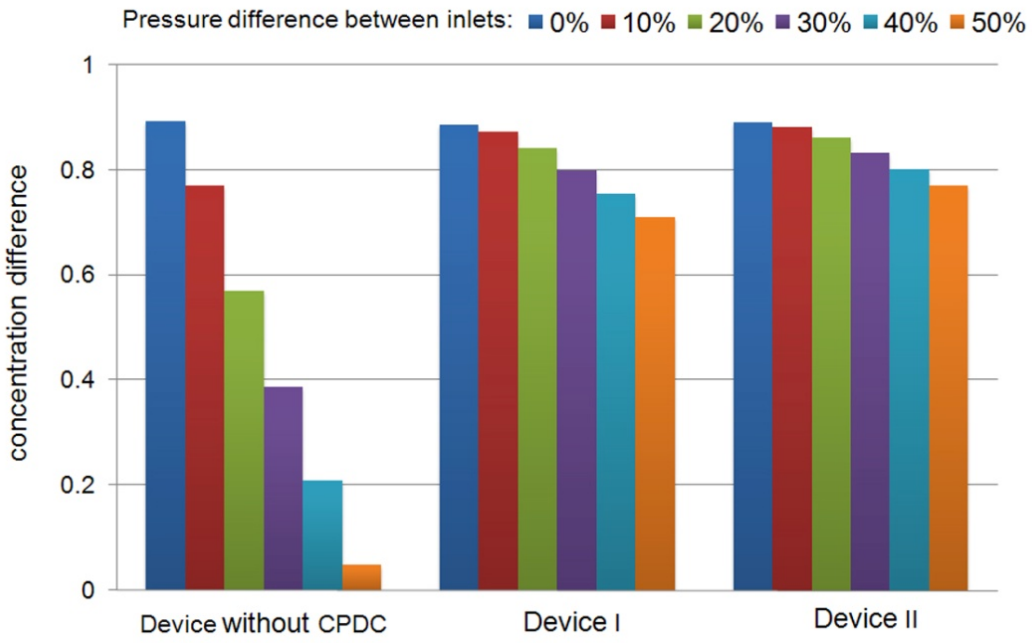

Figure 5.3: Simulation results of the concentration difference between the two streams in the compensation channels.

5.3.3 Experimental validation of the generated concentration gradient

Verification of the reagent concentration distribution was performed using digital imaging of a fluorescent marker (FITC, Thermo Fisher, Pierce, IL). The images for the concentration distribution were taken using a fluorescent inverted microscope with a CCD camera.

As shown in Fig**. 5.4**(**a**), inlet A was connected to a syringe pump to inject deionized (DI) water and inlet B was connected to a cylindrical reservoir that held FITC diluted into DI water. The cell loading well was covered tightly; and therefore, the cell loading channels would not affect the flow field in the cell culture chamber. As a result, there existed parallel laminar flows in the cell chamber, which was critical to generate a linear concentration gradient. For a short time period during the experiment, the pressure of inlet B and the outlet can be regarded as constant, and the pressure difference between the two inlets can be evaluated from the equivalent electrical circuit as (see supplementary material for detail),

$$P_{\mathrm{A}} - P_{\mathrm{B}} = \frac{[(R_{\mathrm{cp}}+2R_{\mathrm{m}}+R_{\mathrm{c}})i_{\mathrm{A}}-P_{\mathrm{B}}]R_{\mathrm{cp}}}{R_{\mathrm{cp}}+R_{\mathrm{m}}+0.5R_{\mathrm{c}}}, \tag{5.2}$$

where R_{cp}, R_{c}, and R_{m} are the flow resistance of the CPDC, the compensation channel and the splitting and mixing zone, respectively. The flow resistances R_{cp}, R_{c}, and R_{m} were calculated according to (White, 2006)

$$R = \frac{L}{\frac{4ba^3}{3\mu}\left[1-\frac{192a}{\pi^5 b}\sum_{i=1,3,5\ldots}^{\infty}\frac{\tanh\,(i\pi b/2a)}{i^5}\right]}. \tag{5.3}$$

Here b and a are half of the channel height and the channel width, respectively. The flow rate i_{A} was read from the syringe pump. The pressure of inlet B, represented by P_{B} in the equivalent circuit, was determined from the fluorescence micrographs

around the equilibrium zone. By adjusting the flow rate i_A, the two streams met in the middle as shown in Fig. **5.4**(**b**). We assumed that the two flow rates from inlet A and B were approximately equal in this case. The flow rate was recorded as i_A^0. Then the value of P_B was obtained as

$$P_B = \left(R_{cp} + 2R_m + R_c\right) i_A^0 . \tag{5.4}$$

Once P_B was determined, the pressure difference was calculated by Eqn. (5.2). Fig. **5.4**(**c**) shows the fluorescent intensity profile as the flow rate i_A was increased to 25 nl/s (corresponding to a pressure difference of 27.09% based on the calculation as described above).

The concentration profiles along the line in the cell culture and observation chamber in Fig. **5.4** are plotted in Fig. **5.5** for both types of devices. The results confirmed the effectiveness of the pressure balance circuit in the microfluidic device. With the pressure balance circuit, the microfluidic concentration generator can generate a concentration gradient even if there is a large pressure imbalance between the two inlets.

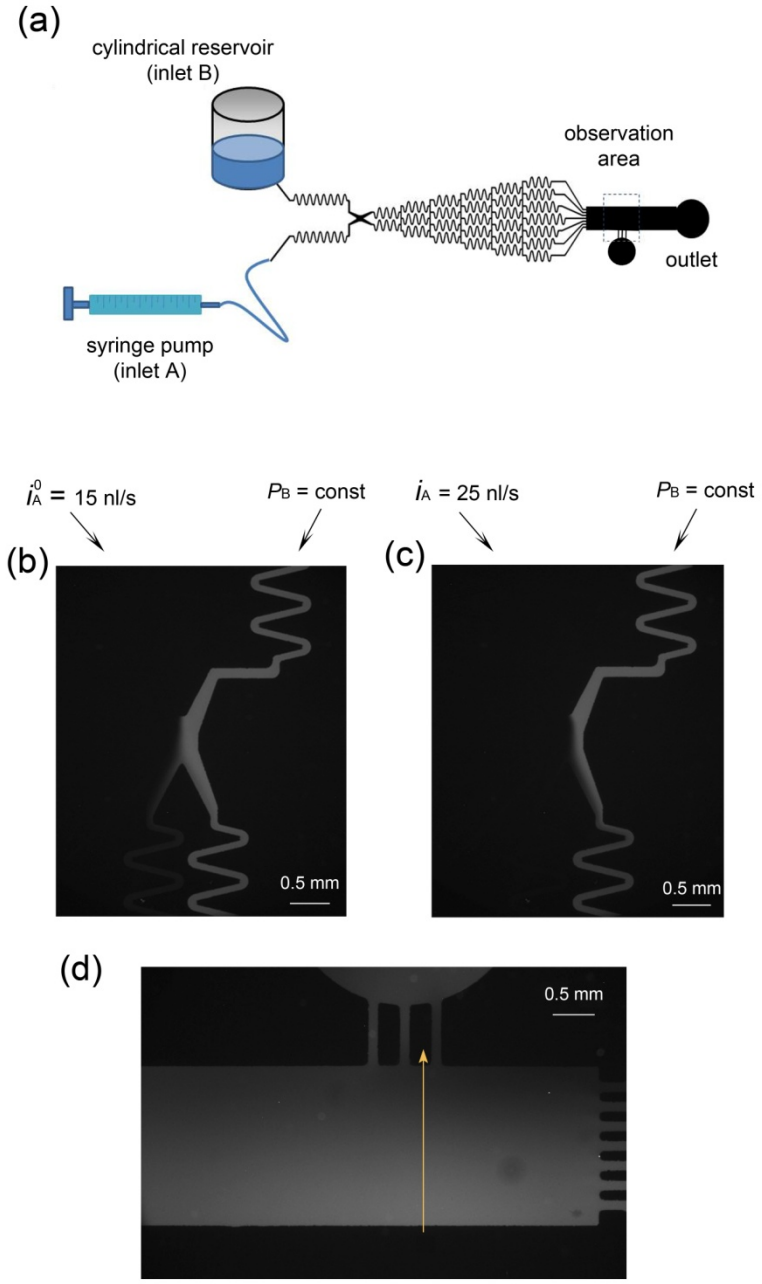

Figure 5.4: Experimental validation of the concentration gradient generator. (**a**) A schematic of the experimental set-up to verify the concentration profile. (**b**, **c**) Fluorescent micrographs around the equilibrium zone. Image (b) was used to determine the equilibrium flow rate and pressure. (**d**) A fluorescent micrograph in the cell culture and observation zone. The line was the place along which the fluorescent intensity was extracted to plot the intensity profiles in Figs. **5.5**, **5.6**, and **5.7**.

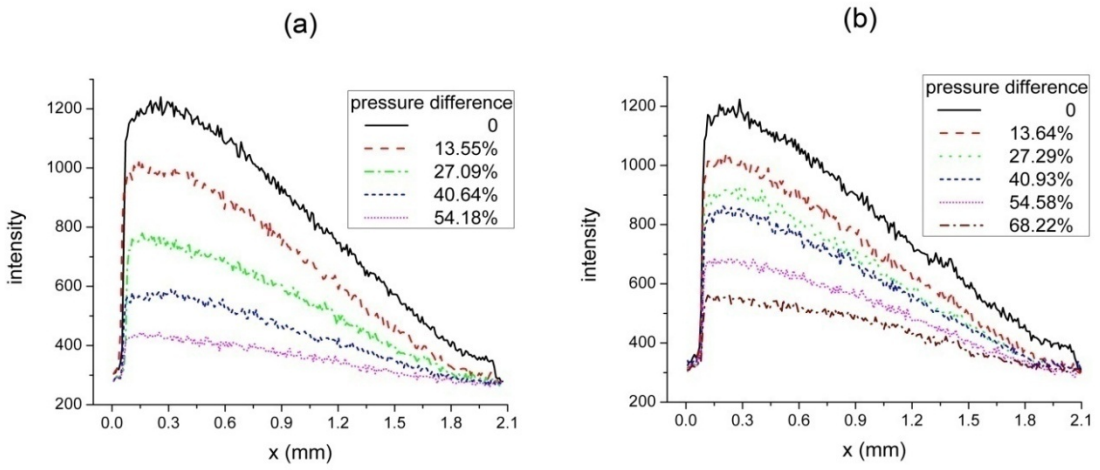

Figure 5.5: Fluorescent intensity profiles in the cell culture and observation zone. (**a**) Device I (R_b = 15,978 Pa·s/µl) (**b**) Device II (R_b = 61,009 Pa·s/µl). Both cases have R_c = 6,213.9 Pa·s/µl and R_m = 7,298.2 Pa·s/µl.

To further demonstrate the effectiveness of the pressure balance circuits, we have compared the fluorescent intensity profiles from devices with and without the balance zone. We fabricated a total of 8 type I devices (as shown in Fig. **5.1**(**d**)) and another 8 devices without the pressure balance circuits where the two streams from the passive pumps went to the splitting and mixing zone directly. During the tests, 400 µl of DI water alone or with FITC were loaded into each reservoir, respectively. After 30 minutes, fluorescent images were recorded at the cell migration chambers. The tests were repeated twice for each device by loading the FITC in different reservoirs. A total of 16 results for each type of concentration gradient generators were obtained as shown in Fig. **5.6**. It can be clearly seen that without the pressure balance circuit the intensity profiles (stars in Fig. **5.6**) are difficult to reproduce, because of the inevitable slight variations in the loading process and device parameters. However, the intensity profiles from the type I microfluidic devices (shown with solid circles) form approx-

imately linear gradients, which are bounded in a relatively narrow region. These results show that the pressure balance circuit could effectively improve the performance of the microfluidic gradient generator.

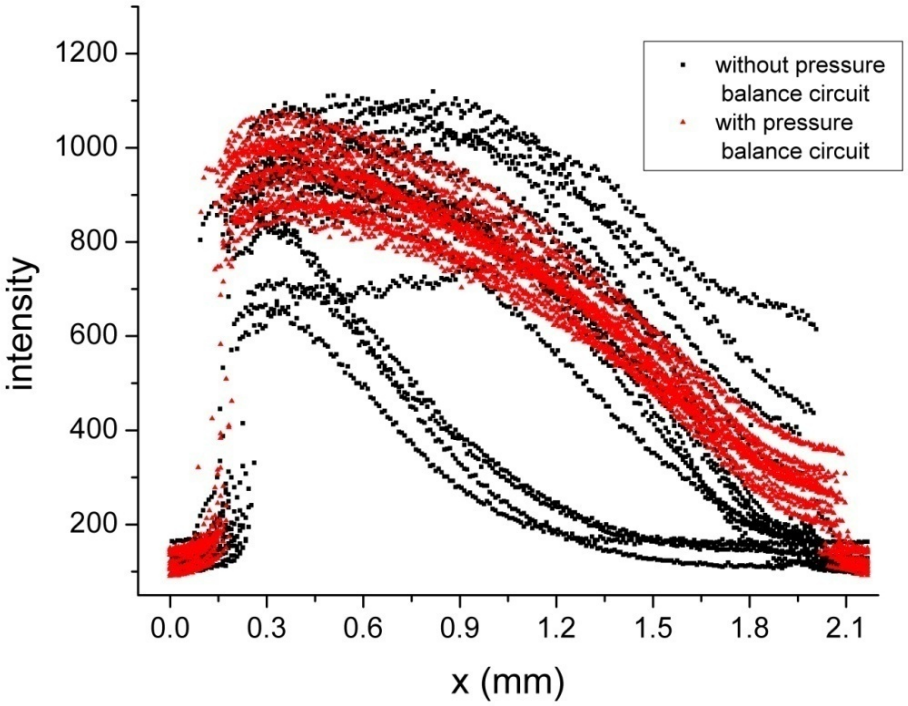

Figure 5.6: Comparison of fluorescent intensity profiles of microfluidic devices with and without the pressure balance zone.

Free from the external pumps and connections, the gradient generator utilizing passive pumps have great potential to maintain the gradient for a long time. It would be a great advantage that the concentration gradient can last for enough time so that the end users only need to add chemotactic agent and remove the cumulated waste media once or twice per day. Therefore, we also conducted an experiment to monitor the concentration profile as a function of time.

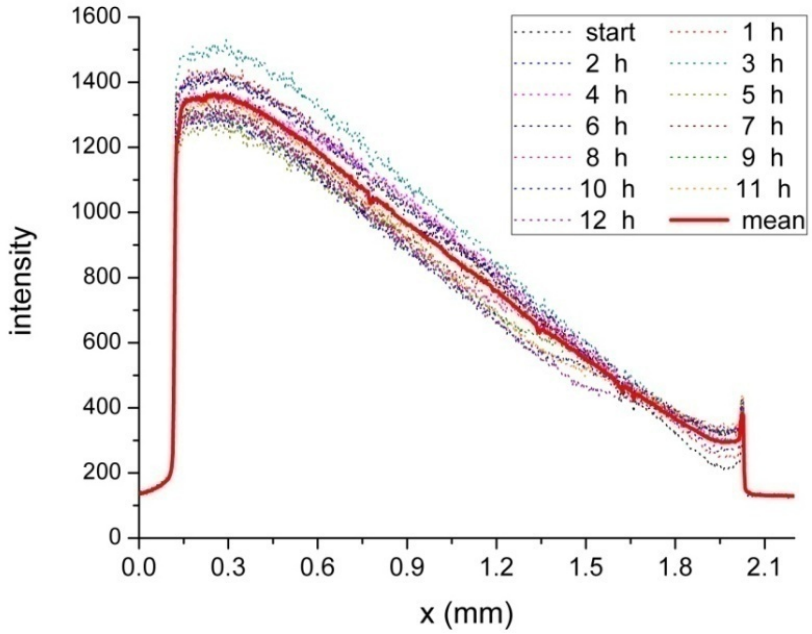

Figure 5.7: Concentration profiles for 12 h.

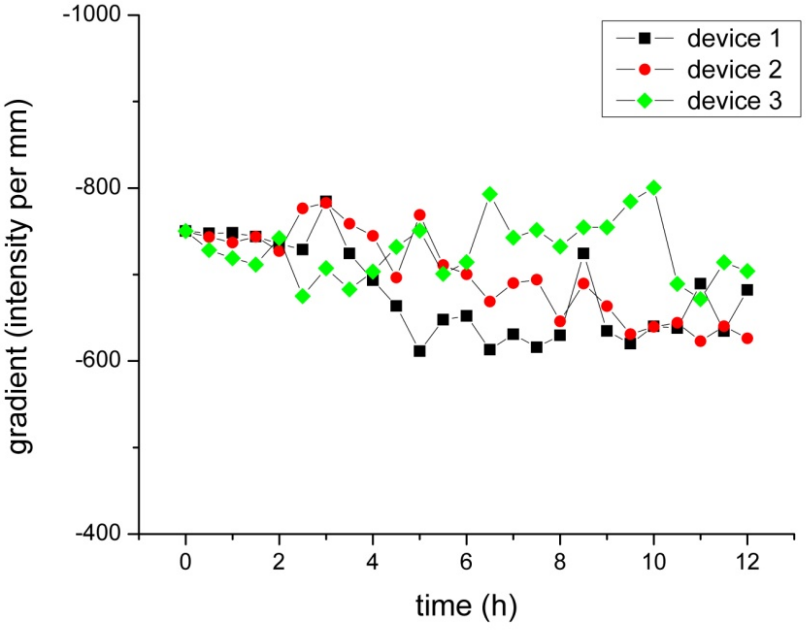

Figure 5.8: Concentration gradients versus time.

Four hundred microliters of ovalbumin (at a concentration of 0.1 mg/ml) and 400 μl of 10× PBS were loaded into the upstream reservoirs in three type II devices. The initial incomplete meniscus in the waste reservoirs generated a fast flow to build up the concentration gradient quickly. After 30 min, 100 μl of 10× PBS was added in the waste reservoir to form a complete meniscus to slow down the flow rate. This operation also avoided the abrupt flow rate change caused by the transition from incomplete to complete meniscus (Lynn and Dandy, 2009). After the loading reservoirs were covered by two slabs of PDMS to reduce the effect of evaporation, the microfluidic platform was mounted onto the microscope stage. Fluorescent images were taken every half an hour, and the results are plotted in Fig. **5.7** for one device. We also extracted the data ranging from 0.3 to 1.8 mm and found the gradient of each line (intensity per millimeter) that fitted the data in a least squares sense. The gradients at each time point for the three devices were plotted in Fig. **5.8**. The gradient profiles are relatively consistent for up to 12 h.

5.4 A Variation of the Dunn Chamber for 2D and 3D Cell Migration Studies

5.4.1 Concentration gradient in 2D

In the above described microfluidic device, liquid flow was necessary to maintain the chemotactic gradient. Even though the microfluidic device provides a method of establishing gradients quickly, the associated shear stress may yield unfavorable effects (Walker, et al., 2005). For example, soluble signaling molecules secreted by the cells may be washed away. Shear stress was also found to modulate cell's morphology and focal adhesions (Girard and Nerem, 1995). Therefore, the above concen-

tration gradient generator might not be suitable for certain biological studies. In addition, the concentration gradient changes along the flow direction due to diffusion. To address these problems, a Dunn chamber combining with the passive pumping method has been designed and implemented, in which the cells would experience a stable chemical gradients but a trivial shear stress.

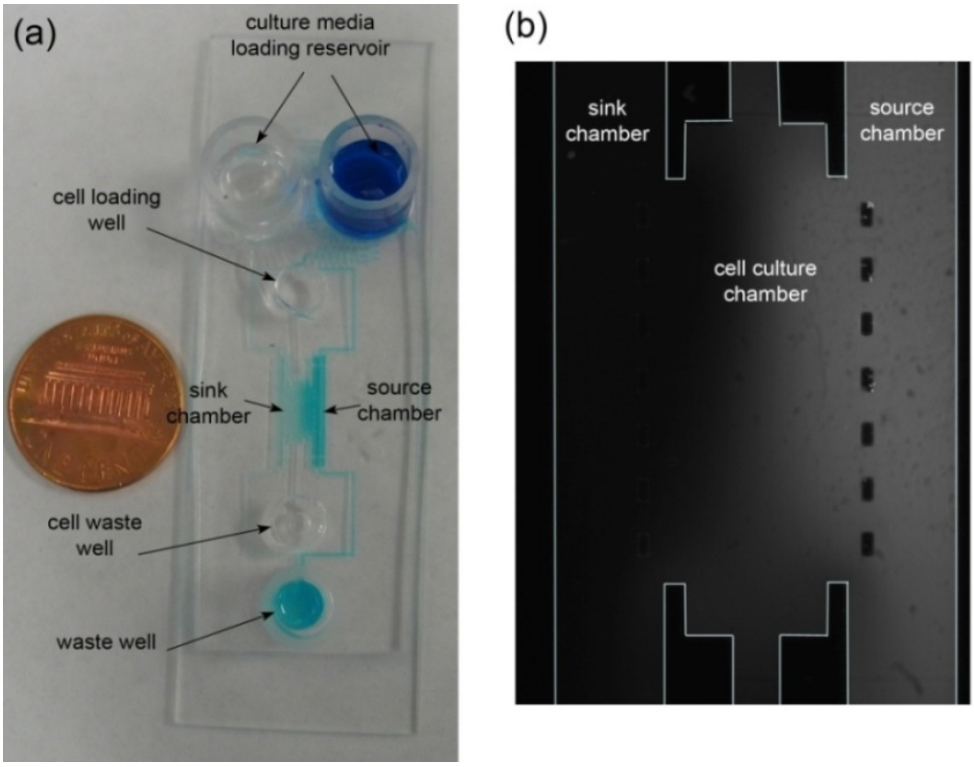

Figure 5.9: Microfluidic 2D gradient generator using the source/sink construct. (**a**) A photograph of an assembled device. (**b**) A fluorescence micrograph of FITC around the cell culture chamber.

The microfluidic platform is composed of two reagent chambers, defined as the source and sink chamber, respectively, and a cell culture chamber as shown in Fig**. 5.9**. The passive pumps and pressure balance zone are integrated at the upstream to generate two continuous streams with approximately equal flow rates and pressure to

feed the source and sink chamber. Therefore, there would be no convection in the middle cell culture chamber ideally. The chemotactic agent diffuses from the source chamber to the sink chamber and forms a static linear gradient in the middle of the cell chamber. This concentration gradient is maintained by the equal media flow in the source and sink chambers. In this design, microcapillary (Shamloo, et al., 2008) and membrane (Abhyankar, et al., 2006; Diao, et al., 2006) are excluded, which limit the transport of the chemotactic agents. In addition, the cells in the culture chamber experience a minimal shear stress.

5.4.2 Concentration gradient in 3D

The microfluidic platform using the source/sink configuration is easily modified to generate a concentration gradient in a 3D matrix. As shown in Fig. **5.10**, a mixture of cells and pre-gel solution is loaded into the middle chamber first. After polymerization, a concentration gradient in the gel is created and maintained in the middle chamber by the equal flows in the source and sink chambers.

However, if the cell-gel mixture is directly loaded into the middle chamber of the microfluidic platform as shown in Fig. **5.9**, the arbitrary flow of the culture medium into the middle chamber or the flow of mixture into the side channels can happen inevitably. The resulting mixing of pre-gel solution with culture medium can change the final composition of the matrix and its stiffness. On the other hand, the presence of gels in the side channels will change their flow resistances, inducing an uncertain concentration gradient in the cell chamber. Therefore, four pressure-controlled valves were integrated in the platform as shown in Fig. **5.10**.

The valve mechanism is shown in Fig. **5.11**. Once being activated, the valves can effectively isolate the middle chamber from the other microfluidic circuits. Therefore, these valves can successfully prevent the pre-gel solution flowing into the side channels or culture media flowing into the cell chamber to change composition of the gel.

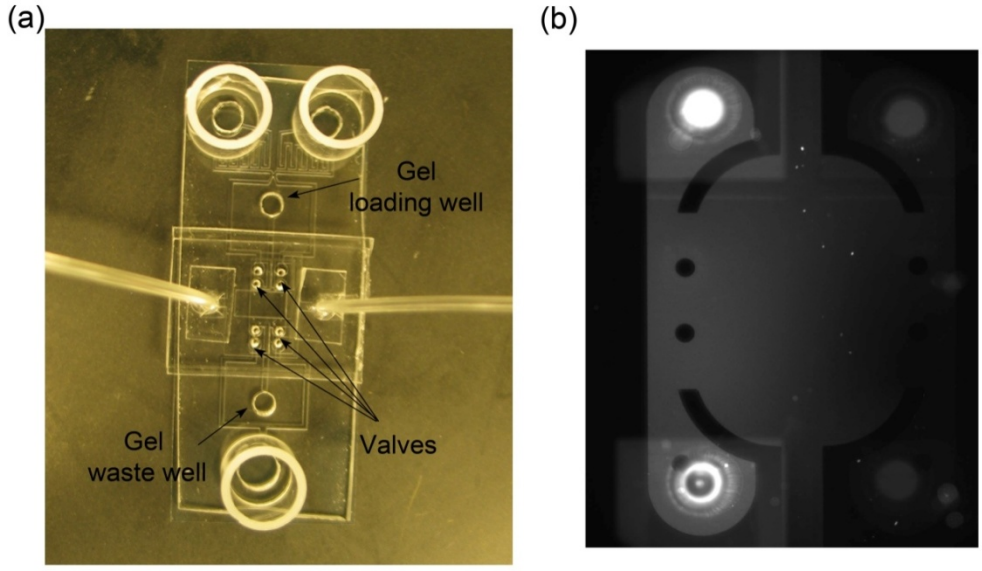

Figure 5.10: Microfluidic 3D gradient generator and the mechanism of its integrated valve. (**a**) A picture of a fabricated device. (**b**) Concentration distribution of fluorescent dye in a collagen matrix after one side reservoir was loaded with FITC.

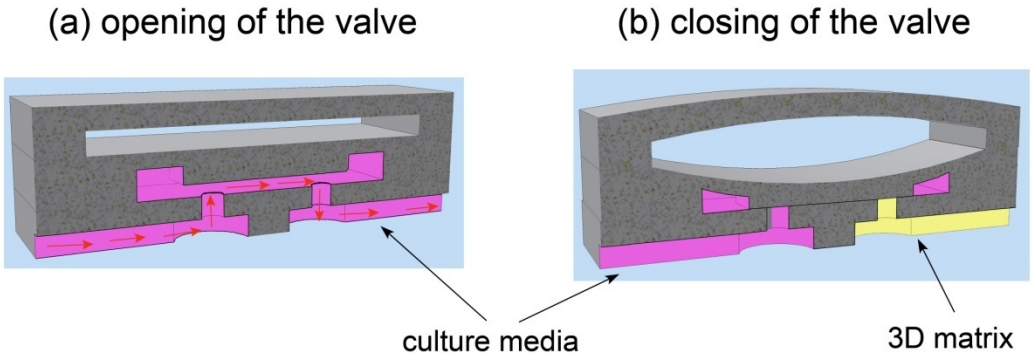

Figure 5.11: Schematic and operation of the integrated valve.

5.4.3 Cell Migration in 3D Collagen Matrices

Cell migration is a highly complex and coordinated process which includes the extension of a leading edge protrusion, the formation of new adhesions, the translocation of cytoplasm forward, and detachment of adhesions at the cell rear (Friedl and Wolf, 2003). Huge varieties of intracellular signaling molecules are involved in the migration process. The Rho family of small GTPases, particularly Rac, Cdc42, and Rho, are thought to be the central coordinators in cell migration (Schwartz and Shattil, 2000). Rac is required at the front of the cell to regulate actin polymerization and induce new adhesion formation (Rottner, et al., 1999). Cdc42 is required for the establishment of cell polarity, which is essential for directed migration (Etienne-Manneville and Hall, 2003). Rho is thought to associate with the maturation of adhesions and regulate the contraction and retraction force required in the cell body (Raftopoulou and Hall, 2004).

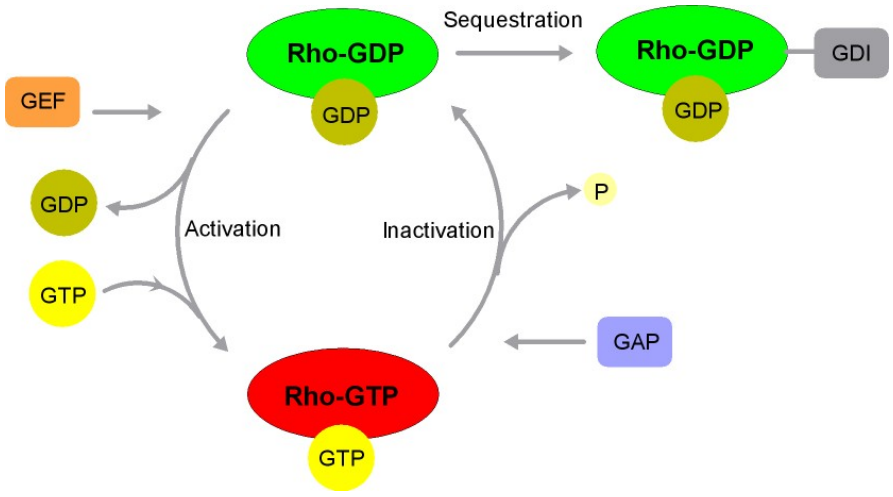

Figure 5.12: Mechanisms of Rho-protein regulation. GDP, guanosine diphosphate; GTP, guanosine triphosphate; P, phosphate; GEF, guanine nucleotide exchange factor; GAP, GTPases-activating protein; GDI, guanine nucleotide dissociation inhibitor.

The Rho family of small GTPases cycle is regulated by three groups of proteins as shown in Fig. **5.12**. Guanine nucleotide exchange factors (GEFs) activate the GTPases directly through the exchange of GDP for GTP while GTPases-activating protein (GAP) stimulate the activity of the GTPase to hydrolyze its bound GTP molecule to GDP, and guanine nucleotide dissociation inhibitor (GDI) is thought to block the GTPases (Raftopoulou and Hall, 2004).

We applied this microfluidic platform to study the role of Asef2, a Rho family GEF, in cell migration. Asef2 is thought to regulate cell migration via modulation of the actin cytoskeleton (Kawasaki, et al., 2007; Sagara, et al., 2009). HT1080 fibrosarcoma cell lines were generated to stably express low levels of GFP-Asef2 or GFP. Compared to the GFP control cells, cells expressing GFP-Asef2 contained 2-3 folds increased levels of active Rac and active Cdc42, and had approximately 50% decreased levels of active RhoA (Bristow, et al., 2009). On a collagen coated surface, the GFP-Asef2 cells migrated slower than the GFP control cells (unpublished data), which was contradictory to observations made on substratum coated with fibronectin, where GFP-Asef2 cells had a migration advantage over the GFP control cells (Bristow, et al., 2009). To better understand the mechanism of the GFP-Asef2 effects on cellular migration in a 3D matrix, we utilized these microfluidic devices to create a 3D collagen matrix for cell migration analyses.

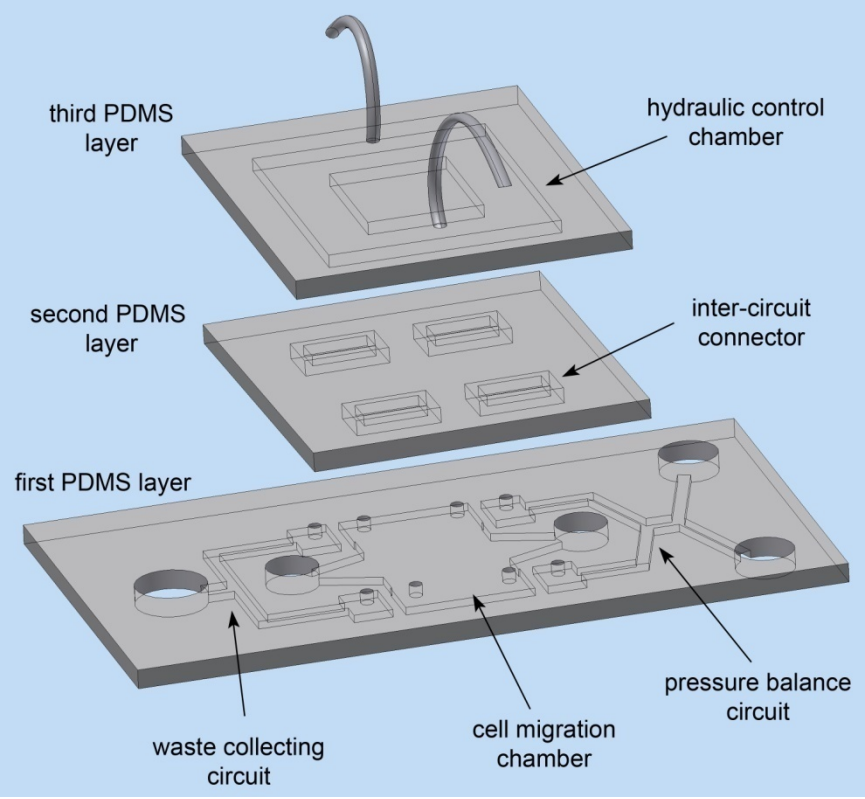

Figure 5.13: Schematics of the PDMS layers of the 3D gradient generator. The first PDMS layer defines a pressure balance circuit, a cell migration chamber and a waste collecting circuit. The second PDMS layer connects these three circuits. The connection was controlled by pressure inside the third PDMS layer.

The microfluidic platform was fabricated using the soft-lithography techniques as described in section **2.2**. SU-8 2150 (Microchem, Newton, MA) generated 500 μm high mold for the first PDMS layer (Fig. **5.13**). The high chamber would facilitate the matrix loading. After peeled off from the mold, four pairs of 700 μm in diameter holes were punched in the first PDMS layer. Each pair of holes was connected by the second PDMS layer as shown in Fig. **5.13**. The third PDMS layer defined a hydraulic control chamber as an overall switch for the lower four connectors. These three PDMS layers were stacked to sit on a thin (0.13-0.16 mm) coverslip (No. 1, VWR

Vista Vision, Suwanne, GA), which was selected to facilitate imaging at high resolution during microscopy.

Once liquid (PBS or DI water) was injected into the control chamber through the attached microbore tubes which were clamped at the two ends, the cell migration chamber was effectively isolated from the other two circuits. Subsequently, a cell-gel mixture was loaded into the middle chamber. Because the cell migration chamber was disconnected from the media providing and collecting channels, the culture media would not flow inside the pre-gel solution or vice versa. As a result, the composition of the cell-gel mixture loaded remained consistent among experiments and flow resistance of side channels kept symmetric.

HT1080 cells were first trypsinized using 0.25% trypsin and suspended in SF DMEM at a density of 60,000 cell/ml. The 3D collagen matrix was prepared by homogeneously mixing 5 µl 10× DMEM (GIBCO® Carlsbad, CA), 6.7 µl DI water, 0.86 µl 1 N NaOH for optimal pH, and 37.5 µl rat tail type I collagen (3.66 mg/ml stock) (BD Biosciences, Dan Jose, CA). The cell impregnated collagen matrix was made by adding 50 µl of cell suspended medium to the collagen solution, to achieve a final concentration of 1.5 mg/ml collagen and 30,000 cell/ml. The mixture was subsequently added to the loading well while the whole device was placed on ice. Vacuum was not required because the flow rate was adequate for loading the cells because of the big chamber. To achieve a homogeneous distribution of cells, the platform was flipped upside down and put into a humidified incubator at 37^{o}C. After 10 min, the platform was flipped over and put back into the incubator for another 30 min to allow for polymerization of the matrices, after which 10% fetal bovine serum (HyClone La-

boratories Inc., Logan, UT) plus 1% penicillin-streptomycin (GIBCO® Carlsbad, CA) supplemented DMEM was filled into the reservoirs to maintain the culture.

When grown in these 3D matrices, the cells show a spindle-shaped morphology as evidenced in the z-stack images obtained by reflection microscopy (Fig. **5.14**), which also show the distribution of collagen fibrils. As shown in Fig. **5.14**, we were able to obtain a homogeneous distribution of cells in the 3D matrix within the 500 µm high chamber. Once mounted onto an environmental chamber attached to the confocal microscope, live-cell imaging was performed to investigate cell migration in real-time. Figure **5.15** shows a series of images of the migration process. The original images were taken for 10 hours with 5 min intervals. As shown in Fig. **5.15**, the cell morphology dramatically changed during migration. The cells exhibited thin, long or branched protrusions with ultimate translocation of the cell body in the 3D matrix.

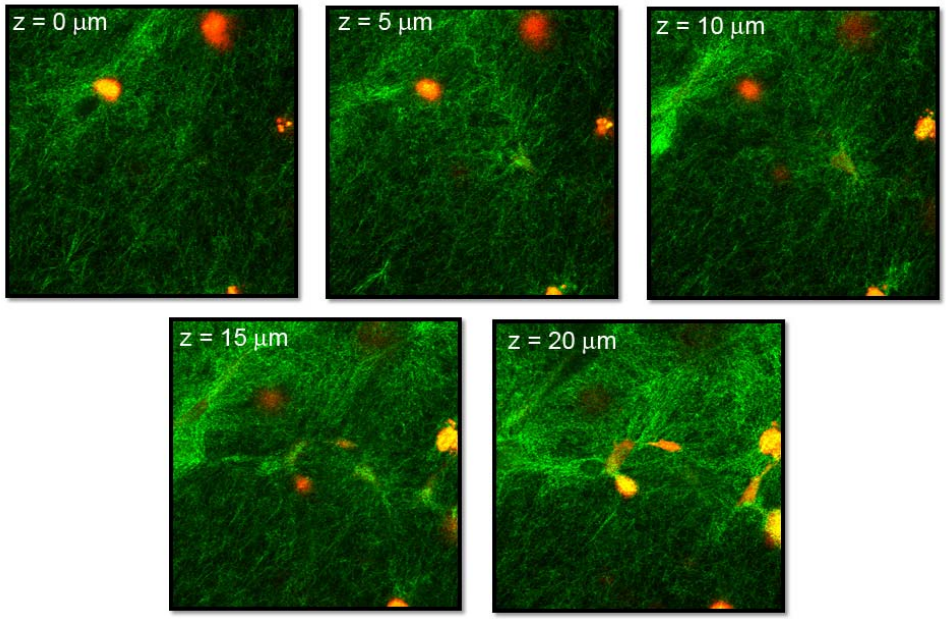

Figure **5.14**: Z-stack images of HT1080 cells in collagen matrix acquired by reflection microscopy (a slice thickness of 5 µm averaged over two frames scale).

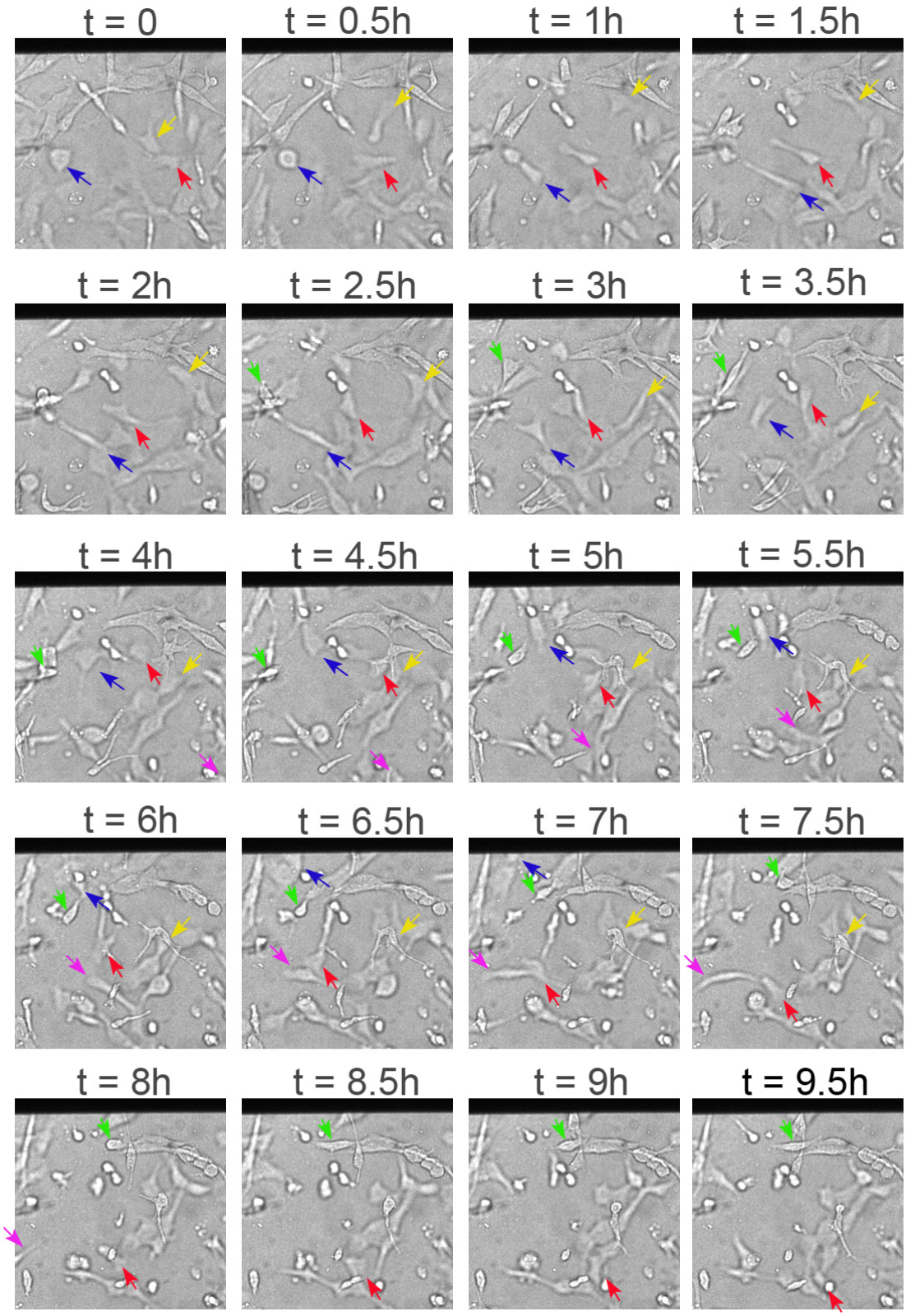

Figure 5.15: Time lapse images of HT1080 cell migration in a collage matrix.

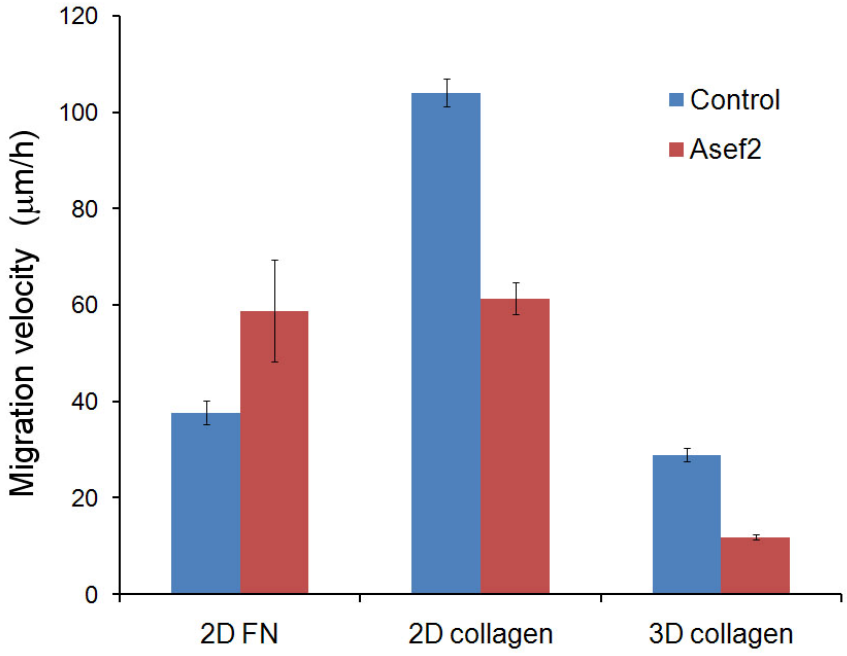

Figure 5.16: Migration velocity of GFP (control) and GFP-Asef2 cells on a 2D surface and in a 3D matrix.

We also tracked the migration path and speed using live-cell imaging. While the migration velocity of GFP-Asef2 cells increased on 2D fibronectin coated surface (Bristow, et al., 2009), we found that the migration velocity of GFP-Asef2 cells was slower compared with GFP control cells (Fig. **5.16**) on collagen coated surface. We found the same pattern in the 3D collagen matrix. The conflict indicated that the cells were regulated via a different signaling pathway and might differentially regulate adhesion dynamics during their migration in the 3D matrix. Interestingly, Rac, not Cdc42, is essential for Asef2-mediated migration and adhesion turnover on a 2D surface (Bristow, et al., 2009). Adhesions in GFP-Asef2 cells were small and had fast assembly and disassembly rates (Bristow, et al., 2009). The current study, however,

suggested that other signaling mechanisms may also play roles in Asef2-mediated migration when cells were moving in a 3D collagen matrix.

From these results, we conclude that this microfluidic assay has a preliminary success and discloses significantly different cell migration behaviors in a 3D environment. Because modulations of cell migration and adhesion in 2D settings have limitations in predicting the cellular responses found in real organisms, the limitation of traditional planar migration highlights the urgent need to study cell migration in a 3D matrix. The developed microfluidic device appropriately offers such a platform to culture cell in a 3D matrix.

5.5 Summary

To develop compact microfluidic cell culture platforms for establishment of a concentration gradient using the passive pumping method, we have designed a pressure balance fluidic circuit that could automatically generate two streams with equivalent pressure and flow rate. Numerical simulations and fluorescent imaging confirmed the function of the fluidic circuit. By feeding a pyramidal microfluidic circuit with the two streams from two individual passive pumps, a linear concentration gradient was created and maintained at the downstream. The concentration gradient is stable and reproducible.

A variation of the Dunn chamber was also developed using the pressure balance circuit, in which cells in the culture chamber would experience minimal shear flow. More importantly, this type of device could be used to produce a concentration gradient in a 3D matrix and to study cell migration in the 3D framework.

Initial cell migration studies have also been performed in these chambers, even though at this stage the purpose is still to obtain the baseline instead of studying cell migration in response to a concentration gradient. Interestingly, the experiments did show that the cell migration behavior in 2D and 3D can be different in response to the regulation of certain molecules.

Taking advantage of the passive pumping, the whole device was compact enough to fit inside a Petri dish. No external accessories, such as syringe pumps and connections, were associated with these devices, which is a favorable feature to biologists. This microfluidic gradient generator offers a platform for a facile way of long-term imaging and analysis using high-resolution microscopy. It has the potential of gaining wide acceptance as a routine tool for a range of basic and applied studies of cell migration. Finally, the pressure balance fluidic circuit used in this study may be applied to a variety of lab-on-a-chip applications requiring a balanced pressure among different flow streams.

CHAPTER 6

SUMMARY AND OUTLOOK

6.1 Summary

This dissertation has developed several microfluidic platforms to manipulate various aspects of the microenvironment of cells in culture and co-culture. A couple of innovative features and designs have been implemented to facilitate biological research. All platforms share several common biologically favorite characteristics. Passive pump provides sufficient culture media to maintain long-term cell culture and co-culture. By virtue of exquisite portability and easy operation, the chance of introducing contamination are significantly reduced. All devices sit onto a thin and high optical quality coverslip, suitable for live-cell investigations using high-resolution microscopy. Replicating modeling using PDMS as the construction material makes the final device low cost and disposable in addition to increasing the homogeneity of devices and the throughput of experiments.

A microfabricated valve has been integrated in an effort to establish platforms to control the interactions between two adjacent cell populations. We demonstrated the feasibility of co-culturing two groups of cells in side-by-side and vertically-layered configurations. Taking advantage of the integrated valve, each cell population can be individually treated without affecting the other. This dissertation is the first to demonstrate live-cell imaging of dynamic synapse formation between two CNS neurons transfected to express different fluorescent proteins, which represents a significant

technology breakthrough opening the door for dissecting the molecular mechanisms of spine and synapse formation. The platform enables crosstalk between two cell populations in a controllable and reproducible fashion, which has been demonstrated by neuron-glia co-culture and cancer-endothelial cell cross-migration under different conditions. The importance of cell microenvironments in cell-cell interactions has been demonstrated in the cross-migration of tumor cells and endothelial cells under normoxic and hypoxic conditions. The platform also enabled *in vitro* examination of cross migration of both cells mediated by different ligand-receptor pairs, which help to dissect the functions of these molecules.

This dissertation has also developed two innovative new techniques for probing cellular signaling pathways. Spatial separation through a permeable barrier prevents a miscellany of cell populations but permits communication through soluble signaling molecules alone. Furthermore, the barrier has been engineered to prohibit the transport of certain molecules. Therefore, specific extracellular signaling pathways can be selectively blocked without any genetic modifications of the cells. I believe that applications of these platforms could be greatly helpful in fundamental biological and therapeutic studies.

A pressure balance fluidic circuit has been developed to automatically generate two liquid streams with equal pressure and flow rate. Integrated with this circuit, the platform has the ability to create and maintain a linear and stable concentration in 2D and 3D for a long time while keeping its user-friendly interface. No other accessories are associated with these devices. This innovative design provides a superior and via-

ble alternative to the microfluidic cell migration assays using expensive external syringe pumps.

Finally, this dissertation has demonstrated the implications of microfluidic platforms for cell culture and cell migration in a 3D matrix to better predict the cellular responses. Moving from cell monolayer to 3D environment is a new tread in *in vitro* cell biology studies. Microfluidics offers a well-suited way to establish assays to support 3D cell culture as shown by the cell migration platform. I believe that all these platforms have the potential to gain wide acceptance as daily tools for a range of fundamental and clinical studies.

6.2 Outlook, Challenge and Future work

This dissertation has explored examples in controlling various aspects of the cellular microenvironment in cell culture and co-culture. Possible future work includes new applications of these devices for investigations of other interesting cellular interactions to answer important biological questions. I particularly speculate that employment of the ligand traps to probe signaling pathways will make a huge impact on cell biology. However, one of the main challenges is to effectively conjugate the interested ligands' receptors onto nanoparticles at a high concentration. In our experiments, we found that nanoparticles tended to accumulate during the polymerization process of the gel. For a functioning device, the nanoparticles need to distribute homogenously in their scaffold. More experiments need to be performed to find an appropriate condition such as temperature, pH value and solution contents, which not only allows gel for polymerization but also prevents the accumulation of nanoparticles.

In this dissertation, only the simplest form, a straight valve barrier, has been implemented. Other shape, such as a circle, can be generated in a similar way in the future work for more complex devices. Additionally, only one valve-controlled barrier has been integrated in each platform. In the future, without being limited, the method using a controlled physical barrier can be easily extended to individually-controlled multiple barriers for multiple-chamber systems to regulate the interaction among more than two populations. Taking the matter further, not only can the particles embedded barrier be patterned between cell populations, but also cell containing scaffold can be created in a similar manner, providing a unique opportunity to generate complex but more interesting multi-cell co-culture configurations.

Another direction for the technology is to develop sophisticated systems to integrate additional functionality. For example, micro-electrodes can be used to stimulate and record the activities of neurons. We also can integrate new glucose and oxygen sensors to monitor the metabolic rates of the cultured cells and novel sensors to measure the cell migration force. However, an ongoing challenge is to trade the easy operation and low cost for the potential gain from these additional functionalities. More effort to communicate ideas between engineers and biologists is critical to address this issue.

Culturing cells in 3D has the potential to improve the physiological relevance of cell-based assays. Microfluidics is expected to play a significant role in utilizing 3D cell culture by forming the scaffold, providing continuous nutrition, and integrating analysis tools. However, many challenges still remain to fully establish a mainstream approach to reduce the gap between cell cultures and physiological tissues.

Transport of nutrients and growth factors is known to be hindered in a 3D matrix. Both matrix composition and cells' distribution are correlated to the diffusive and convective hindrance, especially for large biological molecules. Cell adhesion and migration speed also responds to the steric and mechanical properties of the matrix. Matrix compliancy should be considered as an additional parameter to construct a biological model. In addition, information to collect and analyze increases exponentially after moving from a 2D into a 3D context. Innovative acquisition tools are required and new theoretical models shall be developed to account for this change. However, despite all these challenges, I optimistically believe that the integration of engineering and cell biology will lead to new standard protocols and quantitative analysis methods impacting on both fundamental and therapeutic studies.

APPENDIX

A. Two-layer Photolithography Protocol

1. Spin-coat: SU-8 2005
    - Dispense photoresist onto silicon wafer
    - Spin at 500 rpm for 5 seconds
    - Spin at 3000 rmp for 30 seconds
    - Spin at 500 rpm for 5 seconds
2. Soft bake
    - 65 ^{o}C for 1 minutes
    - 95 ^{o}C for 2 minutes
3. Exposure: expose wafer to UV light through the transparency mask
    - 400 mW/cm^2 × 5
4. Post exposure bake
    - 65 ^{o}C for 1 minutes
    - 95 ^{o}C for 3 minutes
5. Development: develop in SU8 developer on spinning machine and rinse with acetone.
6. Hard Bake:
    - 120 ^{o}C for 30 minutes
7. Spin-coat: SU-8 2050
    - Dispense photoresist onto silicon wafer
    - Spin at 500 rpm for 5 seconds
    - Spin at 1650 rmp for 30 seconds
    - Spin at 500 rpm for 5 seconds
8. Soft bake
    - 65 ^{o}C for 5 minutes
    - 95 ^{o}C for 20 minutes
9. Exposure: expose wafer to UV light through the transparency mask

- 400 mW/cm^2

10. Post exposure bake
    - 65 ^{o}C for 1 minutes
    - 95 ^{o}C for 10 minutes
11. Development: develop in SU8 developer on spinning machine and rinse with acetone several times.
12. Hard Bake:
    - 120 ^{o}C for 30 minutes

B. Five Hundred Micrometre High Photolithography Protocol

1. Spin-coat: SU-8 2150
    - Dispense photoresist onto silicon wafer
    - Spin at 500 rpm for 60 seconds
    - Spin at 1400 rmp for 30 seconds
    - Spin at 500 rpm for 10 seconds
2. Soft bake
    - 65 ^{o}C for 10 minutes
    - 95 ^{o}C for 120 minutes
3. Exposure: expose wafer to UV light through the transparency mask
    - 400 mW/cm^2 × 3
4. Post exposure bake
    - 65 ^{o}C for 5 minutes
    - 95 ^{o}C for 30 minutes
5. Development: immerse into SU8 developer for 20 minutes and then develop on spinning machine and rinse with acetone several times.
6. Hard Bake:
    - 120 ^{o}C for 30 minutes

C. Transfection of Neurons

The plasmids used for transfection of neurons were as follows: TSα2-m-Cherry construct, TSα2-EGFPC1, pre-synaptic protein construct, m-Cherry-pLL3.7-Synaptophysin (a generous gift from Anne Marie Craig, University of British Columbia, Canada) and the post-synaptic protein construct, TSα2-EGFP-PSD-95.

The neurons are transfected on DIV3-4 with a modified calcium phosphate method. Two separate DNA expression vectors, one tagged with green fluorescent protein EGFPC1 and another with m-Cherry at varying concentrations ranging from 2.5μg to 4.0μg are mixed separately in tubes containing 45μl of 120 mM $CaCl_2$ solution. A co-precipitate containing calcium phosphate and DNA is formed by slowly bubbling 45μl of HEPES-buffered (HBS) solution (pH 7.05) in the tubes. An additional 45μl of culture media is added to the mixture which is allowed to stand for 5 min at room temperature to facilitate the precipitate formation.

Before adding the transfection mixtures, 0.2-0.3 ml of air is injected into the air chamber to press the barrier valve down and isolate the two chambers. The media in the reservoirs and the waste wells of the chips are also removed. To begin the transfection process, 45 μl of each of the separate calcium phosphate- DNA- transfection mixtures are loaded in the respective cylinders. The precipitates can be observed under the microscope and their flow can be monitored in the chambers. After ensuring that an adequate flow rate is achieved and there is an even distribution of the precipitates over the cells, the devices are replaced in the incubator. After 10-15 min, a drop of culture media is added in the waste well to reduce the fluid flow. This ensures the deposition of the precipitates over the cells within the chambers and minimizes their loss

into the waste wells. The chambers are incubated at 37 ^{0}C for another 1-1.5 hours depending on the general health of the cells that can be monitored occasionally. After about 1.5 hours, the transfection mixtures are removed, and replaced with pre-warmed wash buffer (HBS) at a pH 7.15, and the devices are returned to the incubator. The wash buffer hastens the dissolution and removal of the excess precipitates in the chambers that were not taken up by the cells. After approximately 1 hour of washing, the liquid in the reservoir cylinders are replaced with 300 µl of fresh glia-conditioned B27 culture media. The air is released from the air chamber after unclamping the microbore tube. A slight negative pressure is occasionally applied to ensure the complete release of the barrier valves from their pressed position.

D. MATLAB code for concentration in the semi-permeable barrier

```
clear all
Pe = 10.0;                          % Peclet number
Da = 100.0;                         % Damkohler number
Phi_A = double(1.0);                % partition coefficient for A

NN = 5000;                          % number of eigenvalues

beta = zeros(1,NN,'double');        % eigenvalues

t = 0.5;                            % time

dx = 0.01;
x = 0 : dx : 1;                     % positions

theta = x .* 0.0;                   % initial of theta
theta(1) = Phi_A;

for i = 2 : length(theta)
        for   n = 1 : NN
                an = 2.0*( (beta(n)*beta(n) + Pe*Pe/4.0) )/...
                ( beta(n)*beta(n) + Pe*Pe/4.0 + Pe/2.0);
                bn = ( beta(n)*beta(n) + Pe*Pe/4.0 + Da ) / Pe;
                theta(i) = theta(i) + ( (1- exp(-bn*t)) * exp(0.5*Pe*x(i))*...
                sin(beta(n)*x(i)) ) * Phi_A * an * beta(n) / Pe / bn;
        end
end

% steady state to check the solution
theta_s = x.*0.0;
theta_s(1) = Phi_A;

for i = 2 : length(theta_s)
        rho = double(sqrt(Pe*Pe/4.0+Da));
        A = double(Phi_A);
        B = -double(A*(rho*tanh(rho)+0.5*Pe)/(rho+0.5*Pe*tanh(rho)));
        theta_s(i) = (A+B*tanh(rho*x(i)))*(1+exp(-2*rho*x(i)))...
                /2.0/exp(-rho*x(i))*exp(0.5*Pe*x(i));
end

plot(x,theta,'b',x,theta_s,'r');

% save results in a file
fid = fopen('results.txt','w');
fprintf(fid, 'Pe=%12.6f\n',Pe);
fprintf(fid, 'Da=%12.6f\n\n',Da);
fprintf(fid, 'beta=\n');
fprintf(fid, '%12.8f\n',beta);
fprintf(fid, '\n\nx=\n');
fprintf(fid, '%10.8f\n',x);
fprintf(fid, '\n\ntheta=\n');
fprintf(fid, '%10.8f\n',theta);
fclose(fid);
```

REFERENCES

Abate, A. R. and Weitz, D. A. (2008). Single-layer membrane valves for elastomeric microfluidic devices. *Appl Phys Lett***, 92,** 243509.

Abbott, A. (2003). Cell culture: biology's new dimension. *Nature***, 424,** 870-872.

Abhyankar, V. V., Lokuta, M. A., Huttenlocher, A. and Beebe, D. J. (2006). Characterization of a membrane-based gradient generator for use in cell-signaling studies. *Lab Chip***, 6,** 389-393.

Alberts, B. (2002). *Molecular biology of the cell*, 4th edn. Garland Science: New York.

Allen, N. J. and Barres, B. A. (2005). Signaling between glia and neurons: focus on synaptic plasticity. *Curr Opin Neurobiol***, 15,** 542-548.

Allen, N. J. and Barres, B. A. (2009). NEUROSCIENCE Glia - more than just brain glue. *Nature***, 457,** 675-677.

Armani, D., Liu, C. and Aluru, N. (1999). Re-configurable fluid circuits by PDMS elastomer micromachining, *Micro Electro Mechanical Systems, 1999* City, pp. 222-227.

Atencia, J. and Beebe, D. J. (2005). Controlled microfluidic interfaces. *Nature***, 437,** 648-655.

Bains, J. S. and Oliet, S. H. (2007). Glia: they make your memories stick! *Trends Neurosci***, 30,** 417-424.

Berthier, E. and Beebe, D. J. (2007). Flow rate analysis of a surface tension driven passive micropump. *Lab on a Chip***, 7,** 1475-1478.

Berthier, E., Warrick, J., Casavant, B. and Beebe, D. J. (2011). Pipette-friendly laminar flow patterning for cell-based assays. *Lab Chip***, 11,** 2060-2065.

Bertout, J. A., Patel, S. A. and Simon, M. C. (2008). HYPOXIA AND METABOLISM SERIES - TIMELINE The impact of O(2) availability on human cancer. *Nat Rev Cancer*, **8,** 967-975.

Bhatia, S. N., Yarmush, M. L. and Toner, M. (1997). Controlling cell interactions by micropatterning in co-cultures: hepatocytes and 3T3 fibroblasts. *J Biomed Mater Res*, **34,** 189-199.

Bhowmick, N. A., Chytil, A., Plieth, D., Gorska, A. E., Dumont, N., Shappell, S., Washington, M. K., Neilson, E. G. and Moses, H. L. (2004a). TGF-beta signaling in fibroblasts modulates the oncogenic potential of adjacent epithelia. *Science*, **303,** 848-851.

Bhowmick, N. A., Neilson, E. G. and Moses, H. L. (2004b). Stromal fibroblasts in cancer initiation and progression. *Nature*, **432,** 332-337.

Bhowmick, N. A. and Moses, H. L. (2005). Tumor-stroma interactions. *Curr Opin Genet Dev*, **15,** 97-101.

Bissell, M. J. and Radisky, D. (2001). Putting tumours in context. *Nat Rev Cancer*, **1,** 46-54.

Boyden, S. (1962). The chemotactic effect of mixtures of antibody and antigen on polymorphonuclear leucocytes. *J Exp Med*, **115,** 453-466.

Brantley-Sieders, D. M., Caughron, J., Hicks, D., Pozzi, A., Ruiz, J. C. and Chen, J. (2004). EphA2 receptor tyrosine kinase regulates endothelial cell migration and vascular assembly through phosphoinositide 3-kinase-mediated Rac1 GTPase activation. *J Cell Sci*, **117,** 2037-2049.

Brantley-Sieders, D. M., Dunaway, C. M., Rao, M., Short, S., Hwang, Y., Gao, Y. D., Li, D. Y., Jiang, A. X., Shyr, Y., Wu, J. Y. and Chen, J. (2011). Angiocrine Factors Modulate Tumor Proliferation and Motility through EphA2 Repression of Slit2 Tumor Suppressor Function in Endothelium. *Cancer Res*, **71,** 976-987.

Bristow, J. M., Sellers, M. H., Majumdar, D., Anderson, B., Hu, L. and Webb, D. J. (2009). The Rho-family GEF Asef2 activates Rac to modulate adhesion and actin dynamics and thereby regulate cell migration. *J Cell Sci*, **122,** 4535-4546.

Butler, J. M., Kobayashi, H. and Rafii, S. (2010). Instructive role of the vascular niche in promoting tumour growth and tissue repair by angiocrine factors. *Nat Rev Cancer*, **10,** 138-146.

Campenot, R. B. (1977). Local control of neurite development by nerve growth factor. *Proc Natl Acad Sci USA*, **74,** 4516-4519.

Carmeliet, P., Dor, Y., Herbert, J. M., Fukumura, D., Brusselmans, K., Dewerchin, M., Neeman, M., Bono, F., Abramovitch, R., Maxwell, P., Koch, C. J., Ratcliffe, P., Moons, L., Jain, R. K., Collen, D. and Keshert, E. (1998). Role of HIF-1alpha in hypoxia-mediated apoptosis, cell proliferation and tumour angiogenesis. *Nature*, **394,** 485-490.

Chang, Y. J., Mohseni, K. and Bright, V. M. (2007). Fabrication of tapered SU-8 structure and effect of sidewall angle for a variable focus microlens using EWOD. *Sensor Actuat a-Phys*, **136,** 546-553.

Cheng, N., Brantley, D. M. and Chen, J. (2002). The ephrins and Eph receptors in angiogenesis. *Cytokine Growth Factor Rev*, **13,** 75-85.

Cheng, S. Y., Heilman, S., Wasserman, M., Archer, S., Shuler, M. L. and Wu, M. (2007). A hydrogel-based microfluidic device for the studies of directed cell migration. *Lab Chip*, **7,** 763-769.

Chung, B. G., Flanagan, L. A., Rhee, S. W., Schwartz, P. H., Lee, A. P., Monuki, E. S. and Jeon, N. L. (2005). Human neural stem cell growth and differentiation in a gradient-generating microfluidic device. *Lab on a Chip*, **5,** 401-406.

Cochrane, D. E., Carraway, R. E., Boucher, W. and Feldberg, R. S. (1991). Rapid Degradation of Neurotensin by Stimulated Rat Mast-Cells. *Peptides*, **12,** 1187-1194.

Coleman, M. L. and Ratcliffe, P. J. (2009). Angiogenesis: escape from hypoxia. *Nat Med*, **15,** 491-493.

Craig, A. M., Graf, E. R. and Linhoff, M. W. (2006). How to build a central synapse: clues from cell culture. *Trends Neurosci*, **29,** 8-20.

Cukierman, E., Pankov, R., Stevens, D. R. and Yamada, K. M. (2001). Taking cell-matrix adhesions to the third dimension. *Science*, **294,** 1708-1712.

Debnath, J., Muthuswamy, S. K. and Brugge, J. S. (2003). Morphogenesis and oncogenesis of MCF-10A mammary epithelial acini grown in three-dimensional basement membrane cultures. *Methods*, **30,** 256-268.

Deen, W. M. (1998). *Analysis of transport phenomena*. Oxford University Press: New York.

Dertinger, S. K. W., Chiu, D. T., Jeon, N. L. and Whitesides, G. M. (2001). Generation of gradients having complex shapes using microfluidic networks. *Anal Chem*, **73,** 1240-1246.

Dertinger, S. K. W., Jiang, X. Y., Li, Z. Y., Murthy, V. N. and Whitesides, G. M. (2002). Gradients of substrate-bound laminin orient axonal specification of neurons. *Proc Natl Acad Sci USA*, **99,** 12542-12547.

Diao, J., Young, L., Kim, S., Fogarty, E. A., Heilman, S. M., Zhou, P., Shuler, M. L., Wu, M. and DeLisa, M. P. (2006). A three-channel microfluidic device for generating static linear gradients and its application to the quantitative analysis of bacterial chemotaxis. *Lab Chip*, **6,** 381-388.

Dillon, C. and Goda, Y. (2005). The actin cytoskeleton: integrating form and function at the synapse. *Annu Rev Neurosci*, **28,** 25-55.

Dittrich, P. S. and Manz, A. (2006). Lab-on-a-chip: microfluidics in drug discovery. *Nat Rev Drug Discov*, **5,** 210-218.

Duffy, D. C., McDonald, J. C., Schueller, O. and Whitesides, G. M. (1998). Rapid prototyping of microfluidic system in poly(dimethylsiloxane). *Anal Chem*, **70,** 4974-4984.

Dunaevsky, A., Tashiro, A., Majewska, A., Mason, C. and Yuste, R. (1999). Developmental regulation of spine motility in the mammalian central nervous system. *Proc Natl Acad Sci USA*, **96,** 13438-13443.

El-Ali, J., Sorger, P. K. and Jensen, K. F. (2006). Cells on chips. *Nature*, **442,** 403-411.

Etienne-Manneville, S. and Hall, A. (2003). Cdc42 regulates GSK-3 beta and adenomatous polyposis coli to control cell polarity. *Nature*, **421,** 753-756.

Even-Ram, S. and Yamada, K. M. (2005). Cell migration in 3D matrix. *Curr Opin Cell Biol*, **17,** 524-532.

Fiala, J. C., Spacek, J. and Harris, K. M. (2002). Dendritic spine pathology: cause or consequence of neurological disorders? *Brain Res Rev*, **39,** 29-54.

Folch, A. and Toner, M. (1998). Cellular micropatterns on biocompatible materials. *Biotechnol Progr*, **14,** 388-392.

Freshney, R. I. (2005). *Culture of animal cells : a manual of basic technique*, 5th edn. Wiley-Liss: Hoboken, N.J.

Friedl, P., Zanker, K. S. and Brocker, E. B. (1998). Cell migration strategies in 3-D extracellular matrix: Differences in morphology, cell matrix interactions, and integrin function. *Microsc Res Techniq*, **43,** 369-378.

Friedl, P. and Wolf, K. (2003). Tumour-cell invasion and migration: diversity and escape mechanisms. *Nat Rev Cancer*, **3,** 362-374.

Fuard, D., Tzvetkova-Chevolleau, T., Decossas, S., Tracqui, P. and Schiavone, P. (2008). Optimization of poly-di-methyl-siloxane (PDMS) substrates for studying cellular adhesion and motility. *Microelectron Eng*, **85,** 1289-1293.

Garner, C. C., Waites, C. L. and Ziv, N. E. (2006). Synapse development: still looking for the forest, still lost in the trees. *Cell Tissue Res*, **326,** 249-262.

Gerisch, G. and Keller, H. U. (1981). Chemotactic reorientation of granulocytes stimulated with micropipettes containing fMet-Leu-Phe. *J Cell Sci*, **52,** 1-10.

Giepmans, B. N., Adams, S. R., Ellisman, M. H. and Tsien, R. Y. (2006). The fluorescent toolbox for assessing protein location and function. *Science*, **312,** 217-224.

Girard, P. R. and Nerem, R. M. (1995). Shear-Stress Modulates Endothelial-Cell Morphology and F-Actin Organization through the Regulation of Focal Adhesion-Associated Proteins. *J Cell Physiol*, **163,** 179-193.

Golden, A. P. and Tien, J. (2007). Fabrication of microfluidic hydrogels using molded gelatin as a sacrificial element. *Lab Chip*, **7,** 720-725.

Goslin, K., Asmussen, H. and Banker, G. (1998). *Rat hippocampal neurons in low-density culture*. MIT Press: Cambridge, MA.

Gray, N. W., Weimer, R. M., Bureau, I. and Svoboda, K. (2006). Rapid redistribution of synaptic PSD-95 in the neocortex in vivo. *PLoS Biol*, **4,** e370.

Green, N. M. (1963). Avidin. 1. The Use of (14-C)Biotin for Kinetic Studies and for Assay. *Biochem J*, **89,** 585-591.

Gross, P. G., Kartalov, E. P., Scherer, A. and Weiner, L. P. (2007). Applications of microfluidics for neuronal studies. *J Neurol Sci*, **252,** 135-143.

Haessler, U., Kalinin, Y., Swartz, M. A. and Wu, M. (2009). An agarose-based microfluidic platform with a gradient buffer for 3D chemotaxis studies. *Biomed Microdevices*, **11,** 827-835.

Hama, H., Hara, C., Yamaguchi, K. and Miyawaki, A. (2004). PKC signaling mediates global enhancement of excitatory synaptogenesis in neurons triggered by local contact with astrocytes. *Neuron*, **41,** 405-415.

Harris, A. L. (2002). Hypoxia - A key regulatory factor in tumour growth. *Nat Rev Cancer*, **2,** 38-47.

Haydon, P. G. (2001). Glia: Listening and talking to the synapse. *Nat Rev Neurosci*, **2,** 185-193.

Holash, J., Davis, S., Papadopoulos, N., Croll, S. D., Ho, L., Russell, M., Boland, P., Leidich, R., Hylton, D., Burova, E., Ioffe, E., Huang, T., Radziejewski, C., Bailey, K., Fandl, J. P., Daly, T., Wiegand, S. J., Yancopoulos, G. D. and Rudge, J. S. (2002). VEGF-Trap: A VEGF blocker with potent antitumor effects. *Proc Natl Acad Sci USA*, **99,** 11393-11398.

Houston, K. S., Weinkauf, D. H. and Stewart, F. F. (2002). Gas transport characteristics of plasma treated poly(dimethylsiloxane) and polyphosphazene membrane materials. *J Membrane Sci*, **205,** 103-112.

Hui, E. E. and Bhatia, S. N. (2007). Micromechanical control of cell-cell interactions. *Proc Natl Acad Sci USA*, **104,** 5722-5726.

Ikeda, E., Achen, M. G., Breier, G. and Risau, W. (1995). Hypoxia-induced transcriptional activation and increased mRNA stability of vascular endothelial growth factor in C6 glioma cells. *J Biol Chem*, **270,** 19761-19766.

Irimia, D. and Toner, M. (2006). Cell handling using microstructured membranes. *Lab Chip*, **6,** 345-352.

Irimia, D., Charras, G., Agrawal, N., Mitchison, T. and Toner, M. (2007). Polar stimulation and constrained cell migration in microfluidic channels. *Lab on a Chip*, **7,** 1783-1790.

Jacks, T. and Weinberg, R. A. (2002). Taking the study of cancer cell survival to a new dimension. *Cell*, **111,** 923-925.

Jeon, N. L., Dertinger, S. K. W., Chiu, D. T., Choi, I. S., Stroock, A. D. and Whitesides, G. M. (2000). Generation of solution and surface gradients using microfluidic systems. *Langmuir*, **16,** 8311-8316.

Jeon, N. L., Baskaran, H., Dertinger, S. K. W., Whitesides, G. M., Van de Water, L. and Toner, M. (2002). Neutrophil chemotaxis in linear and complex gradients of interleukin-8 formed in a microfabricated device. *Nat Biotechnol*, **20,** 826-830.

Kaelin, W. G., Jr. (2008). The von Hippel-Lindau tumour suppressor protein: O2 sensing and cancer. *Nat Rev Cancer*, **8,** 865-873.

Kalluri, R. and Zeisberg, M. (2006). Fibroblasts in cancer. *Nat Rev Cancer*, **6,** 392-401.

Kane, B. J., Zinner, M. J., Yarmush, M. L. and Toner, M. (2006). Liver-specific functional studies in a microfluidic array of primary mammalian hepatocytes. *Anal Chem*, **78,** 4291-4298.

Kawasaki, Y., Sagara, M., Shibata, Y., Shirouzu, M., Yokoyama, S. and Akiyama, T. (2007). Identification and characterization of Asef2, a guanine-nucleotide exchange factor specific for Rac1 and Cdc42. *Oncogene*, **26,** 7620-7627.

Khademhosseini, A., Yeh, J., Eng, G., Karp, J., Kaji, H., Borenstein, J., Farokhzad, O. C. and Langer, R. (2005). Cell docking inside microwells within reversibly

sealed microfluidic channels for fabricating multiphenotype cell arrays. *Lab Chip*, **5,** 1380-1386.

Khetani, S. R. and Bhatia, S. N. (2008). Microscale culture of human liver cells for drug development. *Nat Biotechnol*, **26,** 120-126.

Kohidai, L. (1995). Method for Determination of Chemoattraction in Tetrahymena-Pyriformis. *Curr Microbiol*, **30,** 251-253.

Kosto, K. B. and Deen, W. M. (2005). Hindered convection of macromolecules in hydrogels. *Biophys J*, **88,** 277-286.

Kuperwasser, C., Chavarria, T., Wu, M., Magrane, G., Gray, J. W., Carey, L., Richardson, A. and Weinberg, R. A. (2004). Reconstruction of functionally normal and malignant human breast tissues in mice. *Proc Natl Acad Sci USA*, **101,** 4966-4971.

Lauffenburger, D. A. and Horwitz, A. F. (1996). Cell migration: A physically integrated molecular process. *Cell*, **84,** 359-369.

Lee, J. N., Park, C. and Whitesides, G. M. (2003). Solvent compatibility of poly(dimethylsiloxane)-based microfluidic devices. *Anal Chem*, **75,** 6544-6554.

Lee, K., Kim, C., Kim, Y., Ahn, B., Bang, J., Kim, J., Panchapakesan, R., Yoon, Y. K., Kang, J. Y. and Oh, K. W. (2011). Microfluidic concentration-on-demand combinatorial dilutions. *Microfluid Nanofluid*, **11,** 75-86.

Levy, W. B. and Steward, O. (1979). Synapses as associative memory elements in the hippocampal formation. *Brain Res*, **175,** 233-245.

Li, C. Y., Shan, S., Huang, Q., Braun, R. D., Lanzen, J., Hu, K., Lin, P. and Dewhirst, M. W. (2000). Initial stages of tumor cell-induced angiogenesis: evaluation via skin window chambers in rodent models. *J Natl Cancer Inst*, **92,** 143-147.

Li, Z. and Sheng, M. (2003). Some assembly required: the development of neuronal synapses. *Nat Rev Mol Cell Bio*, **4,** 833-841.

Lin, F., Saadi, W., Rhee, S. W., Wang, S. J., Mittal, S. and Jeon, N. L. (2004). Generation of dynamic temporal and spatial concentration gradients using microfluidic devices. *Lab on a Chip*, **4,** 164-167.

Liotta, L. A. and Kohn, E. C. (2001). The microenvironment of the tumour-host interface. *Nature*, **411,** 375-379.

Liu, X. H., Kirschenbaum, A., Yao, S., Stearns, M. E., Holland, J. F., Claffey, K. and Levine, A. C. (1999). Upregulation of vascular endothelial growth factor by cobalt chloride-simulated hypoxia is mediated by persistent induction of cyclooxygenase-2 in a metastatic human prostate cancer cell line. *Clin Exp Metastasis*, **17,** 687-694.

Longsworth, L. G. (1953). Diffusion Measurements, at 25°, of Aqueous Solutions of Amino Acids, Peptides and Sugars. *J Am Chem Soc*, **75,** 5.

Lotters, J. C., Olthuis, W., Veltink, P. H. and Bergveld, P. (1997). The mechanical properties of the rubber elastic polymer polydimethylsiloxane for sensor applications. *J Micromech Microeng*, **7,** 145-147.

Luo, D. and Saltzman, W. M. (2000). Synthetic DNA delivery systems. *Nat Biotechnol*, **18,** 33-37.

Lynn, N. S. and Dandy, D. S. (2009). Passive microfluidic pumping using coupled capillary/evaporation effects. *Lab Chip*, **9,** 3422-3429.

Lynn, N. S., Henry, C. S. and Dandy, D. S. (2009). Evaporation from microreservoirs. *Lab Chip*, **9,** 1780-1788.

Mandriota, S. J. and Pepper, M. S. (1998). Regulation of angiopoietin-2 mRNA levels in bovine microvascular endothelial cells by cytokines and hypoxia. *Circ Res*, **83,** 852-859.

Mauch, D. H., Nagler, K., Schumacher, S., Goritz, C., Muller, E. C., Otto, A. and Pfrieger, F. W. (2001). CNS synaptogenesis promoted by glia-derived cholesterol. *Science*, **294,** 1354-1357.

McAllister, A. K. (2007). Dynamic aspects of CNS synapse formation. *Annu Rev Neurosci*, **30,** 425-450.

McCarty, W. J. and Johnson, M. (2007). The hydraulic conductivity of Matrigel (TM). *Biorheology*, **44,** 303-317.

McDonald, J. C. and Whitesides, G. M. (2002). Poly(dimethylsiloxane) as a material for fabricating microfluidic devices. *Accounts Chem Res*, **35,** 491-499.

Mcneil, P. L. (1989). Incorporation of Macromolecules into Living Cells. *Method Cell Biol*, **29,** 153-173.

Merker, T. C., Bondar, V. I., Nagai, K., Freeman, B. D. and Pinnau, I. (2000). Gas sorption, diffusion, and permeation in poly(dimethylsiloxane). *J Polym Sci Pol Phys*, **38,** 415-434.

Meyvantsson, I. and Beebe, D. J. (2008). Cell culture models in microfluidic systems. *Annu Rev Anal Chem*, **1,** 423-449.

Micke, P. and Ostman, A. (2004). Tumour-stroma interaction: cancer-associated fibroblasts as novel targets in anti-cancer therapy? *Lung Cancer*, **45 Suppl 2,** S163-175.

Millet, L. J., Stewart, M. E., Sweedler, J. V., Nuzzo, R. G. and Gillette, M. U. (2007). Microfluidic devices for culturing primary mammalian neurons at low densities. *Lab Chip*, **7,** 987-994.

Mueller, M. M. and Fusenig, N. E. (2004). Friends or foes - Bipolar effects of the tumour stroma in cancer. *Nat Rev Cancer*, **4,** 839-849.

Narayanan, J., Xiong, J.-Y. and Liu, X.-Y. (2006). Determination of agarose gel pore size: Absorbance measurements vis a vis other techniques *J Phys Conf Ser*, **28,** 4.

Nelson, R. D., Quie, P. G. and Simmons, R. L. (1975). Chemotaxis under agarose: a new and simple method for measuring chemotaxis and spontaneous migration of human polymorphonuclear leukocytes and monocytes. *J Immunol*, **115,** 1650-1656.

Oh, K. W. and Ahn, C. H. (2006). A review of microvalves. *J Micromech Microeng*, **16,** R13-R39.

Ozawa, C. R., Banfi, A., Glazer, N. L., Thurston, G., Springer, M. L., Kraft, P. E., McDonald, D. M. and Blau, H. M. (2004). Microenvironmental VEGF concentration, not total dose, determines a threshold between normal and aberrant angiogenesis. *J Clin Invest*, **113,** 516-527.

Paguirigan, A. L. and Beebe, D. J. (2008). Microfluidics meet cell biology: bridging the gap by validation and application of microscale techniques for cell biological assays. *Bioessays*, **30,** 811-821.

Petersen, N. O., Brown, C., Kaminski, A., Rocheleau, J., Srivastava, M. and Wiseman, P. W. (1998). Analysis of membrane protein cluster densities and sizes in situ by image correlation spectroscopy. *Faraday Discuss*, **111,** 289-305.

Pfrieger, F. W. (2002). Role of glia in synapse development. *Curr Opin Neurobiol*, **12,** 486-490.

Pfrieger, F. W. (2009). Roles of glial cells in synapse development. *Cell Mol Life Sci*, **66,** 2037-2047.

Pugh, C. W. and Ratcliffe, P. J. (2003). Regulation of angiogenesis by hypoxia: role of the HIF system. *Nat Med*, **9,** 677-684.

Raftopoulou, M. and Hall, A. (2004). Cell migration: Rho GTPases lead the way. *Dev Biol*, **265,** 23-32.

Ramanujan, S., Pluen, A., McKee, T. D., Brown, E. B., Boucher, Y. and Jain, R. K. (2002). Diffusion and convection in collagen gels: Implications for transport in the tumor interstitium. *Biophys J*, **83,** 1650-1660.

Ravula, S. K., Wang, M. S., Asress, S. A., Glass, J. D. and Bruno Frazier, A. (2007). A compartmented neuronal culture system in microdevice format. *J Neurosci Meth*, **159,** 78-85.

Regehr, K. J., Domenech, M., Koepsel, J. T., Carver, K. C., Ellison-Zelski, S. J., Murphy, W. L., Schuler, L. A., Alarid, E. T. and Beebe, D. J. (2009). Biological implications of polydimethylsiloxane-based microfluidic cell culture. *Lab Chip*, **9,** 2132-2139.

Rottner, K., Hall, A. and Small, J. V. (1999). Interplay between Rac and Rho in the control of substrate contact dynamics. *Curr Biol*, **9,** 640-648.

Saadi, W., Rhee, S. W., Lin, F., Vahidi, B., Chung, B. G. and Jeon, N. L. (2007). Generation of stable concentration gradients in 2D and 3D environments using a microfluidic ladder chamber. *Biomed Microdevices*, **9,** 627-635.

Sabeh, F., Ota, I., Holmbeck, K., Birkedal-Hansen, H., Soloway, P., Balbin, M., Lopez-Otin, C., Shapiro, S., Inada, M., Krane, S., Allen, E., Chung, D. and Weiss, S. J. (2004). Tumor cell traffic through the extracellular matrix is controlled by the membrane-anchored collagenase MT1-MMP. *J Cell Biol*, **167,** 769-781.

Sagara, M., Kawasaki, Y., Iemura, S., Natsume, T., Takai, Y. and Akiyama, T. (2009). Asef2 and Neurabin2 cooperatively regulate actin cytoskeletal organization and are involved in HGF-induced cell migration. *Oncogene*, **28,** 1357-1365.

Samoszuk, M., Tan, J. and Chorn, G. (2005). Clonogenic growth of human breast cancer cells co-cultured in direct contact with serum-activated fibroblasts. *Breast Cancer Res*, **7,** R274-283.

Sasoglu, F. M., Bohl, A. J. and Layton, B. E. (2007). Design and microfabrication of a high-aspect-ratio PDMS microbeam array for parallel nanonewton force measurement and protein printing. *J Micromech Microeng*, **17,** 623-632.

Scholl, M., Sprossler, C., Denyer, M., Krause, M., Nakajima, K., Maelicke, A., Knoll, W. and Offenhausser, A. (2000). Ordered networks of rat hippocampal neurons attached to silicon oxide surfaces. *J Neurosci Meth*, **104,** 65-75.

Schwartz, M. A. and Shattil, S. J. (2000). Signaling networks linking integrins and Rho family GTPases. *Trends Biochem Sci*, **25,** 388-391.

Selkoe, D. J. (2002). Alzheimer's disease is a synaptic failure. *Science*, **298,** 789-791.

Shamloo, A., Ma, N., Poo, M. M., Sohn, L. L. and Heilshorn, S. C. (2008). Endothelial cell polarization and chemotaxis in a microfluidic device. *Lab Chip*, **8,** 1292-1299.

Shin, H. S., Kim, H. J., Sim, S. J. and Jeon, N. L. (2009). Shear Stress Effect on Transfection of Neurons Cultured in Microfluidic Devices. *J Nanosci Nanotechno*, **9,** 7330-7335.

Skelley, A. M., Kirak, O., Suh, H., Jaenisch, R. and Voldman, J. (2009). Microfluidic control of cell pairing and fusion. *Nat Methods*, **6,** 147-152.

Skinner, M. K. (1991). Cell-cell interactions in the testis. *Endocr Rev*, **12,** 45-77.

Squires, T. M. and Quake, S. R. (2005). Microfluidics: Fluid physics at the nanoliter scale. *Rev Mod Phys*, **77,** 977-1026.

Stroh, M., Zipfel, W. R., Williams, R. M., Webb, W. W. and Saltzman, W. M. (2003). Diffusion of nerve growth factor in rat striatum as determined by multiphoton microscopy. *Biophys J*, **85,** 581-588.

Studer, V., Hang, G., Pandolfi, A., Ortiz, M., Anderson, W. F. and Quake, S. R. (2004a). Scaling properties of a low-actuation pressure microfluidic valve. *J Appl Phys*, **95,** 393-398.

Studer, V., Jameson, R., Pellereau, E., Pepin, A. and Chen, Y. (2004b). A microfluidic mammalian cell sorter based on fluorescence detection. *Microelectron Eng*, **73-74,** 852-857.

Takayama, S., McDonald, J. C., Ostuni, E., Liang, M. N., Kenis, P. J. A., Ismagilov, R. F. and Whitesides, G. M. (1999). Patterning cells and their environments using multiple laminar fluid flows in capillary networks. *Proc Natl Acad Sci USA*, **96,** 5545-5548.

Takayama, S., Ostuni, E., LeDuc, P., Naruse, K., Ingber, D. E. and Whitesides, G. M. (2001). Subcellular positioning of small molecules. *Nature*, **411,** 1016.

Tang, M. D., Golden, A. P. and Tien, J. (2003). Molding of three-dimensional microstructures of gels. *J Am Chem Soc*, **125,** 12988-12989.

Taylor, A. M., Blurton-Jones, M., Rhee, S. W., Cribbs, D. H., Cotman, C. W. and Jeon, N. L. (2005). A microfluidic culture platform for CNS axonal injury, regeneration and transport. *Nat Methods*, **2,** 599-605.

Taylor, A. M., Dieterich, D. C., Ito, H. T., Kim, S. A. and Schuman, E. M. (2010). Microfluidic local perfusion chambers for the visualization and manipulation of synapses. *Neuron*, **66,** 57-68.

Thangawng, A. L., Ruoff, R. S., Swartz, M. A. and Glucksberg, M. R. (2007). An ultra-thin PDMS membrane as a bio/micro-nano interface: fabrication and characterization. *Biomed Microdevices*, **9,** 587-595.

Thorsen, T., Maerkl, S. J. and Quake, S. R. (2002). Microfluidic large-scale integration. *Science*, **298,** 580-584.

Tlsty, T. D. (2001). Stromal cells can contribute oncogenic signals. *Semin Cancer Biol*, **11,** 97-104.

Unger, M. A., Chou, H. P., Thorsen, T., Scherer, A. and Quake, S. R. (2000). Monolithic microfabricated valves and pumps by multilayer soft lithography. *Science*, **288,** 113-116.

Vogt, A. K., Wrobel, G., Meyer, W., Knoll, W. and Offenhausser, A. (2005). Synaptic plasticity in micropatterned neuronal networks. *Biomaterials*, **26,** 2549-2557.

Volterra, A. and Meldolesi, J. (2005). Astrocytes, from brain glue to communication elements: The revolution continues. *Nat Rev Neurosci*, **6,** 626-640.

Waites, C. L., Craig, A. M. and Garner, C. C. (2005). Mechanisms of vertebrate synaptogenesis. *Annu Rev Neurosci*, **28,** 251-274.

Walker, G. M. and Beebe, D. J. (2002). A passive pumping method for microfluidic devices. *Lab Chip*, **2,** 131-134.

Walker, G. M., Zeringue, H. C. and Beebe, D. J. (2004). Microenvironment design considerations for cellular scale studies. *Lab Chip*, **4,** 91-97.

Walker, G. M., Sai, J., Richmond, A., Stremler, M., Chung, C. Y. and Wikswo, J. P. (2005). Effects of flow and diffusion on chemotaxis studies in a microfabricated gradient generator. *Lab on a Chip*, **5,** 611-618.

Webb, D. J. and Horwitz, A. F. (2003). New dimensions in cell migration. *Nat Cell Biol*, **5,** 690-692.

Weiner, O. D. (2002). Regulation of cell polarity during eukaryotic chemotaxis: the chemotactic compass. *Curr Opin Cell Biol*, **14,** 196-202.

White, F. M. (2006). *Viscous fluid flow*, 3rd edn. McGraw-Hill Higher Education: New York, NY.

Whitesides, G. M., Ostuni, E., Takayama, S., Jiang, X. and Ingber, D. E. (2001). Soft lithography in biology and biochemistry. *Annu Rev Biomed Eng***, 3,** 335-373.

Wilson, S. R., Tracy, C. J. and Freeman, J. L. (1993). *Handbook of multilevel metallization for integrated circuits : materials, technology, and applications*. Noyes: Park Ridge, N.J., U.S.A.

Wiseman, P. W., Brown, C. M., Webb, D. J., Hebert, B., Johnson, N. L., Squier, J. A., Ellisman, M. H. and Horwitz, A. F. (2004). Spatial mapping of integrin interactions and dynamics during cell migration by Image Correlation Microscopy. *J Cell Sci***, 117,** 5521-5534.

Wolfer, D. P., Crusio, W. E. and Lipp, H. P. (2002). Knockout mice: simple solutions to the problems of genetic background and flanking genes. *Trends Neurosci***, 25,** 336-340.

Xia, Y. N. and Whitesides, G. M. (1998). Soft lithography. *Annu Rev Mater Sci***, 28,** 153-184.

Yeon, J. H. and Park, J. K. (2007). Microfluidic cell culture systems for cellular analysis. *Biochip J***, 1,** 17-27.

Yuan, Y., Hilliard, G., Ferguson, T. and Millhorn, D. E. (2003). Cobalt inhibits the interaction between hypoxia-inducible factor-alpha and von Hippel-Lindau protein by direct binding to hypoxia-inducible factor-alpha. *J Biol Chem***, 278,** 15911-15916.

Zhang, H., Webb, D. J., Asmussen, H. and Horwitz, A. F. (2003). Synapse formation is regulated by the signaling adaptor GIT1. *J Cell Biol***, 161,** 131-142.

Zicha, D., Dunn, G. A. and Brown, A. F. (1991). A new direct-viewing chemotaxis chamber. *J Cell Sci***, 99 (Pt 4),** 769-775.

Zicha, D., Dunn, G. and Jones, G. (1997). Analyzing chemotaxis using the Dunn direct-viewing chamber. *Methods Mol Biol***, 75,** 449-457.